

# Reconstruction of temperature, accumulation rate, and layer thinning from an ice core at South Pole using a statistical inverse method

Emma C. Kahle<sup>1,1</sup>, Eric J. Steig<sup>1,1</sup>, Tyler R. Jones<sup>2,2</sup>, T.J. Fudge<sup>1,1</sup>, Michelle Rebecca Koutnik<sup>1,1</sup>, Valerie Morris<sup>2,2</sup>, Bruce Vaughn<sup>2,2</sup>, Andrew Schauer<sup>1,1</sup>, C. Max Stevens<sup>3,3</sup>, Howard Conway<sup>1,1</sup>, Edwin D Waddington<sup>1,1</sup>, Christo Buizert<sup>4,4</sup>, Jenna Epifanio<sup>4,4</sup>, and James W.C. White<sup>2,2</sup>

<sup>1</sup>University of Washington

<sup>2</sup>University of Colorado Boulder

<sup>3</sup>University of Washington

<sup>4</sup>Oregon State University

November 30, 2022

## Abstract

Data from the South Pole ice core (SPC14) are used to constrain climate conditions and ice-flow-induced layer thinning for the last 54,000 years. Empirical constraints are obtained from the SPC14 ice and gas timescales, used to calculate annual-layer thickness and the gas-ice age difference ( $\Delta\text{age}$ ), and from high-resolution measurements of water isotopes, used to calculate the water-isotope diffusion length. Both  $\Delta\text{age}$  and diffusion length depend on firn properties and therefore contain information about past temperature and snow-accumulation rate. A statistical inverse approach is used to obtain an ensemble of reconstructions of temperature, accumulation-rate, and thinning of annual layers in the ice sheet at the SPC14 site. The traditional water-isotope/temperature relationship is not used as a constraint; the results therefore provide an independent calibration of that relationship. The temperature reconstruction yields a glacial-interglacial temperature change of  $6.7 \pm 1.0$  °C at the South Pole. The sensitivity of  $\delta^{18}\text{O}$  to temperature is  $0.99 \pm 0.03$  significantly greater than the spatial slope of  $\sim 0.8$  East Antarctic ice core records. The reconstructions of accumulation rate and ice thinning show millennial-scale variations in the thinning function as well as decreased thinning at depth compared to the results of a 1-D ice flow model, suggesting influence of bedrock topography on ice flow.

1 **Reconstruction of temperature, accumulation rate, and**  
2 **layer thinning from an ice core at South Pole, using a**  
3 **statistical inverse method**

4 **Emma C. Kahle<sup>1</sup>, Eric J. Steig<sup>1</sup>, Tyler R. Jones<sup>2</sup>, T.J. Fudge<sup>1</sup>, Michelle R.**  
5 **Koutnik<sup>1</sup>, Valerie Morris<sup>2</sup>, Bruce H. Vaughn<sup>2</sup>, Andrew J. Schauer<sup>1</sup>, C. Max**  
6 **Stevens<sup>1</sup>, Howard Conway<sup>1</sup>, Edwin D. Waddington<sup>1</sup>, Christo Buizert<sup>3</sup>, Jenna**  
7 **Epifanio<sup>3</sup>, James W. C. White<sup>2</sup>**

8 <sup>1</sup>Department of Earth and Space Sciences, University of Washington, Seattle WA 98195, USA

9 <sup>2</sup>Institute of Arctic and Alpine Research, University of Colorado, Boulder CO 80309, USA

10 <sup>3</sup>College of Earth Ocean and Atmospheric Sciences, Oregon State University, Corvallis OR 97331, USA

11 **Key Points:**

- 12 • Observations of water-isotope ratios, the gas-ice age difference, and annual-layer  
13 thickness are obtained from an ice core at South Pole.
- 14 • An inverse method using a firn model with isotope diffusion provides self-consistent  
15 temperature, accumulation rate, and thinning histories.
- 16 • Novel calibration of the isotope paleothermometer shows that glacial-interglacial  
17 temperature change at the South Pole was 6.3 +/- 0.8 K.

**Abstract**

Data from the South Pole ice core (SPC14) are used to constrain climate conditions and ice-flow-induced layer thinning for the last 54,000 years. Empirical constraints are obtained from the SPC14 ice and gas timescales, used to calculate annual-layer thickness and the gas-ice age difference ( $\Delta\text{age}$ ), and from high-resolution measurements of water isotopes, used to calculate the water-isotope diffusion length. Both  $\Delta\text{age}$  and diffusion length depend on firn properties and therefore contain information about past temperature and snow-accumulation rate. A statistical inverse approach is used to obtain an ensemble of reconstructions of temperature, accumulation-rate, and thinning of annual layers in the ice sheet at the SPC14 site. The traditional water-isotope/temperature relationship is not used as a constraint; the results therefore provide an independent calibration of that relationship. The sensitivity of water isotopes to temperature is greater than previously assumed for East Antarctica. The temperature reconstruction yields a glacial-interglacial temperature change of  $6.3\pm 0.8^\circ\text{C}$  at the South Pole.

**1 Introduction**

Ice cores from polar ice sheets provide important records of past changes in climate and ice dynamics. Temperature and snow-accumulation rate are critical targets for reconstruction from ice-core data (Lorius et al., 1990). The traditional approach to reconstructing temperature is the use of water isotope ratios ( $\delta^{18}\text{O}$ ,  $\delta\text{D}$ ), calibrated using empirical relationships (Dansgaard, 1964; Jouzel et al., 1993). Another approach is borehole thermometry, which provides a direct measurement of the modern temperature profile of the ice sheet that can be related to surface temperature history through a heat advection-diffusion model (Cuffey et al., 1995; Dahl-Jensen et al., 1998). Finally, measurements of  $\delta^{15}\text{N}$  of  $\text{N}_2$  in trapped air bubbles provide information about the thickness of the firn layer and past abrupt temperature changes that produce thermal gradients (Sowers et al., 1992; Schwander, 1989; Severinghaus et al., 1998). Because firn thickness is a function of accumulation rate and temperature,  $\delta^{15}\text{N}$  can be used to provide constraints on both variables through modeling of the firn densification process (Huber et al., 2006; Guillevic et al., 2013; Kindler et al., 2014). With independent constraints on the ice-core depth-age relationship, in particular from annual-layer counting, these approaches can be combined to produce robust estimates of temperature and accumulation rate through time. Results from Greenland (Buizert et al., 2014) and the West Antarctic Ice Sheet (WAIS) Divide ice core (Cuffey et al., 2016) provide recent examples.

In comparison with locations in West Antarctica and Greenland, ice-core sites in East Antarctica pose special challenges. The low accumulation rates typical of the East Antarctic plateau are unfavorable for borehole thermometry, which generally requires high accumulation rates and locations near ice divides, where the horizontal velocity is low. Additionally, some recent studies have questioned the validity of firn models at the typically very cold temperatures in East Antarctica (Freitag et al., 2013; Bréant et al., 2017). One approach that may help to address such challenges is to use the “diffusion length”, a measure of the spectral properties of high-resolution measurements of water-isotope ratios. Water-isotope diffusion length reflects the vertical diffusion experienced by water molecules through the firn column (Johnsen, 1977; Whillans and Grootes, 1985; Cuffey and Steig, 1998; Johnsen et al., 2000). While diffusion length has primarily been used as a proxy for temperature (e.g., Simonsen et al., 2011; van der Wel et al., 2015; Gkinis et al., 2014; Holme et al., 2018), it is sensitive to both temperature and accumulation rate though their influence on the firn density profile, and is also affected by vertical strain (Gkinis et al., 2014; Jones et al., 2017a). Diffusion length thus provides an independent constraint on several important ice-core properties: temperature, accumulation rate, and the thinning history due to ice deformation.

68 Here, we present data from a new ice core (SPC14) from the South Pole, East Antarc-  
 69 tica, and we use a novel approach to combine multiple data sets to constrain temper-  
 70 ature, accumulation-rate, and ice-thinning histories. We take advantage of two timescales  
 71 for SPC14, one for the ice (Winski et al., 2019) and one for the gas enclosed within it  
 72 (Epifanio et al., 2020), to obtain an empirical measure of the gas-age ice-age difference  
 73 ( $\Delta$ age). We also use high-resolution measurements of  $\delta^{17}\text{O}$ ,  $\delta^{18}\text{O}$ , and  $\delta\text{D}$  of ice to ob-  
 74 tain water-isotope diffusion lengths.

75 We use a statistical inverse approach to obtain optimized, self-consistent reconstructions  
 76 of temperature and accumulation rate using a combined firn-densification and water-isotope  
 77 diffusion model. We exclude gas isotope ( $\delta^{15}\text{N}$ ) data and use the water-isotope values  
 78 only for calculating diffusion length, reserving these variables for comparison and val-  
 79 idation. This approach allows us to produce a novel and independent calibration of the  
 80 traditional isotope paleothermometer without the use of borehole thermometry. We also  
 81 obtain an independent constraint on the thinning of annual layers. This is important at  
 82 South Pole because the location of the site is about 200 km from the ice divide and the  
 83 ice-flow history is not well known at ages earlier than the Holocene (Lilien et al., 2018).

## 84 2 Data from the South Pole Ice Core

85 The South Pole Ice Core (SPC14) was obtained from 2014 to 2016 at 89.9889°S, 98.1596°W,  
 86 approximately 2 km from the geographic South Pole. SPC14 was drilled to a depth of  
 87 1751 m, equivalent to an age of approximately 54 ka (Winski et al., 2019). Compared  
 88 to other East Antarctic ice-core sites, South Pole has a relatively high annual accumu-  
 89 lation rate (8 cm w.e.  $\text{yr}^{-1}$ ) (Casey et al., 2014) given its low mean-annual air temper-  
 90 ature of  $-49^\circ\text{C}$  (Lazzara et al., 2012). The mean firn temperature is  $-51^\circ\text{C}$  (Severinghaus  
 91 et al., 2001). The modern surface ice velocity is  $10 \text{ m yr}^{-1}$  (Casey et al., 2014).

92 The data sets used in our analysis are developed from the independent ice and gas timescales  
 93 for SPC14 described previously by Winski et al. (2019) and Epifanio et al. (2020), and  
 94 water-isotope measurements presented here for the first time. We briefly summarize the  
 95 information obtained directly from the ice-core measurements as well as the data sets  
 96 derived from that information (annual-layer thickness,  $\Delta$ age, and water-isotope diffu-  
 97 sion length).

### 98 2.1 Ice Timescale and Annual-Layer Thickness

99 The ice timescale was constructed by stratigraphic matching of 251 volcanic tie points  
 100 between SPC14 and WAIS Divide (Winski et al., 2019). Between tie points, identifica-  
 101 tion of individual layers from seasonal cycles in sodium and magnesium ions was used  
 102 to produce an annually-resolved timescale for most of the Holocene. For ages greater than  
 103 11.3 ka, despite lack of annual resolution, the uncertainty of the timescale is estimated  
 104 to be within 124 years relative to WD2014 (Winski et al., 2019). Annual-layer thickness  
 105 is given by the depth between successive years on the SP19 timescale. For ages older than  
 106 11.3 ka where annual layers could not be identified, Winski et al. (2019) found the smoothest  
 107 annual-layer thickness which matched 95% of the volcanic tie points to within one year.  
 108 Based on the uncertainty associated with interpolation between sparse tie points (Fudge  
 109 et al., 2014), we estimate the uncertainty in annual-layer thickness (two standard devi-  
 110 ations, hereafter s.d.) to be  $\pm 3\%$  of the value in the Holocene, increasing to  $\pm 10\%$  of the  
 111 value at earlier ages.

## 2.2 Gas Timescale and $\Delta\text{age}$

Epifanio et al. (2020) developed the SPC14 gas timescale through stratigraphic matching of features in the high-resolution  $\text{CH}_4$  records of the SPC14 and WAIS Divide cores. The difference in age between the ice and gas timescales,  $\Delta\text{age}$ , is a measure of the ice age at the lock-in depth, which depends on the rate of firn densification (Schwander et al., 1984,9; Blunier and Schwander, 2000). Epifanio et al. (2020) determined  $\Delta\text{age}$  empirically at each of the  $\text{CH}_4$  tie points and used a cubic spline fit to derive a continuous  $\Delta\text{age}$  curve for all depths. Due to the empirical nature of the gas timescale, the SPC14  $\Delta\text{age}$  record is determined without the use of a firn-densification model. Moreover, the SPC14  $\Delta\text{age}$  was obtained without relying on the additional constraint of  $\delta^{15}\text{N}$  to determine lock-in depth.

We assign an age to each empirical  $\Delta\text{age}$  estimate as the mid-point between the gas-age and ice-age timescales from which  $\Delta\text{age}$  is calculated. This approximation is justified by results from a dynamic densification model (Stevens et al., 2020), which show that at a site like South Pole the timescale on which  $\Delta\text{age}$  responds to climate variations is a time interval shorter than  $\Delta\text{age}$  itself. Uncertainty in  $\Delta\text{age}$  depends on uncertainty in the match between the WAIS Divide and SPC14 gas timescales, the uncertainty associated with interpolation between tie points, and uncertainty in the  $\Delta\text{age}$  for WAIS Divide. Because  $\Delta\text{age}$  is an order of magnitude smaller at WAIS Divide than at South Pole, that source of uncertainty is the smallest. The uncertainty estimated by Epifanio et al. (2020) ranges from  $\pm 1\%$  to  $\pm 8\%$  (two s.d.) of the value of  $\Delta\text{age}$ .

## 2.3 Water-Isotope Measurements and Diffusion Length

We measured water-isotope ratios at an effective resolution of 0.5 cm using continuous flow analysis (CFA), following the methods described in Jones et al. (2017b). We measured  $\delta^{18}\text{O}$  and  $\delta\text{D}$  for the entirety of the core and  $\delta^{17}\text{O}$  from a depth of 556 m through the bottom of the core. We used Picarro Inc. cavity ring-down laser spectroscopy (CRDS) instruments, including both a model L2130-i (for  $\delta^{18}\text{O}$  and  $\delta\text{D}$ ) and a model L2140-i for  $\delta^{17}\text{O}$  (Steig et al., 2014). We use the standard notation for  $\delta^{18}\text{O}$ :

$$\delta^{18}\text{O}_{\text{sample}} = \left( \frac{^{18}\text{O}}{^{16}\text{O}} \right)_{\text{sample}} / \left( \frac{^{18}\text{O}}{^{16}\text{O}} \right)_{\text{VSMOW}} - 1,$$

where VSMOW is Vienna Standard Mean Ocean Water.  $\delta^{17}\text{O}$  and  $\delta\text{D}$  are defined similarly. These measurements were used to calculate the water-isotope diffusion length. Figure 1 shows the  $\delta^{18}\text{O}$  measurements at 100-year-mean resolution as a function of age.

After deposition as snow on the ice-sheet surface, water isotopologues diffuse through interconnected air pathways among ice grains in the firn, driven by isotope-concentration gradients in the vapor phase (Johnsen, 1977; Whillans and Grootes, 1985; Cuffey and Steig, 1998). In solid ice below the firn column, diffusion continues, but at a rate orders of magnitude slower than in the firn (Johnsen et al., 2000). The extent of diffusion is quantified as the diffusion length, the mean cumulative diffusive-displacement in the vertical direction of water molecules relative to their original location in the firn.

Diffusion length is determined from spectral analysis of the high-resolution water-isotope data, following the methods described in Kahle et al. (2018). We use discrete data sections of 250 years. We calculate the diffusion length,  $\sigma$ , for each section by fitting its power spectrum with a model of a diffused power spectrum and a two-component model of the measurement system noise:

$$P = P_0 \exp(-k^2 \sigma^2) + P'_0 \exp(-k^2 (\sigma')^2) + |\hat{\eta}|^2, \quad (1)$$

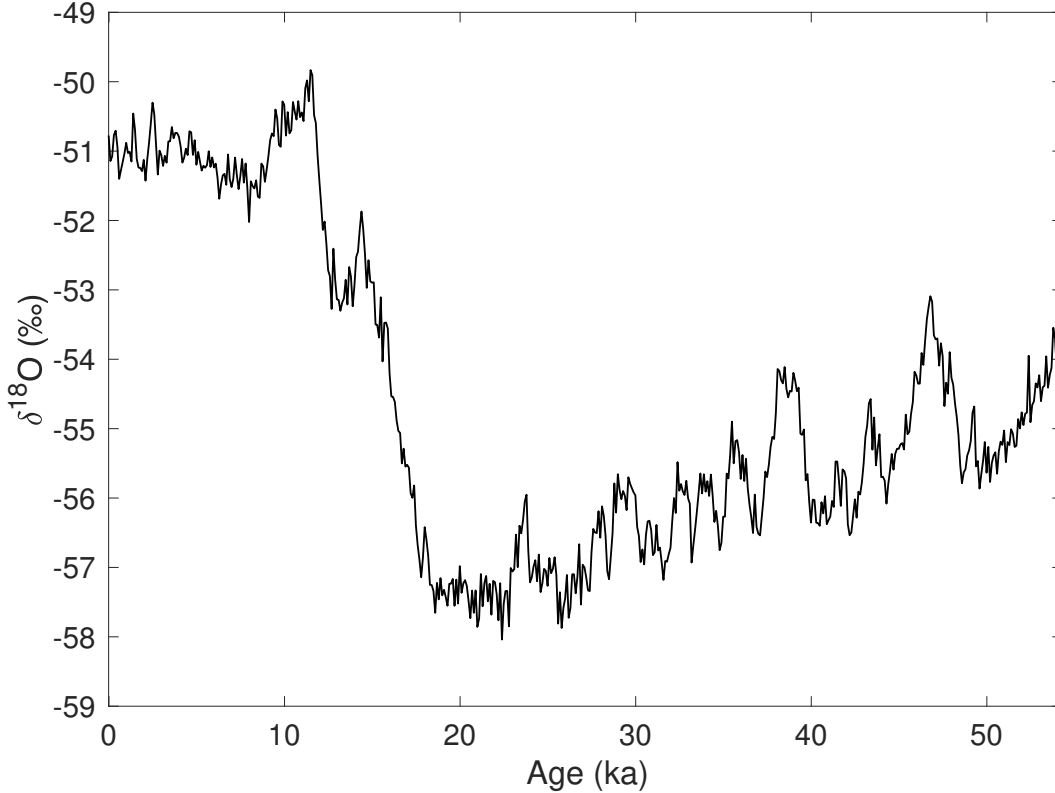


Figure 1: High-resolution  $\delta^{18}\text{O}$  record from the South Pole ice core (SPC14), shown as discrete 100-year averages for clarity, on the SP19 ice timescale (Winski et al., 2019).

155 where  $k$  is the wavenumber,  $|\hat{\eta}|^2$  is the measurement noise, and  $P_0$ ,  $P'_0$ , and  $\sigma'$  are vari-  
 156 able fitting parameters. The second term ( $P'_0 \exp(-k^2(\sigma')^2)$ ) accounts for the influence  
 157 of the CFA measurement system on the water-isotope data spectrum. Kahle et al. (2018)  
 158 found that this term does not completely eliminate the effect of system smoothing on  
 159 the spectrum; we therefore make an additional correction, based on the sequential mea-  
 160 surement of ice standards of known and differing isotopic composition, following Jones  
 161 et al. (2017b). This correction is small, accounting for only  $\sim 4\%$  of the total diffusion  
 162 length throughout the core. The uncertainty on  $\sigma$  is estimated conservatively as described  
 163 in Kahle et al. (2018) and varies from  $\pm 4\%$  to  $\pm 66\%$  (two s.d.) of the value throughout  
 164 the core.

165 Additionally, we correct the diffusion-length estimates to account for diffusion in the solid  
 166 ice, following Gkinis et al. (2014). This effect is also small, accounting for a maximum  
 167 of 4% of the total diffusion length at the bottom of the core. To calculate the solid-ice  
 168 diffusion length, we assume the modern borehole temperature profile  $T(z)$  remains con-  
 169 stant through time to find the diffusivity profile  $D_{ice}(z)$ , following Gkinis et al. (2014).  
 170 We use borehole temperature measurements from the nearby neutrino observatory (Price  
 171 et al., 2002). We assume a simple thinning function from a 1-D ice-flow model (Dans-  
 172 gaard and Johnsen, 1969) with a kink-height  $h_0 = 0.2$  for this calculation; the error in  
 173 this assumption is negligible for the small deviations in total thinning we are calculat-  
 174 ing. We subtract both the solid-ice and CFA diffusion lengths from the observations in  
 175 quadrature to produce our final diffusion-length data set. Further details on both correc-  
 176 tions are provided in the Supporting Information.

177 We calculate the diffusion length for each of the three water-isotope ratios measured on  
 178 the core. To combine the information from each isotope, we convert  $\delta^{17}\text{O}$  and  $\delta\text{D}$  dif-  
 179 fusion lengths to equivalent values for  $\delta^{18}\text{O}$ . For example, the  $\delta^{18}\text{O}$ -equivalent diffusion  
 180 length ( $\sigma_{18 \text{ from } 17}$ ) from the  $\delta^{17}\text{O}$  diffusion length ( $\sigma_{17}$ ) is:

$$\sigma_{18 \text{ from } 17}^2 = \sigma_{17}^2 \frac{D_{18}}{\alpha_{18}} \bigg/ \frac{D_{17}}{\alpha_{17}}, \quad (2)$$

181 where  $D$  and  $\alpha$  are the corresponding air diffusivity and solid-vapor fractionation fac-  
 182 tor for each isotope. Values for  $D$  and  $\alpha$  are given in the Supporting Information (Ma-  
 183 joube, 1970; Barkan and Luz, 2007; Luz and Barkan, 2010; Lamb et al., 2017). For the  
 184 single diffusion-length record used in our analysis, we take the mean of these three es-  
 185 timates for  $\sigma_{18}$ .

### 186 3 Forward Model

187 We use a forward model to relate the observational data sets to the variables of inter-  
 188 est. Figure 2 summarizes the data sets obtained from the ice-core measurements and the  
 189 calculations described above:  $\Delta\text{age}$ , water-isotope diffusion length, and annual-layer thick-  
 190 ness. We use these three data sets as our “observations” in a statistical inverse approach  
 191 to infer temperature, accumulation rate, and ice-thinning function.

192 Figure 3 illustrates the structure of the forward model, including a firn-densification com-  
 193 ponent, a water-isotope diffusion component, and a vertical strain (ice thinning) com-  
 194 ponent. We describe the individual components below.

#### 195 3.1 Firn Densification

196 The firn layer comprises the upper few tens of meters of the ice sheet where snow is pro-  
 197 gressively densifying into solid ice. As successive layers of snow fall on the surface of the  
 198 ice sheet, the increase in overburden pressure causes the underlying ice crystals to pack  
 199 closer together. The rate of densification is determined primarily by temperature and  
 200 accumulation rate. The Herron and Langway (1980) (HL) firn-densification model is the  
 201 benchmark empirical model, based on depth-density data from Greenland and Antarc-  
 202 tic ice cores. We model the depth-density profile of the firn using the HL framework due  
 203 to its simplicity and its good match with measurements of the modern South Pole firn  
 204 density.

205 We use a surface density  $\rho_0 = 350 \text{ kg m}^{-3}$ , consistent with measured values at the SPC14  
 206 site, and assume it remains constant through time (Fausto et al., 2018). The bottom of  
 207 the firn is constrained by a close-off density  $\rho_{co}$ , which we define as a function of tem-  
 208 perature (Martinerie et al., 1994). As temperature varies between  $-50$  and  $-60^\circ\text{C}$ , close-  
 209 off density varies in a small range between  $831.5$  and  $836.4 \text{ kg m}^{-3}$ .

210 We use the analytical formulation of the HL model, which assumes an isothermal firn.  
 211 If either temperature or accumulation rate changes on short timescales, a transient for-  
 212 mulation of the model would be required to reflect propagation through the firn column.  
 213 Although our temperature and accumulation-rate inputs vary through time, the timescale  
 214 of those variations (*e.g.* 10 ka for  $\sim 6^\circ\text{C}$  change in temperature) is large enough that the  
 215 steady-state approximation is acceptable. To test this assumption, we ran our forward  
 216 model with a transient formulation of the HL model (Stevens et al., 2020) and found no  
 217 difference in the results. Since the transient model is more computationally expensive,  
 218 we use the analytical formulation.

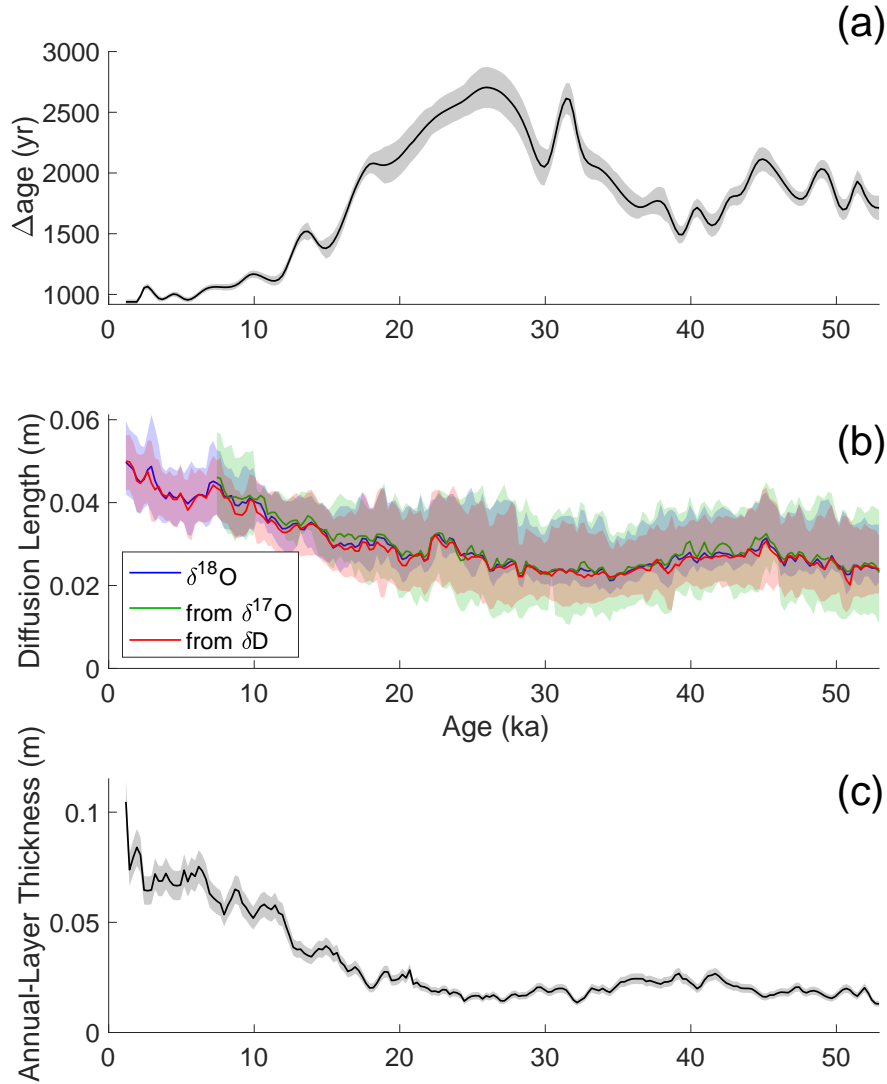


Figure 2: Data sets from SPC14 used to optimize the inverse problem, each averaged over bins of 250 years and plotted with uncertainty representing two s.d. Panel (a) shows annual-layer thickness data, panel (b) shows  $\Delta\text{age}$ , and panel (c) shows water-isotope diffusion lengths. Diffusion lengths from  $\delta^{17}\text{O}$  (green) and  $\delta\text{D}$  (red) have been converted to  $\delta^{18}\text{O}$ -equivalent values.

### 219 3.2 Modeling $\Delta\text{age}$

220 Modeled  $\Delta\text{age}$  is given by the difference in the modeled age of the ice and the gas at the  
 221 lock-in depth. We define the lock-in depth at a density of  $10 \text{ kg m}^{-3}$  less than the close-

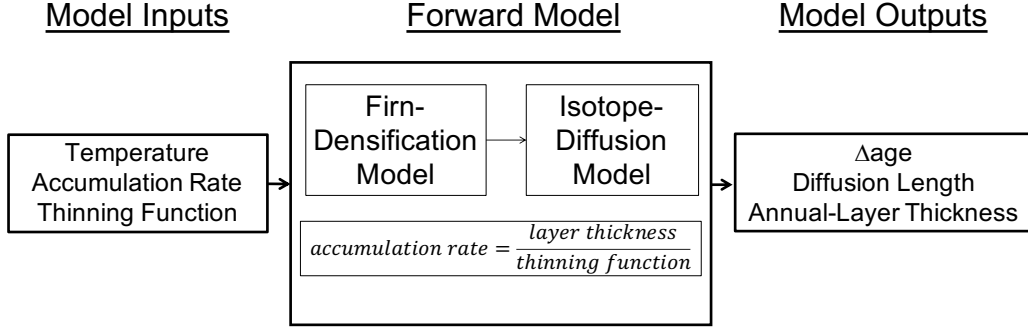


Figure 3: Illustration of the forward model, which includes firn densification, water-isotope diffusion, and vertical strain. Together, these components relate the variables of interest (temperature, accumulation rate, and thinning function) to the observational data sets ( $\Delta$ age, layer thickness, and diffusion length) shown in Figure 2.

222 off density (Blunier and Schwander, 2000). The age of the ice at this depth is estimated  
 223 directly from the depth-density profile. We estimate the age of the gas at the lock-in depth  
 224 (LID) using the parameterization in Buizert et al. (2013):

$$gas\ age(\rho_{LID}) = \frac{1}{1.367} \left( 0.934 \times \frac{(DCH)^2}{D_{CO_2}^0} + 4.05 \right), \quad (3)$$

225 where DCH is the diffusive column height, defined as the lock-in depth minus a 3 m con-  
 226 vective zone at the surface where firn air is well-mixed with the atmosphere.  $D_{CO_2}^0$  is  
 227 the free air diffusivity of  $CO_2$  defined in Schwander et al. (1988) and Buizert et al. (2012).  
 228 The lock-in depth is defined as the depth at which the effective molecular diffusivity of  
 229 the gas is reduced to one thousandth of the free air diffusivity (Buizert et al., 2013).

### 230 3.3 Modeling Diffusion Length

The combined effects on the isotope profile due to diffusion and firn densification are given by:

$$\frac{\partial \delta}{\partial t} = D \frac{\partial^2 \delta}{\partial z^2} - \dot{\epsilon} z \frac{\partial \delta}{\partial z}, \quad (4)$$

231 where  $\delta$  is the isotope ratio,  $D$  is the diffusivity coefficient,  $\dot{\epsilon}$  is the vertical strain rate,  
 232 and  $z$  is the vertical coordinate assuming an origin fixed on an arbitrary sinking layer  
 233 of firn (Johnsen, 1977; Whillans and Grootes, 1985).

234 The diffusivity coefficient  $D_x$  of each isotope  $x$  depends on the temperature and density  
 235 profile of the firn column Whillans and Grootes (1985); Johnsen et al. (2000):

$$D_x = \frac{m p D_x^{air}}{RT \alpha_x \tau} \left( \frac{1}{\rho} - \frac{1}{\rho_{ice}} \right), \quad (5)$$

236 where  $m$  is the molar weight of water,  $p$  is the saturation pressure over ice at temper-  
 237 ature  $T$  and with gas constant  $R$ ,  $D_x^{air}$  is the diffusivity of each isotopologue through  
 238 air,  $\alpha_x$  is the fractionation factor for each isotopic ratio in water vapor over ice,  $\tau$  is the  
 239 tortuosity of the firn,  $\rho$  is the firn density, and  $\rho_{ice}$  is the density of ice. Values for these  
 240 parameters are given in the Supporting Information.

241 Using the output from the firn-densification model, we calculate water-isotope diffusion  
 242 through the depth-density profile. First, the density profile is used to calculate the dif-  
 243 fusivity of each isotope based on Equation 5. We then solve for the diffusion length  $\sigma_{firn}$   
 244 of a particular isotope ratio in terms of its effective diffusivity coefficient  $D$  and the firn  
 245 density  $\rho$  (Gkinis et al., 2014):

$$\sigma_{firn}^2(\rho) = \frac{1}{\rho^2} \int_{\rho_0}^{\rho} 2\rho^2 \left( \frac{d\rho}{dt} \right)^{-1} D(\rho) d\rho, \quad (6)$$

246 where  $\rho_0$  is the surface density and  $\frac{d\rho}{dt}$  is the material derivative of the density. To cal-  
 247 culate the diffusivity  $D$ , we use an atmospheric pressure of 0.7 atm (Severinghaus et al.,  
 248 2001), which we assume to be constant through time.

249 Cumulative vertical strain significantly thins layers in the ice. The thinning function is  
 250 defined as the fractional amount of thinning that has occurred at a given depth in the  
 251 ice sheet. We account for the effects of vertical strain on our modeled firn diffusion length,  
 252  $\sigma_{firn}$ , using a thinning function  $\Gamma$ . We model the diffusion length measured in the ice  
 253 core as  $\sigma_{icecore}$ :

$$\sigma_{icecore} = \sigma_{firn} \times \Gamma. \quad (7)$$

254 Recall that when we compare the modeled diffusion length with the observations, the  
 255 observations have been corrected for diffusion in solid ice.

### 256 3.4 Modeling Annual-Layer Thickness

257 Annual-layer thickness  $\lambda$  is given by the accumulation rate  $A$  multiplied by the thinning  
 258 function  $\Gamma$ :

$$\lambda = A \times \Gamma. \quad (8)$$

## 259 4 Statistical Inverse Approach

260 We use a Bayesian statistical approach to produce an ensemble of possible solutions to  
 261 our inverse problem. Through many iterations, we use the forward model described above  
 262 to solve our forward problem and determine the range of possible model inputs. This  
 263 forward problem is described by the following equation, where the forward model,  $G$ , cal-  
 264 culates the modeled observables, or data parameters,  $d$  as a function of unknown input  
 265 variables, or model parameters,  $m$ :

$$G(m) = d. \quad (9)$$

266 Our forward model  $G$  is nonlinear and cannot be solved analytically. Instead, we use a  
 267 Monte Carlo approach to solve the inverse problem by testing many instances of  $m$  through  
 268 the forward model  $G$  to find the output  $d$  that best matches the observations  $d_{obs}$ . The  
 269 theory and practical implementation of this approach are detailed in the Supporting In-  
 270 formation (Metropolis et al., 1953; Tarantola, 1987; Mosegaard and Tarantola, 1995; Gel-  
 271 man et al., 1996; Mosegaard, 1998; Khan et al., 2000; Mosegaard and Sambridge, 2002;  
 272 Mosegaard and Tarantola, 2002; Steen-Larsen et al., 2010).

273 We incorporate *a priori* information about model parameters based on their modern val-  
 274 ues and our best guess of how they have varied through time. We include this *a priori*  
 275 information by creating bounds on the allowable model space to explore. If the algorithm  
 276 proposes a solution  $m_x$  that falls outside of our bounded model space,  $m_x$  is disregarded  
 277 and another solution is evaluated.

278 We also determine initial guesses  $m_1$  for each parameter. Initializing the problem at what  
 279 is judged to be a reasonable solution  $m_1$  helps to avoid non-physical solutions (MacAyeal,  
 280 1993; Gudmundsson and Raymond, 2008). We design initial guesses for each parame-  
 281 ter that are simplified versions of our best initial guess, allowing higher-frequency infor-  
 282 mation to be inferred from the optimization. The initial guess of temperature is a step-  
 283 function version of the water-isotope record. The initial guess for the thinning function  
 284 is the output of a Dansgaard and Johnsen (1969) (DJ) ice-flow model. This simple model  
 285 produces an approximation of the dynamics acceptable at many ice-core sites (Hammer  
 286 et al., 1978). We use a kink height of  $h_0 = 0.2$  to simulate the flank flow at the SPC14  
 287 site. To produce an initial guess for accumulation rate, we divide the layer-thickness data  
 288 by this thinning function and approximate the result with a simplified step function.

289 Each parameter is bounded based on naïve expectations for its variability. For temper-  
 290 ature, we bound the model space with an upper and lower scaling of the step-function  
 291 initial guess version of the water-isotope record. We create an envelope based on pre-  
 292 vious estimates of glacial-interglacial temperature change in Antarctica, which allows for  
 293 solutions with glacial-interglacial changes as small as  $0.5^\circ\text{C}$  and as large as  $15^\circ\text{C}$ . For ac-  
 294 cumulation rate, the bounded model-parameter range is an envelope about our initial  
 295 guess defined as  $\pm 0.02 \text{ m yr}^{-1}$ . Given the surface and Holocene accumulation-rate fluc-  
 296 tuations at South Pole described in Lilien et al. (2018), this range is a reasonable limit  
 297 on accumulation rate, while still allowing variation in the values tested in each  $m$ . For  
 298 the ice-equivalent thinning function, we enforce a value of one at the surface but do not  
 299 provide further constraints on the model space because it is effectively constrained by  
 300 the bounds on accumulation rate and layer thickness.

## 301 5 *A posteriori* Results

### 302 5.1 Probability Distributions

303 The resulting solutions  $m$  from our inverse approach are described by the *a posteriori*  
 304 distribution. To visualize the high-dimensional *a posteriori* distribution, we plot prob-  
 305 ability distributions for each parameter. Rather than create separate probability distri-  
 306 butions for each of the many parameters in our model space, we plot each probability  
 307 distribution successively in a single figure to visualize the entire model space at once. Fig-  
 308 ure 4 shows our results, with the model inputs on the left and outputs on the right. The  
 309 grey shading shows successive probability distributions. A vertical slice through the shad-  
 310 ing in each plot represents the probability distribution for a particular parameter (re-  
 311 call that a parameter represents the value of a variable at a specified model timestep,  
 312 *i.e.* the value of temperature at the 4th timestep). How often a particular value is ac-  
 313 cepted for each parameter is represented by the shading, where darker shading denotes  
 314 values that were accepted more often. The solid magenta curves describe the initial guess  
 315 for each parameter, and the dashed magenta curves describe the bounded model space  
 316 (for temperature and accumulation rate). The right three panels of Figure 4 illustrate  
 317 how well the modeled observables  $d(m)$  match with the observations  $d_{obs}$  throughout the  
 318 collection of solutions.

### 319 5.2 Sensitivity of Results

320 We evaluate the sensitivity of our results to different choices made in the formulation  
 321 of the forward and inverse problems. Since we opted to keep the surface density  $\rho_0$  in  
 322 the firn-densification model constant through time, we tested the sensitivity of a change.  
 323 We tested two alternate values of surface density  $\rho_{surface}$  ( $450 \text{ kg m}^{-3}$  and  $550 \text{ kg m}^{-3}$ );  
 324 we find no significant change in the results. We also evaluated the sensitivity to differ-  
 325 ent initial guesses for each parameter. Altering the initial guesses within the model space

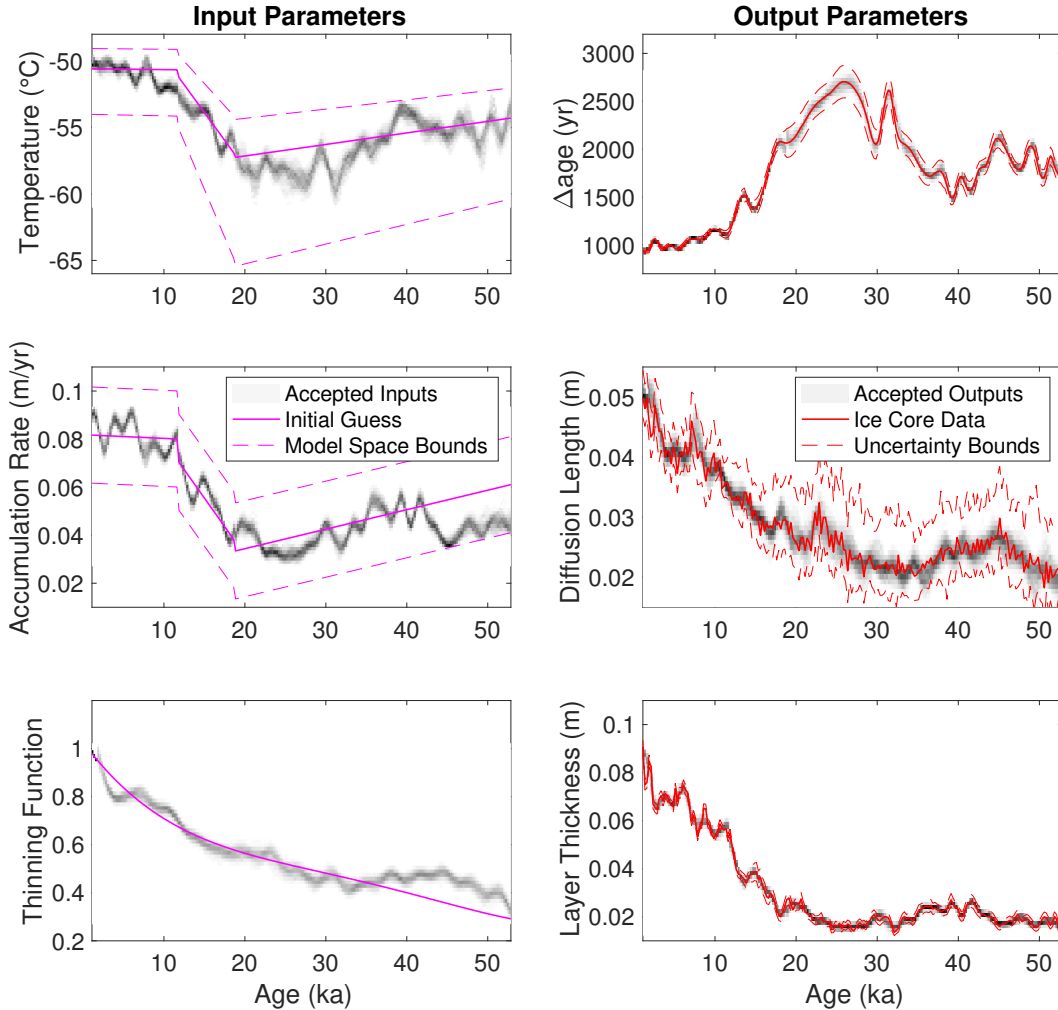


Figure 4: Results of the Monte Carlo inverse calculations, showing the *a posteriori* distribution result compared with *a priori* information. The grey shading in each panel represents probability distributions for each parameter from the *a posteriori* distribution, where darker shading signifies greater likelihood. Left panels show the initial guesses (solid magenta) and model bounds (dashed) for the input parameters: temperature, accumulation rate, and thinning. Right panels show the observational data (solid red) and prescribed uncertainties (dashed) for the output parameters:  $\Delta$ age, diffusion length, and layer thickness.

326 bounds do not affect the final results. Additionally, including higher-frequency *a priori*  
 327 information in our initial guesses does not change the results. For example, we evalu-  
 328 ated initial guesses of constant values for each of temperature, accumulation rate, and  
 329 thinning function. These extremely simplified initial guesses produce results indistinguish-  
 330 able from those that include the high-frequency variability of each comparison data set,  
 331 but require many more iterations to reach an equilibrium solution. As recommended in  
 332 Gudmundsson and Raymond (2008), we opted for a middle-ground approach that saves  
 333 time by setting the initial guess close to the expected answer but relies on the optimiza-  
 334 tion to obtain high-frequency information. We also tested the sensitivity of the results  
 335 to each data set individually, as detailed in the Supporting Information. One key conclu-  
 336 sion from these tests is that all three data sets ( $\Delta$ age, layer thickness, and diffusion

length) provide important information for producing a well-constrained result (Figure S3).

## 6 Discussion

Our reconstructions for accumulation rate, ice thinning, and temperature compare well with estimates from simpler calculations and independent data. In general, the results are in agreement with naïve expectations, but with some important differences. Because the accumulation-rate and thinning reconstructions are fundamentally linked through Equation 8, we discuss them together. We then compare our reconstruction for temperature with the traditional water-isotope paleothermometer, and discuss the broader implications of our results. The *a posteriori* distribution is near-Gaussian, and in this section we plot its mean and standard deviation rather than the full probability distributions. Recall that the *a posteriori* distribution comprises only accepted solutions, a subset of all iterations.

### 6.1 Accumulation Rate and Thinning Function

Figure 5 shows the results for the thinning function (panel (a)) and accumulation rate (panel (b)). The grey shading denotes a band of two s.d. of the *a posteriori* distribution. In general, thinning functions are expected to be smooth and to decrease monotonically because they integrate the total thinning experienced at a given depth, as illustrated by the results of a 1-D Dansgaard-Johnsen (DJ) model with  $h_0 = 0.2$  (red curve, panel (a)). However, the SPC14 site is far from an ice divide such that variations in the bed topography upstream can create more complex thinning histories (e.g., Parrenin et al., 2004). Thus, the thinning function result is similar to the DJ-model output, but contains additional higher-frequency variations. To evaluate the plausibility of these variations in the primary reconstruction, we compare with two other independent estimates of the thinning function, an ice-flow-model thinning function and a  $\delta^{15}\text{N}$ -based thinning function.

First, we compare the primary thinning function with one calculated from an ice-flow model. We use a 2.5-D flowband model (Koutnik et al., 2016) forced with observations of the bedrock topography and the accumulation-rate pattern. Details of the model setup are given in the Supporting Information (Nye, 1963; Looyenga, 1965; Gades et al., 2000; Neumann et al., 2008; Catania et al., 2010; Jordan et al., 2018). The resulting thinning function is best considered in two segments. The thinning function for the past 10 ka (solid black line in Figure 5) is well constrained because the flowline is known (Lilien et al., 2018) and the bed topography has been measured along the flowline (Figure S6). The key result is that the bed undulations along the flowline cause the same structure as is inferred in the primary thinning function. The “reversal” in the thinning function at 7 ka, where deeper layers have thinned less than shallower layers, matches well in both the primary and ice-flow-model thinning functions. This feature is caused by an overdeepening in the bed topography (Figure S10).

For ages older than 10 ka, we do not know where the ice originated and thus cannot use the ice-flow model to determine the thinning function with confidence. Instead, we aim to evaluate whether the primary thinning function is physically plausible, given what we know about the bed topography in the region. Using airborne radar measurements (Forsberg et al., 2017) to guide a simulated but realistic bed, we show that the ice-flow model (black dashed line) can approximately match the magnitude and structure of the primary thinning function. Therefore, the primary thinning function is consistent with expectations, given plausible variations in bedrock topography.

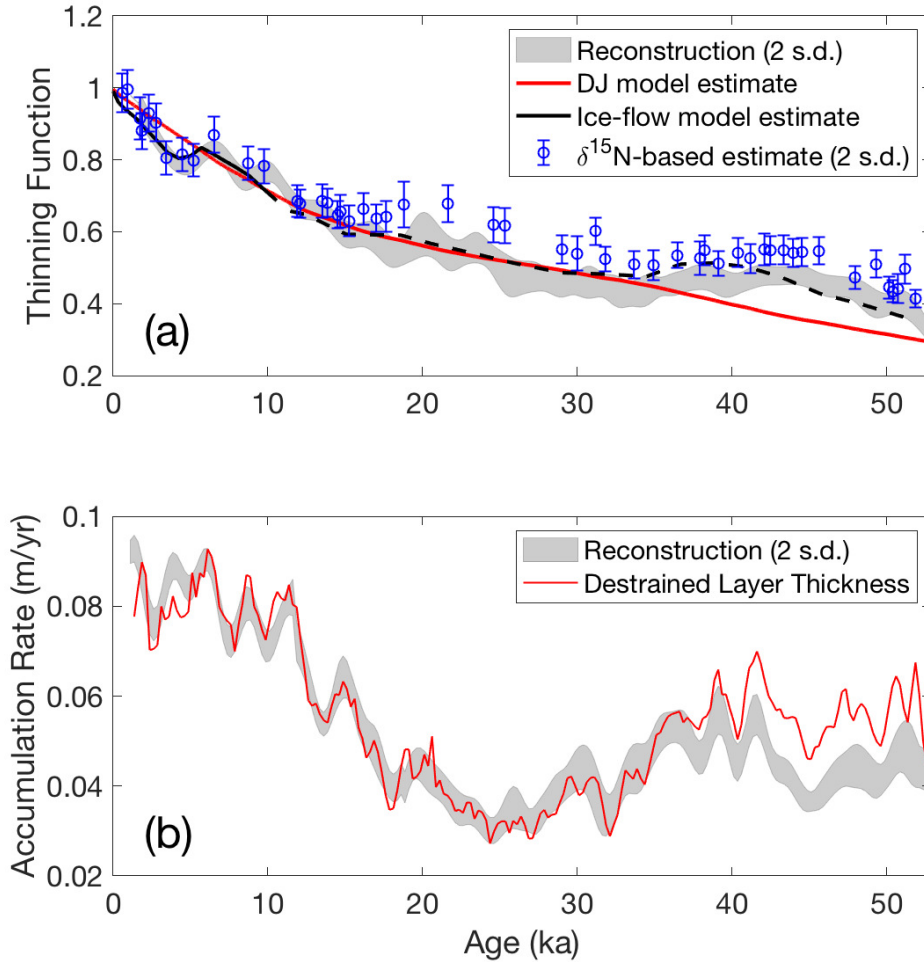


Figure 5: Reconstructions of accumulation rate and thinning function for SPC14. Two s.d. (grey shading) of the *a posteriori* distribution is plotted for each reconstruction alongside comparison estimates. Panel (a) shows the primary thinning function reconstruction (grey) compared to a DJ-model output with  $h_0 = 0.2$  (red), an ice-flow-model thinning function from a 2.5-D flowband model (black), and a  $\delta^{15}\text{N}$ -based thinning function with error bars showing two s.d. uncertainty (blue). The solid black curve shows where the ice-flow-model thinning function is well constrained by data, and the dashed black curve shows where the bed topography is simulated. Panel (b) shows the accumulation-rate reconstruction compared to the layer-thickness data destrained by the same DJ-model output (red).

384 Second, we compare the primary thinning function with a  $\delta^{15}\text{N}$ -based thinning function  
 385 (blue line; error bars show two s.d. uncertainty). We obtain this estimate using measure-  
 386 ments of the  $\delta^{15}\text{N}$  of  $\text{N}_2$  gas, data reported in Winski et al. (2019), following the meth-  
 387 ods described in Parrenin et al. (2012). The enrichment of  $\delta^{15}\text{N}$  in the ice core is a lin-  
 388 ear function of the original diffusive column height (DCH) of the firn due to the signal of  
 389 gravitational fractionation recorded at the lock-in depth (LID) (Sowers et al., 1992;  
 390 Buizert et al., 2013). To determine the thinning that has occurred in the ice sheet, the  
 391 ice-equivalent LID is compared to the “ $\Delta$ depth” of the ice core, which reflects the thick-

392 ness of ice that originally comprised the firn column at the ice-sheet surface. The  $\Delta\text{depth}$   
 393 is closely related to the  $\Delta\text{age}$  and is the difference in depth in the ice core of the same  
 394 climate event. The thinning function  $\Gamma$  is then given by (Parrenin et al., 2012):

$$\Gamma = \frac{\Delta\text{depth}}{A \times \text{LID}}, \quad (10)$$

395 where  $A$  is a scaling factor that accounts for the ice-equivalent thickness of the original  
 396 firn column (Winski et al., 2019). Full details on this approach and its uncertainties are  
 397 given in the Supporting Information.

398 Figure 5 panel (a) shows that the structure of the  $\delta^{15}\text{N}$ -based thinning function agrees  
 399 well with the primary reconstruction, showing the same high-frequency variations and  
 400 mean estimates whose error bars overlap. At ages greater than about 15 ka, the  $\delta^{15}\text{N}$ -  
 401 based thinning function appears shifted towards higher values (less thinning) on aver-  
 402 age. Differences between firn-model results and constraints from  $\delta^{15}\text{N}$  have previously  
 403 been note for sites at very cold temperatures (Freitag et al., 2013; Bréant et al., 2017);  
 404 this has been referred to colloquially as the “ $\delta^{15}\text{N}$  problem”. The agreement between  
 405 our primary reconstruction and the  $\Delta\text{depth}$  calculation shows that at least at South Pole,  
 406 this discrepancy is within the uncertainties on both. We emphasize that the uncertain-  
 407 ties for the  $\Delta\text{depth}$  calculation are not depth-independent; many known sources of er-  
 408 ror are expected to be systematic. For example, if the WAIS Divide  $\Delta\text{age}$  data set were  
 409 systematically too large during the glacial period, correcting for this would result in smaller  
 410 estimates for the SPC14  $\Delta\text{depth}$ , and therefore smaller values (more thinning) in the  $\delta^{15}\text{N}$ -  
 411 based thinning function. The same adjustment to  $\Delta\text{age}$  results in no significant change  
 412 in the primary thinning function, thus improving the agreement between the means of  
 413 the two independent estimates. Similarly, the scaling factor of  $A$  in Equation 10, whose  
 414 mean value is taken from modern observations of the firn column, is unlikely to be con-  
 415 stant in time; this would also systematically affect the  $\delta^{15}\text{N}$ -based thinning function with-  
 416 out changing the results of our primary reconstruction.

417 For comparison with the accumulation-rate reconstruction, Figure 5 panel (b) shows the  
 418 raw annual-layer thickness data corrected for thinning from the 1-D DJ-model output  
 419 (red curve). We note that high-frequency variability in the accumulation-rate reconstruc-  
 420 tion is limited by our enforcing smooth perturbations at each iteration (see Supporting  
 421 Information). The low-frequency variability, on the other hand, reflects new information  
 422 resulting from the optimization. In particular, the thinning function reversal between  
 423 40 and 50 ka is reflected by a significantly smaller accumulation rate than would be in-  
 424 ferred using a DJ model.

425 To produce an estimate of the accumulation-rate history that incorporates the high-frequency  
 426 information of the SPC14 timescale (Winski et al., 2019) and is also consistent with the  
 427 thinning results discussed above, we combine information from all available measurements  
 428 (Figure 6). We destrain the SP19 layer thicknesses using the mean of the primary thin-  
 429 ning function and the  $\delta^{15}\text{N}$ -based thinning function. We determine uncertainty for this  
 430 estimate (two s.d.) by destraining the layer-thickness data with the uncertainty bounds  
 431 of each thinning function (blue and red representing the primary and  $\delta^{15}\text{N}$ -based thin-  
 432 ning functions, respectively). This represents our best estimate for the accumulation-  
 433 rate history in SPC14.

## 434 6.2 Temperature Reconstruction

435 The temperature reconstruction is shown in Figure 7. For comparison, we show two scaled  
 436 versions of the measured  $\delta^{18}\text{O}$ , corrected for secular variations in the  $\delta^{18}\text{O}$  of sea-water,  
 437 following Bintanja and van de Wal (2008). Recall that while we used diffusion length de-  
 438 termined from the  $\delta^{18}\text{O}$  power spectrum in our reconstruction, we do not use the  $\delta^{18}\text{O}$

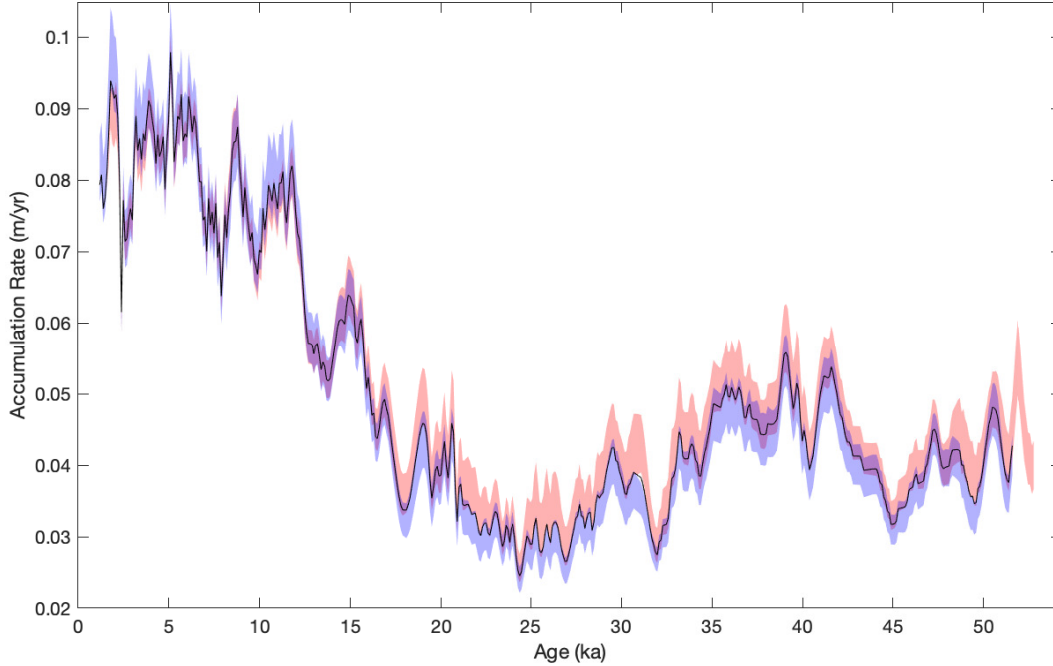


Figure 6: Accumulation rate in SPC14, averaged to 100-year resolution. The accumulation rate (black line) is calculated from the layer-thickness data divided by the mean of the primary and  $\delta^{15}\text{N}$ -based thinning functions shown in Figure 5(a). Also shown is the uncertainty (2 s.d.) as calculated individually from the primary thinning function (red) and the  $\delta^{15}\text{N}$ -based thinning function (blue).

439 values; hence, these comparisons serve as an independent calibration of the traditional  
 440 water-isotope thermometer, similar to what has been done previously with borehole ther-  
 441 mometry (Cuffey et al., 1995, 2016) but maintaining higher-frequency information. The  
 442 red curve in Figure 7 uses a scaling of  $\partial(\delta^{18}\text{O})/\partial T = 0.8\text{‰}\text{C}^{-1}$ , which is both the ob-  
 443 served modern surface isotope-temperature relationship at the site (Fudge et al., 2020)  
 444 and the value commonly used in the literature for Antarctica (e.g. Jouzel et al., 2003;  
 445 Masson-Delmotte et al., 2008). The black curve shows the best-fit linear relationship be-  
 446 tween  $\delta^{18}\text{O}$  and the mean of our reconstruction; this has a significantly greater slope of  
 447  $0.98\text{‰}\text{C}^{-1}$ .

448 A single  $\partial(\delta^{18}\text{O})/\partial T$  scaling does not capture all of the variability in our  $T$  reconstruc-  
 449 tion. Nevertheless, the overall agreement is excellent, and there is no evidence of the large  
 450 change in scaling that has been observed in Greenland ice cores (Cuffey et al., 1995) and  
 451 attributable primarily to changes in the seasonality of precipitation (Steig et al., 1994;  
 452 Werner et al., 2000). The correlation coefficient between  $\delta^{18}\text{O}$  and the mean of our en-  
 453 semble is 0.93. As already noted and as is apparent in Figure 7, our calibration yields  
 454 a significantly greater slope than has been generally used in previous work. This is con-  
 455 sistent with isotope-modeling results that show that the sensitivity of  $\delta^{18}\text{O}$  to temper-  
 456 ature should increase at sites with colder mean-annual temperatures and higher eleva-  
 457 tions in Antarctica. For example, Markle (2017) obtains  $\partial(\delta^{18}\text{O})/\partial T \sim 0.8\text{‰}\text{C}^{-1}$  for  
 458 a location like WAIS Divide, in agreement with the borehole temperature calibration,  
 459 and  $\partial(\delta^{18}\text{O})/\partial T \sim 1\text{‰}\text{C}^{-1}$  for South Pole. This difference in sensitivity occurs be-  
 460 cause air masses traveling to higher elevations are on different moist isentropic surfaces,  
 461 and experience greater rainout for a given change in temperature (Bailey et al., 2019).

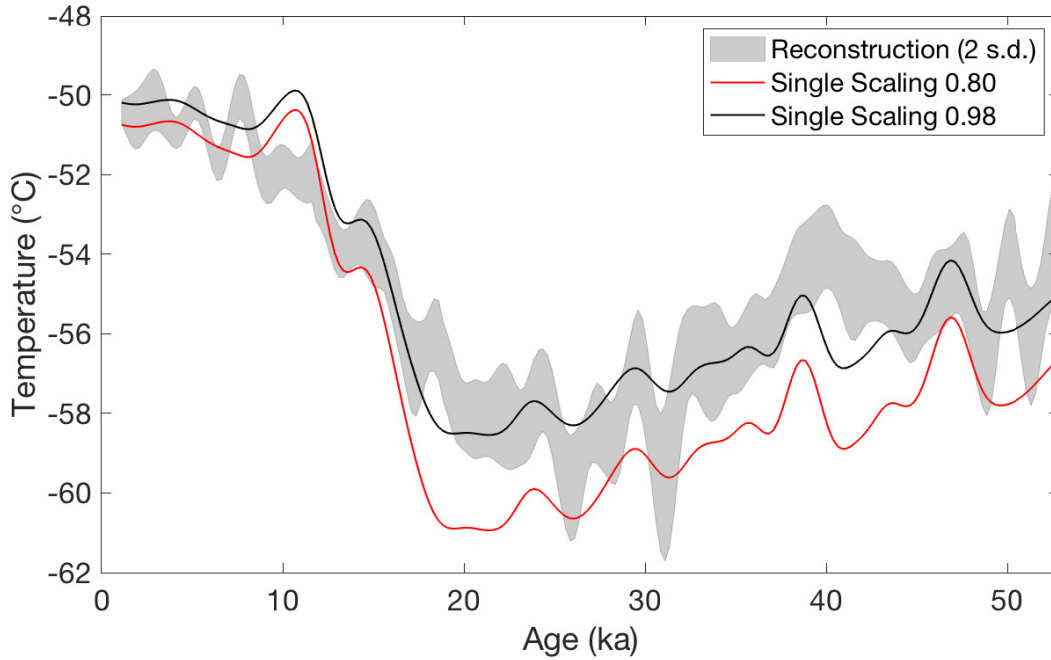


Figure 7: Reconstruction of temperature and relationship with  $\delta^{18}\text{O}$ . Grey shading shows two s.d. of the *a posteriori* distribution. Solid lines show scaled versions of the  $\delta^{18}\text{O}$ , discretely averaged to 250-year resolution and smoothed with a 3000-year lowpass filter. The water isotopes are scaled by  $0.8\text{‰}\text{°C}^{-1}$ , the modern surface relationship (red), and by  $0.98\text{‰}\text{°C}^{-1}$ , the calibrated linear relationship with the mean of the temperature reconstruction (black).

462 We use our temperature reconstruction to determine the magnitude of glacial-interglacial  
 463 temperature change at South Pole. We define this change as the difference in the mean  
 464 temperature within the intervals of 0.5 - 2.5 ka and 19.5 - 22.5 ka. Note that our recon-  
 465 struction ends at 0.5 ka, not the present, because the upper  $\sim 500$  years of the record is  
 466 in the firn; hence,  $\Delta\text{age}$  is undefined and diffusion of water isotopes is still in progress.  
 467 The choice of the last glacial maximum (LGM) window avoids the prominent warming  
 468 of the Antarctic Isotope Maximum (AIM2) event. Our mean reconstruction for SPC14  
 469 yields a change of  $7.5\pm 0.8\text{°C}$  (one s.d.). However, because SPC14 was drilled far from  
 470 the divide, deeper ice in the core originated increasingly farther upstream. We can cor-  
 471 rect for this using modern ice-flow data and surface observations. Fudge et al. (2020) show  
 472 that the magnitude of the adjustment, based on observations of the  $\delta^{18}\text{O}$  surface gra-  
 473 dient and surface-temperature lapse rate of  $10\text{°C km}^{-1}$ , is roughly a  $1\text{°C}$  warming cor-  
 474 rection in the glacial period. Thus, our best estimate for the glacial-interglacial temper-  
 475 ature change at the South Pole site is  $6.3\pm 0.8\text{°C}$  (one s.d.). We show the ice-flow-corrected,  
 476 calibrated  $\delta^{18}\text{O}$  record in Figure 8; this should be considered the best current estimate  
 477 of temperature-calibrated isotope variations at South Pole through the last 54,000 years.  
 478 We calculate the uncertainty (two s.d.) by taking into account the correlation coefficient  
 479 between the reconstruction and the scaled-isotope estimate.

480 Our results from SPC14 indicate a 2 to  $3.5\text{°C}$  lower glacial-interglacial surface temper-  
 481 ature change than reconstructed from other ice cores in east Antarctica, which is gen-  
 482 erally taken to be  $9\text{°C}$  (Parrenin et al., 2013). This difference cannot readily be attributed  
 483 to elevation change at South Pole, which is unlikely to have been more than 100 m thin-  
 484 ner during the last glacial maximum (e.g., Pollard and DeConto, 2009), thus account-

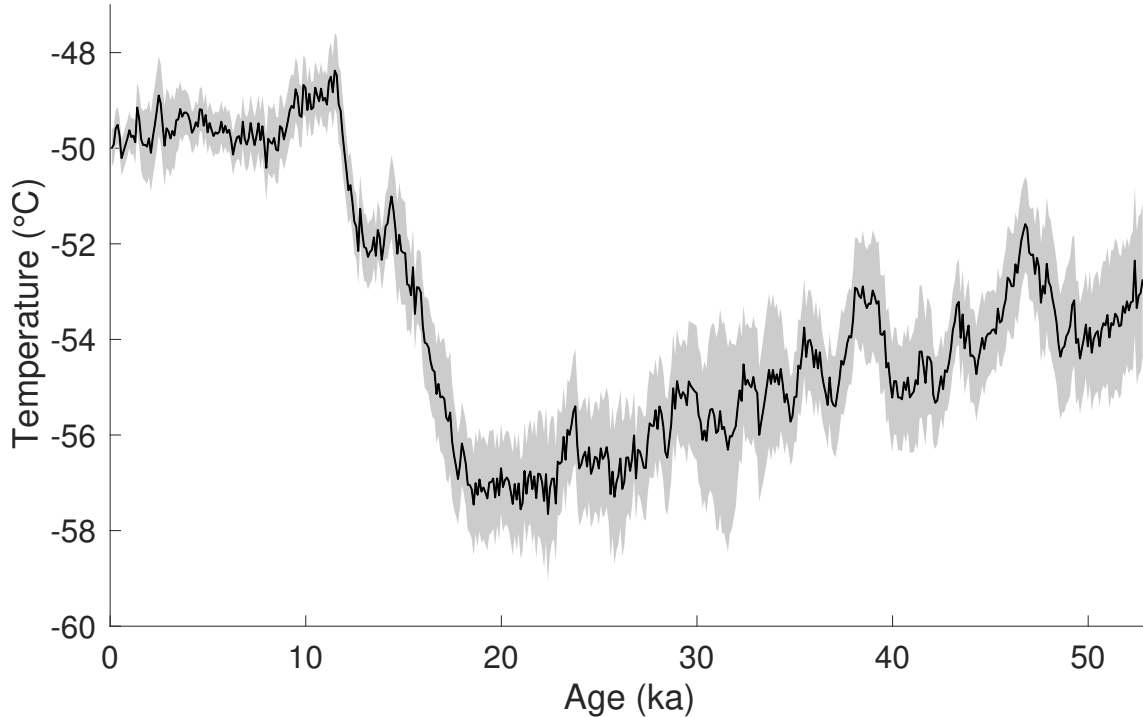


Figure 8: Advection-corrected temperature at South Pole, from scaled  $\delta^{18}\text{O}$ , averaged to 100-year resolution. The  $\delta^{18}\text{O}$  is scaled by  $0.98\text{‰}\text{°C}^{-1}$ , the best-fit relationship with the independent temperature reconstruction from our inverse method, and corrected for ice flow following Fudge et al. (2020). Uncertainty (two s.d.) takes into account the correlation coefficient between the temperature reconstruction and the scaled-isotope estimate.

485 ing for at most about  $1\text{°C}$  of the difference. Instead, we suggest that the commonly-used  
 486  $9\text{°C}$  value, which is based on water isotopes unconstrained by the independent estimates  
 487 we use here, is too large. Importantly, this may resolve an apparent disagreement, first  
 488 recognized at least three decades ago (Crowley and North, 1991), between ice-core based  
 489 temperature estimates and results from general circulation models (GCMs), which do  
 490 not produce cold-enough LGM temperatures unless surface elevations significantly higher  
 491 than present are assumed (e.g., Masson-Delmotte et al., 2006; Schoenemann et al., 2014;  
 492 Masson-Delmotte et al., 2013). Such GCM estimates are in better agreement with our  
 493 results if corrected for the prescribed elevation changes, consistent with the smaller changes  
 494 in East Antarctic ice elevations during the LGM indicated by more recent results (Briggs  
 495 et al., 2014; Argus et al., 2014; Roy and Peltier, 2015) than those suggested by earlier  
 496 work (e.g., Peltier, 2004).

## 497 7 Conclusions

498 The South Pole ice core (SPC14) provides the opportunity to obtain reconstructions of  
 499 important climate variables using multiple independent constraints. SPC14 has an empiri-  
 500 cal measure of the gas-age ice-age difference,  $\Delta\text{age}$ , obtained independent of firm den-  
 501 sification modeling (Epifanio et al., 2020). We also present a new continuous record of  
 502 water-isotope diffusion length. Both  $\Delta\text{age}$  and diffusion length depend on firm proper-  
 503 ties, which in turn depend on the snow-accumulation rate and firm temperature. The water-  
 504 isotope diffusion length provides an important additional constraint on the ice-thinning

505 function, which relates measured layer thickness with the original accumulation rate at  
 506 the surface. Layer thickness variations in SPC14 are well-constrained by the ice timescale  
 507 for the core, developed by annual-layer counting through the Holocene and by stratigraphic  
 508 matches with the well-dated West Antarctic Ice Sheet Divide ice core (Winski et al., 2019).  
 509 We have used a statistical inverse approach to combine information from all these data  
 510 sets to obtain an ensemble of self-consistent temperature, accumulation-rate, and ice-  
 511 thinning histories.

512 Our estimate of the thinning function for SPC14 indicates greater variations in thinning  
 513 rate, and significantly less thinning at depth, than can be captured with a simple one-  
 514 dimensional ice-flow parameterization such as the commonly-used Dansgaard-Johnsen  
 515 model. Variations in thinning comparable in timing and magnitude to our results are  
 516 supported by a 2.5-D flowband model that accounts for variations in bedrock topogra-  
 517 phy upstream of the drill site. Our results are further supported by measurements of the  
 518  $\delta^{15}\text{N}$  of  $\text{N}_2$ , which provide an additional independent estimate of thinning, based on the  
 519 “ $\Delta$ depth” calculation of firn-layer thickness following Parrenin et al. (2012). The thin-  
 520 ning function reconstruction is particularly important because SPC14 was drilled more  
 521 than 200 km away from the ice divide and the surface velocity is high ( $10 \text{ m yr}^{-1}$ ) (Casey  
 522 et al., 2014).

523 Our temperature reconstruction serves two important purposes. First, it provides the  
 524 first empirical, high-frequency estimate of temperature for an East Antarctic ice-core site  
 525 that does not depend on the traditional water-isotope paleothermometer. It thus enables  
 526 an independent calibration of the isotope-temperature sensitivity,  $\partial(\delta^{18}\text{O})/\partial T$ , similar  
 527 to what has been done in central Greenland and in West Antarctica using borehole ther-  
 528 mometry (Cuffey et al., 1995, 2016). Moreover, our approach preserves additional high-  
 529 frequency information that is not available from the highly diffused borehole-temperature  
 530 measurements. Second, our result demonstrates a smaller glacial-interglacial tempera-  
 531 ture change than previously estimated elsewhere in East Antarctica. This smaller glacial-  
 532 interglacial change may resolve the discrepancy between temperature estimates from cli-  
 533 mate models and ice-core data that has been noted in the literature for more than three  
 534 decades (Crowley and North, 1991). Our results thus lend greater confidence to the fi-  
 535 delity of climate-model simulations of last glacial maximum climate.

## 536 Acknowledgments

537 This work was funded through grants from the US National Science Foundation (E.J.S.  
 538 (1143105 and 1141839), C.B. (1643394 and 1443472), M.R.K. and others (1443471)). We  
 539 thank J.P. Severinghaus for providing  $^{15}\text{N}$  data collected under grant NSF1443710. The  
 540 SPC14 high-resolution water stable isotope record published with this paper can be ac-  
 541 cessed through the USAP Data Center (DOI: 10.15784/601239). The radar data used  
 542 in the ice-flow modeling can be accessed through the USAP Data Center at  
 543 <https://www.usap-dc.org/view/project/p0000200>. We thank G.H. Roe, B.R. Markle, and  
 544 D. Shapero for suggestions on this work, and M. Twickler and J. Souney for their work  
 545 administering the SPICEcore project. We thank the SPICEcore field team, the 109th  
 546 New York Air National Guard, and the National Science Foundation Ice Core Facility,  
 547 for the collection, transport, processing, and storage of the core.

## 548 References

549 Argus, D.F., Peltier, W.R., Drummond, R. and Moore, A.W. (2014) The Antarctica  
 550 component of postglacial rebound model ICE-6G C (VM5a) based upon GPS po-  
 551 sitioning, exposure age dating of ice thicknesses, and relative sea level histories.  
 552 *Geophys. J. Int.*, 198(1), 537-563, doi:10.1093/gji/ggu140.

- 553 Bailey, A., Singh, H.K.A., and J. Nusbaumer. (2019). Evaluating a Moist Isentropic  
554 Framework for Poleward Moisture Transport: Implications for Water Isotopes  
555 Over Antarctica. *Geophysical Research Letters*, 46(13), 7819–7827.
- 556 Barkan, E and Luz, B. (2007). Diffusivity fractionations of  $\text{H}_2^{16}\text{O}/\text{H}_2^{17}\text{O}$  and  
557  $\text{H}_2^{16}\text{O}/\text{H}_2^{18}\text{O}$  in air and their implications for isotope hydrology. *Rapid Commu-*  
558 *nications in Mass Spectrometry*, 21(18), 2999-3005.
- 559 Bazin, L., Landais, A., Lemieux-Dudon, B., Toyé Mahamadou Kele, H., Veres, D.,  
560 Parrenin, F., Martinerie, P., Ritz, C., Capron, E., Lipenkov, V., Loutre, M.-F.,  
561 Raynaud, D., Vinther, B., Svensson, A., Rasmussen, S. O., Severi, M., Blunier, T.,  
562 Leuenberger, M., Fischer, H., Masson-Delmotte, V., Chappellaz, J., and Wolff, E.  
563 (2013). An optimized multi-proxy, multi-site Antarctic ice and gas orbital chronol-  
564 ogy (AICC2012): 120800 ka. *Climate of the Past*, 9, 1715-1731.
- 565 Bintanja, R., and van de Wal, R. S. W. (2008). North American ice-sheet dynamics  
566 and the onset of 100,000-year glacial cycles. *Nature*, 454(7206), 869.
- 567 Blunier, T., and Schwander, J. (2000). Gas enclosure in ice: age difference and frac-  
568 tionation. *Physics of Ice Core Records* 307–326. Hokkaido University Press.
- 569 Bréant, C., Martinerie, P., Orsi, A., Arnaud, L., and Landais, A. (2017). Modelling  
570 firn thickness evolution during the last deglaciation: constraints on sensitivity to  
571 temperature and impurities. *Climate of the Past*, 13, 833-853.
- 572 Briggs, R.D. , Pollard, T., and Tarasov, L. (2014). A data-constrained large ense-  
573 mble analysis of Antarctic evolution since the Eemian. *Quaternary Science Reviews*,  
574 Volume 103, 1 November 2014, 91–115, doi:10.1016/j.quascirev.2014.09.003
- 575 Buizert, C., Martinerie, P., Petrenko, V. V., Severinghaus, J. P., Trudinger, C. M.,  
576 Witrant, E., Steele, L. P. et al. (2012). Gas transport in firn: multiple-tracer  
577 characterisation and model intercomparison for NEEM, Northern Greenland.  
578 *Atmospheric Chemistry and Physics*, 12(9), 4259–4277.
- 579 Buizert, C., Sowers, T., and Blunier, T. (2013). Assessment of diffusive isotopic frac-  
580 tionation in polar firn, and application to ice core trace gas records. *Earth and*  
581 *Planetary Science Letters*, 361, 110–119.
- 582 Buizert, C., Gkinis, V., Severinghaus, J. P., He, F., Lecavalier, B. S., Kindler, P.,  
583 Brook, E. J., et al. (2014). Greenland temperature response to climate forcing  
584 during the last deglaciation. *Science*, 345(6201), 1177–1180.
- 585 Buizert, C., Cuffey, K. M., Severinghaus, J. P., Baggenstos, D., Fudge, T. J.,  
586 Steig, E. J., Sowers, T. A. et al. (2015). The WAIS divide deep ice core WD2014  
587 chronologyPart 1: methane synchronization (6831 kaBP) and the gas ageice age  
588 difference. *Climate of the Past*, 11(2).
- 589 Casey, K. A., Fudge, T. J., Neumann, T. A., Steig, E. J., Cavitte, M. G. P., and  
590 Blankenship, D. D. (2014). The 1500 m South Pole ice core: Recovering a 40 ka  
591 environmental record. *Annals of Glaciology*, 55(68), 137–146.
- 592 Catania, G, C. Hulbe, and H. Conway, 2010. Grounding-line basal melt rates deter-  
593 mined using radar-derived internal stratigraphy, *J. Glaciol.* 56(197), 545-554.
- 594 Crowley, T. J., and G. R. North (1991). *Paleoclimatology*. New York, NY: Oxford  
595 University Press.
- 596 Cuffey, K. M., Clow, G. D., Alley, R. B., Stuiver, M., Waddington, E. D., and  
597 Saltus, R. W. (1995). Large arctic temperature change at the Wisconsin-Holocene  
598 glacial transition. *Science*, 270(5235), 455–458.
- 599 Cuffey, K. M. and Steig, E. J. (1998). Isotopic diffusion in polar firn: Implications  
600 for interpretation of seasonal climate parameters in ice-core records, with empha-  
601 sis on central Greenland. *Journal of Glaciology*, 44(147), 273–284.
- 602 Cuffey, K. M., Clow, G. D., Steig, E. J., Buizert, C., Fudge, T. J., Koutnik, M., Sev-  
603 eringhaus, J. P. et al. (2016). Deglacial temperature history of West Antarctica.  
604 *Proceedings of the National Academy of Sciences*, 113(50), 14249–14254.
- 605 Dahl-Jensen, D., Mosegaard, K., Gundestrup, N., Clow, G. D., Johnsen, S. J.,  
606 Hansen, A. W., and Balling, N. (1998). Past temperatures directly from the

- 607 Greenland ice sheet. *Science*, 282(5387), 268–271.
- 608 Dansgaard, W. (1964). Stable isotopes in precipitation. *Tellus B*, 16(4), 436–468.
- 609 Dansgaard, W., and Johnsen, S. J. (1969). A flow model and a time scale for the ice  
610 core from Camp Century, Greenland. *Journal of Glaciology*, 8(53), 215–223.
- 611 Epifanio, J. A., Brook, E. J., Buizert, C., Edwards, J. S., Sowers, T. A., Kahle,  
612 E. C., Severinghaus, J. P., Steig, E. J., Winski, D. A., Osterberg, E. C.,  
613 Fudge, T. J., Aydin, M., Hood, E., Kalk, M., Kreutz, K. J., Ferris, D. G., and  
614 Kennedy, J. A.: The SP19 chronology for the South Pole Ice Core - Part 2: gas  
615 chronology,  $\Delta$ age, and smoothing of atmospheric records, *Clim. Past Discuss.*,  
616 <https://doi.org/10.5194/cp-2020-71>, 2020.
- 617 EPICA Community Members. 2004. Eight glacial cycles from an Antarctic ice core.  
618 *Nature* 429, 623–628.
- 619 Fausto, R. S., Box, J. E., Vandecrux, B. R. M., van As, D., Steffen, K., MacFerrin,  
620 M. J., Charalampidis, C. et al. (2018). A snow density dataset for improving sur-  
621 face boundary conditions in Greenland ice sheet firn modeling. *Frontiers in Earth*  
622 *Science*, 6(51).
- 623 Forsberg, R., A.V. Olesen, F. Ferraccioli, T. Jordan, H. Corr and K. Mat-  
624 suoka (2017). PolarGap 2015/16: Filling the GOCE polar gap in Antarc-  
625 tica and ASIRAS flight around South Pole. Radar grids available at: *ftp* :  
626 [//ftp.bas.ac.uk/tomj/PolarGAP/PolarGAP\\_radar\\_grids.zip](ftp://ftp.bas.ac.uk/tomj/PolarGAP/PolarGAP_radar_grids.zip)
- 627 Freitag, J., Kipfstuhl, S., Laepple, T., and Wilhelms, F. (2013). Impurity-controlled  
628 densification: a new model for stratified polar firn. *Journal of Glaciology*, 59(218),  
629 1163–1169.
- 630 Fudge, T. J., Waddington, E. D., Conway, H., Lundin, J. M. D., and Taylor, K.  
631 (2014). Interpolation methods for Antarctic ice-core timescales: application to  
632 Byrd, Siple Dome and Law Dome ice cores. *Climate of the Past*, 10(3), 1195–1209.
- 633 Fudge, T. J., Markle, B. R., Cuffey, K. M., Buizert, C., Taylor, K. C., Steig, E.  
634 J., Koutnik, M. et al. (2016). Variable relationship between accumulation and  
635 temperature in West Antarctica for the past 31,000 years. *Geophysical Research*  
636 *Letters*, 43(8), 3795–3803.
- 637 Fudge, T. J., Lilien, D. A., Koutnik, M., Conway, H., Stevens, C. M., Wadding-  
638 ton, E. D., Steig, E. J., Schauer, A. J., and Holschuh, N. (2020). Advection and  
639 non-climate impacts on the South Pole Ice Core. *Clim. Past*, 16, 819832.
- 640 Gades, A.M., C.F. Raymond, H. Conway and R.W. Jacobel, 2000. Bed properties  
641 of Siple Dome and adjacent ice streams West Antarctica, inferred from radio-echo  
642 sounding measurements. *Journal of Glaciology*, 46(152), 88-94.
- 643 Gelman, A., Roberts, G. O., and Gilks, W. R. (1996). Efficient Metropolis jumping  
644 rules. *Bayesian Statistics*, 5(599-608), 42.
- 645 Gkinis, V., Simonsen, S. B., Buchardt, S. L., White, J. W. C. and Vinther, B. M.  
646 (2014). Water isotope diffusion rates from the NorthGRIP ice core for the last  
647 16,000 years - glaciological and paleoclimatic implications. *Earth and Planetary*  
648 *Science Letters*, 405, 132–141.
- 649 Gudmundsson, G. H., and Raymond, M. (2008). On the limit to resolution and in-  
650 formation on basal properties obtainable from surface data on ice streams. *The*  
651 *Cryosphere*, 2(3), 413–445.
- 652 Guillevic, M., Bazin, L., Landais, A., Kindler, P., Orsi, A., Masson-Delmotte, V.,  
653 Martinerie, P. et al. (2013). Spatial gradients of temperature, accumulation and  
654  $\delta^{18}\text{O}$ -ice in Greenland over a series of Dansgaard-Oeschger events. *Climate of*  
655 *the Past*, 9(3), 1029–1051.
- 656 Hammer, C. U., Clausen, H. B., Dansgaard, W., Gundestrup, N., Johnsen, S. J., and  
657 Reeh, N. (1978). Dating of Greenland ice cores by flow models, isotopes, volcanic  
658 debris, and continental dust. *Journal of Glaciology*, 20(82), 3–26.
- 659 Herron, M. M., and Langway, C. C. (1980). Firn densification: an empirical model.  
660 *Journal of Glaciology*, 25(93), 373–385.

- 661 Holme, C., Gkinis, V., and Vinther, B. M. (2018). Molecular diffusion of stable  
662 water isotopes in polar firn as a proxy for past temperatures. *Geochimica et Cos-*  
663 *mochimica Acta*, 225, 128-145.
- 664 Huber, C., Leuenberger, M., Spahni, R., Flückiger, J., Schwander, J., Stocker, T. F.,  
665 Jouzel, J. et al. (2006). Isotope calibrated Greenland temperature record over Ma-  
666 rine Isotope Stage 3 and its relation to CH<sub>4</sub>. *Earth and Planetary Science Letters*,  
667 243(3-4), 504–519.
- 668 Johnsen, S. J. (1977). Stable isotope homogenization of polar firn and ice. *Isotopes*  
669 *and Impurities in Snow and Ice*, 201–219.
- 670 Johnsen, S. J., Clausen, H. B., Cuffey, K. M., Hoffmann, G., Schwander, J. and  
671 Creyts, T. (2000). Diffusion of stable isotopes in polar firn and ice: The isotope  
672 effect in firn diffusion. *Physics of Ice Core Records*, 121–140.
- 673 Jones, T. R., Cuffey, K. M., White, J. W. C., Steig, E. J., Buizert, C., Markle,  
674 B. R., McConnell, J. R. and Sigl, M. (2017a). Water isotope diffusion in the WAIS  
675 Divide ice core during the Holocene and last glacial. *Journal of Geophysical Re-*  
676 *search: Earth Surface*, 122, 290-309.
- 677 Jones, T. R., White, J. W. C., Steig, E. J., Vaughn, B. H., Morris, V., Gkinis, V.,  
678 Markle, B. R. and Schoenemann, S. W. (2017b). Improved methodologies for  
679 continuous flow analysis of stable water isotopes in ice cores. *Atmospheric Mea-*  
680 *surement Techniques*, 10, 617-632.
- 681 Jordan, T. A., Martin, C., Ferraccioli, F., Matsuoka, K., Corr, H., Forsberg, R., Ole-  
682 sen, A., and Siegert, M. (2018). Anomalously high geothermal flux near the South  
683 Pole. *Scientific reports*, 8(1), 1-8.
- 684 Jouzel, J., Barkov, N. I., Barnola, J. M., Bender, M., Chappellaz, J., Genthon, C.,  
685 Raynaud, D. et al. (1993). Extending the Vostok ice-core record of palaeoclimate  
686 to the penultimate glacial period. *Nature*, 364(6436), 407.
- 687 Jouzel, J., Vimeux, F., Caillon, N., Delaygue, G., Hoffmann, G., MassonDelmotte,  
688 V., and Parrenin, F. (2003). Magnitude of isotope/temperature scaling for inter-  
689 pretation of central Antarctic ice cores. *Journal of Geophysical Research: Atmo-*  
690 *spheres*, 108(D12).
- 691 Jouzel, J., Masson-Delmotte, V., Cattani, O., Dreyfus, G., Falourd, S., Hoffmann,  
692 G., Fischer, H. et al. (2007). Orbital and millennial Antarctic climate variability  
693 over the past 800,000 years. *Science*, 317(5839), 793–796.
- 694 Kahle, E. C., Holme, C., Jones, T. R., Gkinis, V., and Steig, E. J. (2018). A Gen-  
695 eralized Approach to Estimating Diffusion Length of Stable Water Isotopes From  
696 IceCore Data. *Journal of Geophysical Research: Earth Surface*, 123(10), 2377–  
697 2391.
- 698 Kahle, E. C. (2020). Climate reconstructions from ice cores: New techniques to  
699 understand the information preserved in the South Pole ice core (Doctoral disser-  
700 tation, University of Washington, Seattle, USA).
- 701 Khan, A., Mosegaard, K., and Rasmussen, K. L. (2000). A new seismic velocity  
702 model for the Moon from a Monte Carlo inversion of the Apollo lunar seismic  
703 data. *Geophysical Research Letters*, 27(11), 1591–1594.
- 704 Kindler, P., Guillevic, M., Baumgartner, M. F., Schwander, J., Landais, A., and  
705 Leuenberger, M. (2014). Temperature reconstruction from 10 to 120 kyr b2k from  
706 the NGRIP ice core. *Climate of the Past*, 10(2), 887–902.
- 707 Koutnik, M. R., Fudge, T. J., Conway, H., Waddington, E. D., Neumann, T. A.,  
708 Cuffey, K. M., Taylor, K. C., et al. (2016). Holocene accumulation and ice flow  
709 near the West Antarctic Ice Sheet Divide ice core site. *Journal of Geophysical*  
710 *Research: Earth Surface*, 121(5), 907–924.
- 711 Lamb, K. D., Clouser, B. W., Bolot, M., Sarkozy, L., Ebert, V., Saathoff, H.,  
712 Mohler, O., and Moyer, E. J. (2017). Laboratory measurements of HDO/H<sub>2</sub>O  
713 isotopic fractionation during ice deposition in simulated cirrus clouds. *Proceedings*  
714 *of the National Academy of Sciences*, 114(22), 5612-5617.

- 715 Lazzara, M. A., Keller, L. M., Markle, T., and Gallagher, J. (2012). Fifty-year  
716 AmundsenScott South Pole station surface climatology. *Atmospheric Research*,  
717 118, 240–259.
- 718 Lilien, D. A., Fudge, T. J., Koutnik, M. R., Conway, H., Osterberg, E. C., Ferris, D.  
719 G., and Stevens, C. M. et al. (2018). Holocene IceFlow Speedup in the Vicinity of  
720 the South Pole. *Geophysical Research Letters*, 45(13), 6557–6565.
- 721 Looyenga, H. (1965). Dielectric constants of heterogeneous mixtures. *Physica*, 31(3),  
722 401–406.
- 723 Lorius, C., Jouzel, J., Raynaud, D., Hansen, J., and Le Treut, H. (1990). The ice-  
724 core record: climate sensitivity and future greenhouse warming. *Nature*, 347(6289),  
725 139.
- 726 Luz, B., and Barkan, E. (2010). Variations of 17O/16O and 18O/16O in meteoric  
727 waters. *Geochimica et Cosmochimica Acta*, 74(22), 6276–6286.
- 728 MacAyeal, D. R. (1993). Binge/purge oscillations of the Laurentide ice sheet as a  
729 cause of the North Atlantic’s Heinrich events. *Paleoceanography*, 8(6), 775–784.
- 730 Majoube, B. (1970). Fractionation factor of <sup>18</sup>O between water vapour and ice.  
731 *Nature* 226, 1242.
- 732 Markle, B. R. (2017). *Climate dynamics revealed in ice cores: advances in tech-  
733 niques, theory, and interpretation* (Thesis (PH. D.) – University of Washington,  
734 208 pp.).
- 735 Martinerie, P., Lipenkov, V. Y., Raynaud, D., Chappellaz, J., Barkov, N. I., and  
736 Lorius, C. (1994). Air content paleo record in the Vostok ice core (Antarctica):  
737 A mixed record of climatic and glaciological parameters. *Journal of Geophysical  
738 Research*, 99(D5), 10565.
- 739 Masson-Delmotte, V., Kageyama, M., Braconnot, P., Charbit, S., Krinner, G., Ritz,  
740 C., and Gladstone, R. M. et al. (2006). Past and future polar amplification of cli-  
741 mate change: climate model intercomparisons and ice-core constraints. *Climate  
742 Dynamics*, 26(5), 513–529.
- 743 Masson-Delmotte, V., Hou, S., Ekaykin, A., Jouzel, J., Aristarain, A., Bernardo, R.  
744 T., Frezzotti, M., et al. (2008). A review of Antarctic surface snow isotopic com-  
745 position: Observations, atmospheric circulation, and isotopic modeling. *Journal of  
746 Climate*, 21(13), 3359–3387.
- 747 Masson-Delmotte, V., M. Schulz, A. Abe-Ouchi, J. Beer, A. Ganopolski, J.F. Gon-  
748 zalez Rouco, E. Jansen, K. Lambeck, J. Luterbacher, T. Naish, T. Osborn, B.  
749 Otto-Bliesner, T. Quinn, R. Ramesh, M. Rojas, X. Shao and A. Timmermann  
750 (2013). Information from Paleoclimate Archives. In: *Climate Change 2013: The  
751 Physical Science Basis. Contribution of Working Group I to the Fifth Assessment  
752 Report of the Intergovernmental Panel on Climate Change* [Stocker, T.F., D.  
753 Qin, G.-K. Plattner, M. Tignor, S.K. Allen, J. Boschung, A. Nauels, Y. Xia, V.  
754 Bex and P.M. Midgley (eds.)]. *Cambridge University Press*, Cambridge, United  
755 Kingdom and New York, NY, USA.
- 756 Metropolis, N., Rosenbluth, A. W., Rosenbluth, M. N., Teller, A. H., and Teller, E.  
757 (1953). Equation of state calculations by fast computing machines. *The Journal of  
758 Chemical Physics*, 21(6), 1087–1092.
- 759 Monnin, E., Steig, E.J., Siegenthaler, U., Kawamura, K., Schwander, J., Stauffer, B.,  
760 Morse, D.L., Stocker, T.F., Barnola, J.M., Bellier, B., Raynaud, D. and Fischer,  
761 H. (2004). Evidence for substantial accumulation rate variability in Antarctica  
762 during the Holocene through synchronization of CO<sub>2</sub> in the Taylor Dome, Dome C  
763 and DML ice cores. *Earth and Planetary Science Letters* 224, 45–54.
- 764 Mosegaard, K., and Tarantola, A. (1995). Monte Carlo sampling of solutions to  
765 inverse problems. *Journal of Geophysical Research: Solid Earth*, 100(B7), 12431–  
766 12447.
- 767 Mosegaard, K. (1998). Resolution analysis of general inverse problems through in-  
768 verse Monte Carlo sampling. *Inverse Problems*, 14(3), 405.

- 769 Mosegaard, K., and Tarantola, A. (2002). Probabilistic approach to inverse prob-  
 770 lems. *International Geophysics Series*, 81(A), 237–268.
- 771 Mosegaard, K., and Sambridge, M. (2002). Monte Carlo analysis of inverse problems.  
 772 *Inverse problems*, 18(3), R29.
- 773 Neumann, T.A., H. Conway, S. Price, E.D. Waddington and D.L. Morse, 2008.  
 774 Holocene accumulation and ice-sheet dynamics in central West Antarctica. *J.*  
 775 *Geophys. Res.*, 113, (F2).
- 776 Nye, J. (1963). Correction factor for accumulation measured by the thickness of the  
 777 annual layers in an ice sheet. *Journal of Glaciology*, 4(36), 785–788.
- 778 Parrenin, F., F. Remy, C., Ritz, M.J. Siegert, and J. Jouzel. (2004). New modeling  
 779 of the Vostok ice flow line and implication of the glaciological chronology of the  
 780 Vostok ice core. *Journal of Geophysical Research*, 109, (D20).
- 781 Parrenin, F., Barker, S., Blunier, T., Chappellaz, J., Jouzel, J., Landais, A., Veres,  
 782 D. et al. (2012). On the gas-ice depth difference ( $\Delta$ depth) along the EPICA Dome  
 783 C ice core. *Climate of the Past*, 8(2), 1089–1131.
- 784 Parrenin, F., Masson-Delmotte, V., Kohler, P., Raynaud, D., Paillard, D., Schwander,  
 785 J., Jouzel, J., et al. (2013). Synchronous change of atmospheric CO<sub>2</sub> and  
 786 Antarctic temperature during the last deglacial warming. *Science*, 339(6123),  
 787 1060–1063.
- 788 Peltier, W.R. (2004). Global Glacial Isostasy and the Surface of the Ice-Age Earth:  
 789 The ICE-5G (VM2) Model and GRACE. *Ann. Rev. Earth and Planet. Sci.*, 32,  
 790 111–149.
- 791 Pollard, D., and DeConto, R. M. (2009). Modelling West Antarctic ice sheet growth  
 792 and collapse through the past five million years. *Nature*, 458(7236), 329–332.
- 793 Price, P.B., O.V. Nagornov, R. Bay, D. Chirkin, Y. He, P. Miocinovic, A. Richards,  
 794 K. Woschnagg, B. Koci and Victor Zagorodnov, 2002. Temperature Profile for  
 795 Glacial Ice at the South Pole: Implications for Life in a Nearby Subglacial Lake.  
 796 *Proceedings of the National Academy of Sciences*, 99(12), 7844–7847.
- 797 Raymond, C. (1983). Deformation in the vicinity of ice divides. *Journal of Glaciol-*  
 798 *ogy*, 29(103), 357–373.
- 799 Roy, K., and Peltier, W. R. (2015). Glacial isostatic adjustment, relative sea level  
 800 history and mantle viscosity: reconciling relative sea level model predictions for  
 801 the US East coast with geological constraints. *Geophysical Journal International*,  
 802 201(2), 1156–1181, doi:10.1093/gji/ggv066.
- 803 Severinghaus, J. P., Sowers, T., Brook, E. J., Alley, R. B., and Bender, M. L. (1998).  
 804 Timing of abrupt climate change at the end of the Younger Dryas interval from  
 805 thermally fractionated gases in polar ice. *Nature*, 391(6663), 141.
- 806 Severinghaus, J. P., Grachev, A., and Battle, M. (2001). Thermal fractionation of  
 807 air in polar firn by seasonal temperature gradients. *Geochemistry, Geophysics,*  
 808 *Geosystems*, 2(7).
- 809 Schoenemann, S. W., Steig, E. J., Ding, Q., Markle, B. R., and Schauer, A. J.  
 810 (2014). Triple waterisotope record from WAIS Divide, Antarctica: Controls  
 811 on glacialinterglacial changes in  $\delta^{18}O$  excess of precipitation. *Journal of Geophysical*  
 812 *Research: Atmospheres*, 119(14), 8741–8763.
- 813 Schwander, J., and Stauffer, B. (1984). Age difference between polar ice and the air  
 814 trapped in its bubbles. *Nature*, 311(5981), 45–47.
- 815 Schwander, J., Stauffer, B., and Sigg, A. (1988). Air mixing in firn and the age of  
 816 the air at pore close-off. *Annals of Glaciology*, 10, 141–145.
- 817 Schwander, J. The transformation of snow to ice and the occlusion of gases, in: H.  
 818 Oeschger, C.C. Langway Jr. (Eds.), *The Environmental Record in Glaciers and Ice*  
 819 *Sheets*, John Wiley, New York, 1989, pp. 53–67.
- 820 Sigl, M., Fudge, T. J., Winstrup, M., Cole-Dai, J., Ferris, D., McConnell, J. R., Bisi-  
 821 aux, M. et al. (2016). The WAIS Divide deep ice core WD2014 chronology Part 2:  
 822 Annual-layer counting (0–31 ka BP). *Climate of the Past*, 12(3), 769–786.

- 823 Simonsen, S. B., Johnsen, S. J., Popp, T. J., Vinther, B. M., Gkinis, V., and Steen-  
 824 Larsen, H. C. (2011). Past surface temperatures at the NorthGRIP drill site from  
 825 the difference in firn diffusion of water isotopes. *Climate of the Past*, 7(4), 1327.
- 826 Sowers, T., Bender, M., Raynaud, D., and Korotkevich, Y. S. (1992).  $\delta^{15}\text{N}$  of  $\text{N}_2$   
 827 in air trapped in polar ice: A tracer of gas transport in the firn and a possible  
 828 constraint on ice age differences. *Journal of Geophysical Research: Atmo-*  
 829 *spheres*, 97(D14), 15683–15697.
- 830 Steen-Larsen, H. C., Waddington, E. D., and Koutnik, M. R. (2010). Formulating an  
 831 inverse problem to infer the accumulation-rate pattern from deep internal layer-  
 832 ing in an ice sheet using a Monte Carlo approach. *Journal of Glaciology*, 56(196),  
 833 318–332.
- 834 Steig, E.J., Grootes, P.M., Stuiver, M. (1994). Seasonal precipitation timing and ice  
 835 core records. *Science*, 266, 1885–1886.
- 836 Steig, E. J., Ding, Q., White, J. W. C., Küttel, M., Rupper, S. B., Neumann, T. A.,  
 837 Neff, P. D., Gallant, A. J. E., Mayewski, P. A., Taylor, K. C., Hoffmann, G.,  
 838 Dixon, D. A., Schoenemann, S., Markle B. M., Schneider, D. P., Fudge, T. J.,  
 839 Schauer, A. J., Teel, R. P., Vaughn, B., Burgener, L., Williams, J. and Korotkikh,  
 840 E. (2013). Recent climate and ice-sheet change in West Antarctica compared to  
 841 the past 2000 years. *Nature Geoscience*, 6(5), 372.
- 842 Steig, E. J., Gkinis, V., Schauer, A. J., Schoenemann, S. W., Samek, K., Hoffnagle,  
 843 J., Tan, S. M. et al. (2014). Calibrated high-precision  $^{17}\text{O}$ -excess measurements  
 844 using cavity ring-down spectroscopy with laser-current-tuned cavity resonance.  
 845 *Atmos. Meas. Tech.*, 7, 2421–2435.
- 846 Stevens, C. M., Verjans, V., Lundin, J. M. D., Kahle, E. C., Horlings, A. N., Hor-  
 847 lings, B. I., and Waddington, E. D.: The Community Firn Model (CFM) v1.0,  
 848 Geosci. Model Dev. Discuss., <https://doi.org/10.5194/gmd-2019-361>, in review,  
 849 2020.
- 850 Tarantola, A. (1987). Inverse problem theory: Methods for data fitting and model  
 851 parameter estimation. *Elsevier*, Amsterdam.
- 852 van der Wel, G., Fischer, H., Oerter, H., Meyer, H., and Meijer, H. A. J. (2015).  
 853 Estimation and calibration of the water isotope differential diffusion length in ice  
 854 core records. *The Cryosphere*, 9(4), 1601–1616.
- 855 Veres, D., Bazin, L., Landais, A., Toyé Mahamadou Kele, H., Lemieux-Dudon,  
 856 B., Parrenin, F., Chappellaz, J. et al. (2013). The Antarctic ice core chronology  
 857 (AICC2012): an optimized multi-parameter and multi-site dating approach for the  
 858 last 120 thousand years. *Climate of the Past*, 9(4), 1733–1748.
- 859 Werner, M., Mikolajewicz, U., Heimann, M., Hoffmann, G. (2000). Borehole ver-  
 860 sus isotope temperatures on Greenland: Seasonality does matter. *Geophysical*  
 861 *Research Letters*, 27(5), 723–726.
- 862 Whillans, I. M., and Grootes P. M. (1985). Isotopic diffusion in cold snow and firn.  
 863 *Journal of Geophysical Research*, 90(D2), 3910–3918.
- 864 Winski, D. A., Fudge, T. J., Ferris, D. G., Osterberg, E. C., Fegyveresi, J. M., Cole-  
 865 Dai, J., Buizert, C., Epifanio, J., Brook, E.J., Beaudette, R., Severinghaus, J.,  
 866 Sowers, T., Steig, E.J., Kahle, E.C., Jones, T.R., Morris, V., Aydin, M., Nice-  
 867 wonger, M.R., Casey, K.A., Alley, R.B., Waddington, E.D., Iverson, N.A. (2019).  
 868 The SP19 chronology for the South Pole Ice CorePart 1: volcanic matching and  
 869 annual layer counting. *Climate of the Past*, 15(5), 1793–1808.

1 **Reconstruction of temperature, accumulation rate, and**  
2 **layer thinning from an ice core at South Pole, using a**  
3 **statistical inverse method**

4 **Emma C. Kahle<sup>1</sup>, Eric J. Steig<sup>1</sup>, Tyler R. Jones<sup>2</sup>, T.J. Fudge<sup>1</sup>, Michelle R.**  
5 **Koutnik<sup>1</sup>, Valerie A. Morris<sup>2</sup>, Bruce H. Vaughn<sup>2</sup>, Andrew J. Schauer<sup>1</sup>, C.**  
6 **Max Stevens<sup>1</sup>, Howard Conway<sup>1</sup>, Edwin D. Waddington<sup>1</sup>, Christo Buizert<sup>3</sup>,**  
7 **Jenna Epifanio<sup>3</sup>, James W. C. White<sup>2</sup>**

8 <sup>1</sup>Department of Earth and Space Sciences, University of Washington, Seattle WA 98195, USA

9 <sup>2</sup>Institute of Arctic and Alpine Research, University of Colorado, Boulder CO 80309, USA

10 <sup>3</sup>College of Earth Ocean and Atmospheric Sciences, Oregon State University, Corvallis OR 97331, USA

11 **Key Points:**

- 12 • An inverse method using a firn model with isotope diffusion provides self-consistent  
13 temperature, accumulation rate, and thinning histories.
- 14 • Glacial-interglacial temperature change at the South Pole was 6.7 +/- 1.0 K. The  
15 d18O/T sensitivity is 0.99 +/- 0.03 permille/K.
- 16 • Reconstruction of ice thinning shows millennial-scale variations in thinning func-  
17 tion and decreased thinning at depth compared to 1-D model.

---

Corresponding author: Emma C. Kahle, [eckahle@uw.edu](mailto:eckahle@uw.edu)

**Abstract**

Data from the South Pole ice core (SPC14) are used to constrain climate conditions and ice-flow-induced layer thinning for the last 54,000 years. Empirical constraints are obtained from the SPC14 ice and gas timescales, used to calculate annual-layer thickness and the gas-ice age difference ( $\Delta\text{age}$ ), and from high-resolution measurements of water isotopes, used to calculate the water-isotope diffusion length. Both  $\Delta\text{age}$  and diffusion length depend on firn properties and therefore contain information about past temperature and snow-accumulation rate. A statistical inverse approach is used to obtain an ensemble of reconstructions of temperature, accumulation-rate, and thinning of annual layers in the ice sheet at the SPC14 site. The traditional water-isotope/temperature relationship is not used as a constraint; the results therefore provide an independent calibration of that relationship. The temperature reconstruction yields a glacial-interglacial temperature change of  $6.7 \pm 1.0^\circ\text{C}$  at the South Pole. The sensitivity of  $\delta^{18}\text{O}$  to temperature is  $0.99 \pm 0.03\text{‰}^\circ\text{C}^{-1}$ , significantly greater than the spatial slope of  $0.8\text{‰}^\circ\text{C}^{-1}$  that has been used previously to determine temperature changes from East Antarctic ice core records. The reconstructions of accumulation rate and ice thinning show millennial-scale variations in the thinning function as well as decreased thinning at depth compared to the results of a 1-D ice flow model, suggesting influence of bedrock topography on ice flow.

**1 Introduction**

Ice cores from polar ice sheets provide important records of past changes in climate and ice dynamics. Temperature and snow-accumulation rate are critical targets for reconstruction from ice-core data (Lorius et al., 1990). The traditional approach to reconstructing temperature is the use of water isotope ratios ( $\delta^{18}\text{O}$ ,  $\delta\text{D}$ ), calibrated using empirical relationships (Dansgaard, 1964; Jouzel et al., 1993). Another approach is borehole thermometry, which provides a direct measurement of the modern temperature profile of the ice sheet that can be related to surface temperature history through a heat advection-diffusion model (Cuffey et al., 1995; Dahl-Jensen et al., 1998). Finally, measurements of  $\delta^{15}\text{N}$  of  $\text{N}_2$  in trapped air bubbles provide information about the thickness of the firn layer and past abrupt temperature changes that produce thermal gradients (Sowers et al., 1992; Schwander, 1989; Severinghaus et al., 1998). Because firn thickness is a function of accumulation rate and temperature,  $\delta^{15}\text{N}$  can be used to provide constraints on both variables through modeling of the firn densification process (Huber et al., 2006; Guillevic et al., 2013; Kindler et al., 2014). With independent constraints on the ice-core depth-age relationship, in particular from annual-layer counting, these approaches can be combined to produce robust estimates of temperature and accumulation rate through time. Results from Greenland (Buizert et al., 2014) and the West Antarctic Ice Sheet (WAIS) Divide ice core (Cuffey et al., 2016) provide recent examples.

In comparison with locations in West Antarctica and Greenland, ice-core sites in East Antarctica pose special challenges. The low accumulation rates typical of the East Antarctic plateau are less favorable for borehole thermometry; high accumulation rates and locations near ice divides, where horizontal velocities are low, are generally necessary for preservation of detectable thermal anomalies. Additionally, some recent studies have questioned the validity of firn models at the typically very cold temperatures during the glacial period in East Antarctica (Freitag et al., 2013; Bréant et al., 2017), since many of the models are calibrated with or designed for warmer conditions. One approach that may help to address such challenges is to use the “diffusion length,” a measure of the spectral properties of high-depth-resolution measurements of water-isotope ratios. Water-isotope diffusion length reflects the vertical diffusion experienced by water molecules through the firn column (Johnsen, 1977; Whillans and Grootes, 1985; Cuffey and Steig, 1998; Johnsen et al., 2000). While diffusion length has primarily been used as a proxy for temperature (e.g., Simonsen et al., 2011; Gkinis et al., 2014; van der Wel et al., 2015; Holme et al.,

2018; Gkinis et al., 2021), it is sensitive to both temperature and accumulation rate through their influence on the firn density profile and tortuosity, and is also affected by vertical strain (Gkinis et al., 2014; Jones et al., 2017a). Diffusion length thus provides an independent constraint on several important ice-core properties: temperature, accumulation rate, and the thinning history due to ice deformation.

Here, we present data from a new ice core (SPC14) from the South Pole, East Antarctica, and we use a novel approach to combine multiple data sets to constrain temperature, accumulation-rate, and ice-thinning histories. We take advantage of two timescales for SPC14, one for the ice (Winski et al., 2019) and one for the gas enclosed within it (Epifanio et al., 2020), to obtain an empirical measure of the gas-age ice-age difference ( $\Delta\text{age}$ ). We also use high-resolution measurements of  $\delta^{17}\text{O}$ ,  $\delta^{18}\text{O}$ , and  $\delta\text{D}$  of ice (Steig et al., 2021) to obtain water-isotope diffusion lengths.

We use a statistical inverse approach to obtain optimized, self-consistent reconstructions of temperature and accumulation rate using a combined firn-densification and water-isotope diffusion model. We exclude gas isotope ( $\delta^{15}\text{N}$ ) data and use the water-isotope values only for calculating diffusion length, reserving these variables for comparison and validation. This approach allows us to produce a novel and independent calibration of the traditional isotope paleothermometer without the use of borehole thermometry. We also obtain an independent constraint on the thinning of annual layers. This is important at South Pole because the location of the site is about 200 km from the ice divide and the ice-flow history is not well known at ages earlier than the Holocene (Lilien et al., 2018).

## 2 Data from the South Pole Ice Core

The South Pole Ice Core (SPC14) was obtained from 2014 to 2016 at 89.9889°S, 98.1596°W, approximately 2 km from the geographic South Pole. SPC14 was drilled to a depth of 1751 m, equivalent to an age of approximately 54 ka (Winski et al., 2019). Compared to other East Antarctic plateau ice-core sites, South Pole has a relatively high annual accumulation rate (8 cm w.e.  $\text{a}^{-1}$ ) (Casey et al., 2014) given its low mean-annual air temperature of  $-49^\circ\text{C}$  (Lazzara et al., 2012). The mean firn temperature is  $-51^\circ\text{C}$  (Severinghaus et al., 2001). The modern surface ice velocity is  $10 \text{ m a}^{-1}$  (Casey et al., 2014).

The data sets used in our analysis are developed from the independent ice and gas timescales for SPC14 described previously by Winski et al. (2019) and Epifanio et al. (2020), respectively, and water-isotope measurements obtained at high depth resolution by continuous-flow analysis, as described in Steig et al. (2021). We briefly summarize the information obtained directly from the ice-core measurements as well as the data sets derived from that information (annual-layer thickness,  $\Delta\text{age}$ , and water-isotope diffusion length).

### 2.1 Ice Timescale and Annual-Layer Thickness

The SP19 ice timescale was constructed by stratigraphic matching of 251 volcanic tie points between SPC14 and WAIS Divide (Winski et al., 2019). Between tie points, identification of individual layers from seasonal cycles in sodium and magnesium ions was used to produce an annually-resolved timescale for most of the Holocene. For ages greater than 11.3 ka, despite lack of annual resolution, the uncertainty of the timescale is estimated to be within 124 years relative to WD2014 (Winski et al., 2019). Annual-layer thickness is given by the depth between successive years on the SP19 timescale. For ages older than 11.3 ka where annual layers could not be identified, Winski et al. (2019) found the smoothest annual-layer thickness which matched 95% of the volcanic tie points to within one year. Based on the uncertainty associated with interpolation between sparse tie points (Fudge et al., 2014), we estimate the uncertainty in annual-layer thickness (two standard deviations, hereafter s.d.) to be  $\pm 3\%$  of the value in the Holocene, increasing to  $\pm 10\%$  of the value at earlier ages.

## 2.2 Gas Timescale and $\Delta_{\text{age}}$

Epifanio et al. (2020) developed the SPC14 gas timescale through stratigraphic matching of features in the high-resolution  $\text{CH}_4$  records of the SPC14 and WAIS Divide cores. The difference in age between the ice and gas timescales,  $\Delta_{\text{age}}$ , is a measure of the ice age at the lock-in depth, which depends on the rate of firn densification (Schwander and Stauffer, 1984; Schwander et al., 1988; Blunier and Schwander, 2000). Epifanio et al. (2020) determined  $\Delta_{\text{age}}$  empirically at each of the  $\text{CH}_4$  tie points and used a cubic spline fit to derive a continuous  $\Delta_{\text{age}}$  curve for all depths. Due to the empirical nature of the gas timescale, the SPC14  $\Delta_{\text{age}}$  record is determined without the use of a firn-densification model. Moreover, the SPC14  $\Delta_{\text{age}}$  was obtained without relying on the additional constraint of  $\delta^{15}\text{N}$  to determine lock-in depth.

We assign an age to each empirical  $\Delta_{\text{age}}$  estimate as the mid-point between the gas-age and ice-age timescales from which  $\Delta_{\text{age}}$  is calculated. This approximation is justified by results from a dynamic densification model (Stevens et al., 2020), which show that at a site like South Pole the timescale on which  $\Delta_{\text{age}}$  responds to climate variations is a time interval shorter than  $\Delta_{\text{age}}$  itself. Uncertainty in  $\Delta_{\text{age}}$  depends on uncertainty in the match between the WAIS Divide and SPC14 gas timescales, the uncertainty associated with interpolation between tie points, and uncertainty in the  $\Delta_{\text{age}}$  for WAIS Divide. Because  $\Delta_{\text{age}}$  is an order of magnitude smaller at WAIS Divide than at South Pole, that source of uncertainty is the smallest. The uncertainty estimated by Epifanio et al. (2020) ranges from  $\pm 1\%$  to  $\pm 8\%$  (two s.d.) of the value of  $\Delta_{\text{age}}$ .

## 2.3 Water-Isotope Measurements and Diffusion Length

We measured water-isotope ratios at an effective resolution of 0.5 cm using continuous flow analysis (CFA), following the methods described in Jones et al. (2017b) and Steig et al. (2021). We measured  $\delta^{18}\text{O}$  and  $\delta\text{D}$  for the entirety of the core and  $\delta^{17}\text{O}$  from a depth of 556 m through the bottom of the core. We used Picarro Inc. cavity ring-down laser spectroscopy (CRDS) instruments, including both a model L2130-i (for  $\delta^{18}\text{O}$  and  $\delta\text{D}$ ) and a model L2140-i for  $\delta^{17}\text{O}$  (Steig et al., 2014). We use the standard notation for  $\delta^{18}\text{O}$ :

$$\delta^{18}\text{O}_{\text{sample}} = \left( \frac{^{18}\text{O}}{^{16}\text{O}} \right)_{\text{sample}} / \left( \frac{^{18}\text{O}}{^{16}\text{O}} \right)_{\text{VSMOW}} - 1,$$

where VSMOW is Vienna Standard Mean Ocean Water.  $\delta^{17}\text{O}$  and  $\delta\text{D}$  are defined similarly. These measurements were used to calculate the water-isotope diffusion length. Figure 1 shows the  $\delta^{18}\text{O}$  measurements at 100-year-mean resolution as a function of age.

After deposition as snow on the ice-sheet surface, water isotopologues diffuse through interconnected air pathways among ice grains in the firn, driven by isotope-concentration gradients in the vapor phase (Johnsen, 1977; Whillans and Grootes, 1985; Cuffey and Steig, 1998). In solid ice below the firn column, diffusion continues, but at a rate orders of magnitude slower than in the firn (Johnsen et al., 2000). The extent of diffusion is quantified as the diffusion length, the mean cumulative diffusive-displacement in the vertical direction of water molecules relative to their original location in the firn.

Diffusion length is determined from spectral analysis of the high-resolution water-isotope data, following the methods described in Kahle et al. (2018). We use discrete data sections of 250 years. We calculate the diffusion length,  $\sigma$ , for each section by fitting its power spectrum with a model of a diffused power spectrum and a two-component model of the measurement system noise:

$$P = P_0 \exp(-k^2 \sigma^2) + P'_0 \exp(-k^2 (\sigma')^2) + |\hat{\eta}|^2, \quad (1)$$

where  $k$  is the wavenumber,  $|\hat{\eta}|^2$  is the measurement noise, and  $P_0$ ,  $P'_0$ , and  $\sigma'$  are variable fitting parameters. The second term ( $P'_0 \exp(-k^2 (\sigma')^2)$ ) accounts for the influence

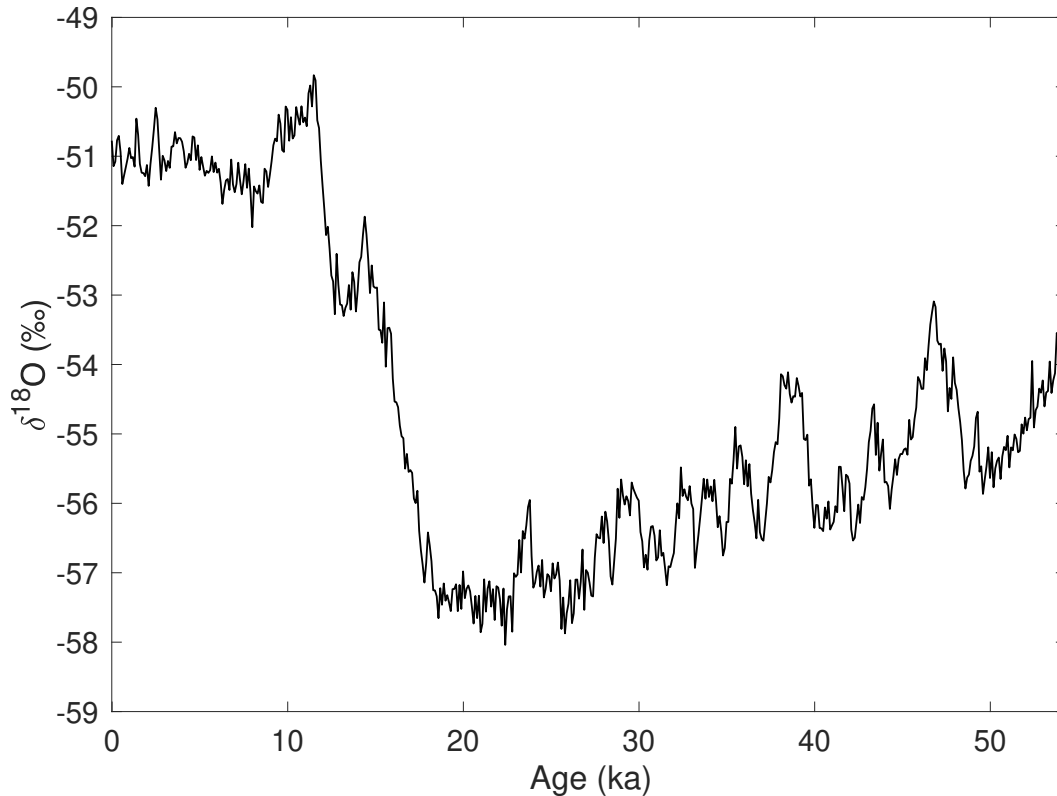


Figure 1: High-resolution  $\delta^{18}\text{O}$  record (Steig et al., 2021) from the South Pole ice core (SPC14), shown as discrete 100-year averages for clarity, on the SP19 ice timescale (Winski et al., 2019).

165 of the CFA measurement system on the water-isotope data spectrum. Kahle et al. (2018)  
 166 found that this term does not completely eliminate the effect of system smoothing on  
 167 the spectrum; we therefore make an additional correction, based on the sequential mea-  
 168 surement of ice standards of known and differing isotopic composition, following Jones  
 169 et al. (2017b). This correction is small, accounting for only  $\sim 4\%$  of the total diffusion  
 170 length throughout the core. The uncertainty on  $\sigma$  is estimated conservatively as described  
 171 in Kahle et al. (2018) and varies from  $\pm 4\%$  to  $\pm 66\%$  (two s.d.) of the value throughout  
 172 the core.

173 Additionally, we correct the diffusion-length estimates to account for diffusion in the solid  
 174 ice, following Gkinis et al. (2014). This effect is also small, accounting for a maximum  
 175 of 4% of the total diffusion length at the bottom of the core. To calculate the solid-ice  
 176 diffusion length, we assume the modern borehole temperature profile  $T(z)$  remains con-  
 177 stant through time to find the diffusivity profile  $D_{ice}(z)$ , following Gkinis et al. (2014).  
 178 We use borehole temperature measurements from the nearby neutrino observatory (Price  
 179 et al., 2002). We assume a simple thinning function from a 1-D ice-flow model (Dans-  
 180 gaard and Johnsen, 1969) with a kink-height  $h_0 = 0.2$  for this calculation; the error in  
 181 this assumption is negligible for the small deviations in total thinning we are calculat-  
 182 ing. We subtract both the solid-ice and CFA diffusion lengths from the observations in  
 183 quadrature to produce our final diffusion-length data set. Further details on both cor-  
 184 rections are provided in the Supporting Information, Section S1.1.

185 We calculate the diffusion length for each of the three water-isotope ratios measured on  
 186 the core. To combine the information from each isotope, we convert  $\delta^{17}\text{O}$  and  $\delta\text{D}$  dif-  
 187 fusion lengths to equivalent values for  $\delta^{18}\text{O}$ . For example, the  $\delta^{18}\text{O}$ -equivalent diffusion  
 188 length ( $\sigma_{18 \text{ from } 17}$ ) from the  $\delta^{17}\text{O}$  diffusion length ( $\sigma_{17}$ ) is:

$$\sigma_{18 \text{ from } 17}^2 = \sigma_{17}^2 \frac{D_{18}}{\alpha_{18}} \bigg/ \frac{D_{17}}{\alpha_{17}}, \quad (2)$$

189 where  $D$  and  $\alpha$  are the corresponding air diffusivity and solid-vapor fractionation fac-  
 190 tor for each isotope. Values for  $D$  and  $\alpha$  are given in the Supporting Information, Sec-  
 191 tion S1.2 (Majoube, 1970; Barkan and Luz, 2007; Luz and Barkan, 2010; Lamb et al.,  
 192 2017). For the single diffusion-length record used in our analysis, we take the mean of  
 193 these three estimates for  $\sigma_{18}$ .

### 194 3 Forward Model

195 We use a forward model to relate the observational data sets to the variables of inter-  
 196 est. Figure 2 summarizes the data sets obtained from the ice-core measurements and the  
 197 calculations described above:  $\Delta\text{age}$ , water-isotope diffusion length, and annual-layer thick-  
 198 ness. We use these three data sets as our ‘‘observations’’ in a statistical inverse approach  
 199 to infer temperature, accumulation rate, and ice-thinning function.

200 Figure 3 illustrates the structure of the forward model, including a firn-densification com-  
 201 ponent, a water-isotope diffusion component, and a vertical strain (ice thinning) com-  
 202 ponent. We describe the individual components below.

#### 203 3.1 Firn Densification

204 The firn layer comprises the upper few tens of meters of the ice sheet where snow is pro-  
 205 gressively densifying into solid ice. As successive layers of snow fall on the surface of the  
 206 ice sheet, the increase in overburden pressure causes the underlying ice crystals to pack  
 207 closer together. The firn matrix densifies through this packing and through metamor-  
 208 phism of the crystal fabric. The rate of densification is determined primarily by temper-  
 209 ature and accumulation rate. The Herron and Langway (1980) (HL) firn-densification  
 210 model is a benchmark empirical model, based on depth-density data from Greenland and  
 211 Antarctic ice cores (Lundin et al., 2017). We model the depth-density profile of the firn  
 212 using the HL framework due to its simplicity and its good match with measurements of  
 213 the modern South Pole firn density. We also evaluate the impact that using different firn  
 214 models would have on our results (Section 5.1).

215 We use a surface density  $\rho_0 = 350 \text{ kg m}^{-3}$ , consistent with measured values at the SPC14  
 216 site, and assume it remains constant through time (Fausto et al., 2018). We assess the  
 217 sensitivity of our results to this assumption in Section 5.1. The bottom of the firn is con-  
 218 strained by a close-off density  $\rho_{co}$ , which we define as a function of temperature (Mar-  
 219 tinerie et al., 1994). As temperature varies between  $-50$  and  $-60^\circ\text{C}$ , close-off density varies  
 220 in a small range between  $831.5$  and  $836.4 \text{ kg m}^{-3}$ .

221 We use the analytical formulation of the HL model, which assumes an isothermal firn.  
 222 If either temperature or accumulation rate changes on short timescales, a transient for-  
 223 mulation of the model would be required to reflect propagation through the firn column.  
 224 Although our temperature and accumulation-rate inputs vary through time, the timescale  
 225 of those variations (*i.e.*, 10 ka for  $\sim 6^\circ\text{C}$  change in temperature) is large enough that the  
 226 steady-state approximation is acceptable. To test this assumption, we ran our forward  
 227 model with a transient formulation of the HL model (Stevens et al., 2020) and found no  
 228 difference in the results when we account for the advection time through the firn, as we  
 229 do in our inverse approach. Since the transient model is more computationally expen-  
 230 sive, we use the analytical formulation.

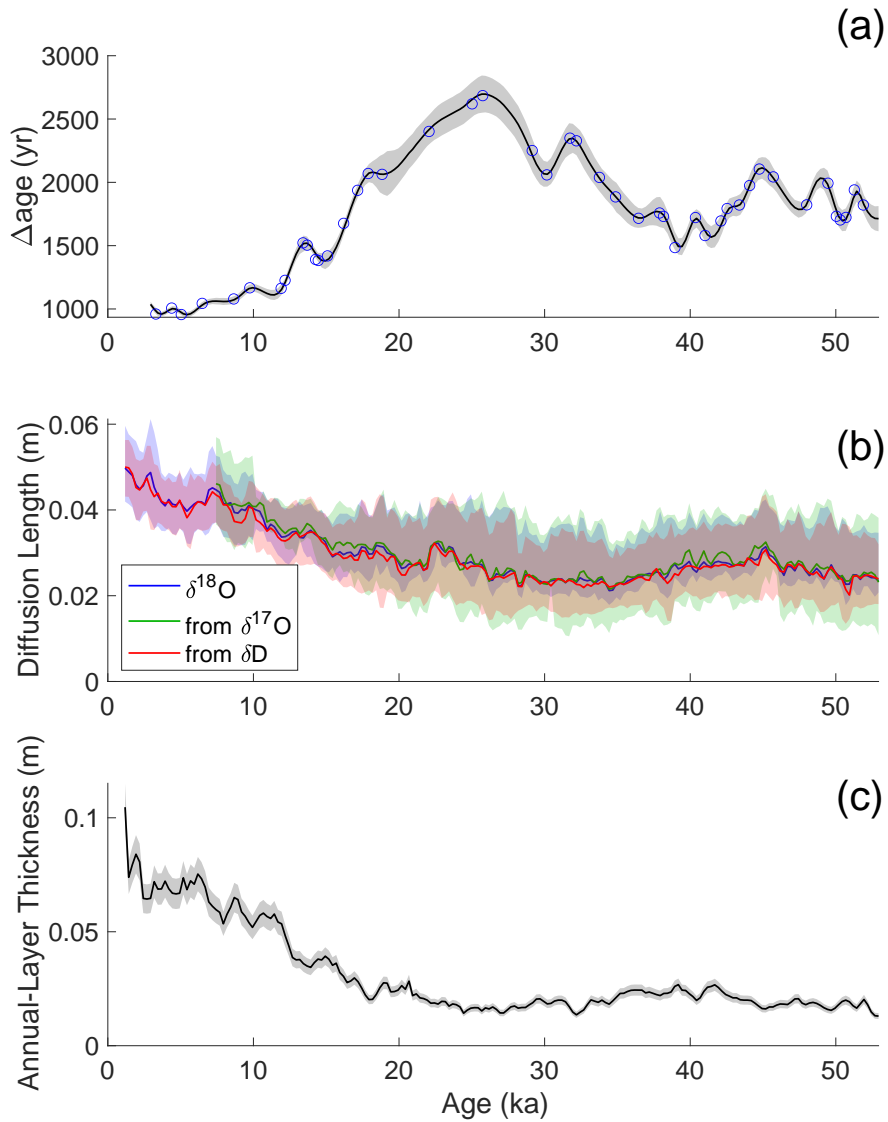


Figure 2: Data sets from SPC14 used to optimize the inverse problem, each averaged over bins of 250 years and plotted with uncertainty representing two s.d. Panel (a) shows  $\Delta\text{age}$  with tie points marked in blue circles, panel (b) shows water-isotope diffusion lengths, and panel (c) shows annual-layer thickness data. Diffusion lengths from  $\delta^{17}\text{O}$  (green) and  $\delta\text{D}$  (red) have been converted to  $\delta^{18}\text{O}$ -equivalent values.

### 231 3.2 Modeling $\Delta\text{age}$

232 Modeled  $\Delta\text{age}$  is given by the difference in the modeled age of the ice and the gas at the  
 233 lock-in depth. We define the lock-in depth at a density of  $10 \text{ kg m}^{-3}$  less than the close-

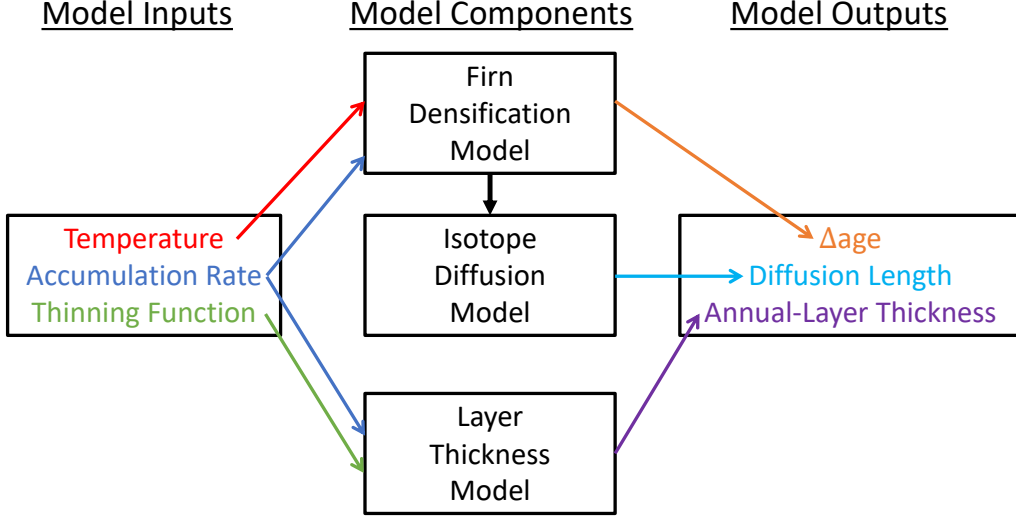


Figure 3: Illustration of the forward model components, which include firn densification (Section 3.1/3.2), water-isotope diffusion (Section 3.3), and a model of layer thickness (Section 3.4). Together, these components relate the variables of interest (temperature, accumulation rate, and thinning function) to the observational data sets ( $\Delta$ age, layer thickness, and diffusion length) shown in Figure 2.

234 off density (Blunier and Schwander, 2000). The age of the ice at this depth is estimated  
 235 directly from the age-density profile from the firn-densification model. We estimate the  
 236 age of the gas at the lock-in depth (LID) using the parameterization in Buizert et al. (2013):

$$\text{gas age}(\rho_{\text{LID}}) = \frac{1}{1.367} \left( 0.934 \times \frac{(\text{DCH})^2}{D_{\text{CO}_2}^0} + 4.05 \right), \quad (3)$$

237 where DCH is the diffusive column height given in units of m, defined as the lock-in depth  
 238 minus a 3 m convective zone at the surface where firn air is well-mixed with the atmo-  
 239 sphere.  $D_{\text{CO}_2}^0$  is the free air diffusivity of  $\text{CO}_2$  defined in Schwander et al. (1988) and  
 240 Buizert et al. (2012) and given in units of  $\text{m}^2 \text{a}^{-1}$ . The lock-in depth is defined as the  
 241 depth at which the effective molecular diffusivity of the gas is reduced to one thousandth  
 242 of the free air diffusivity (Buizert et al., 2013).

### 243 3.3 Modeling Diffusion Length

The combined effects on the initial isotope profile ( $\delta = \delta(z, 0)$ ) due to diffusion and firn densification are given by:

$$\frac{\partial \delta}{\partial t} = D \frac{\partial^2 \delta}{\partial z^2} - \epsilon z \frac{\partial \delta}{\partial z}, \quad (4)$$

244 where  $\delta(z', t)$  is the resulting smoothed and compressed isotope profile after time  $t$  since  
 245 deposition,  $D$  is the diffusivity coefficient,  $\epsilon$  is the vertical strain rate, and  $z$  is the ver-  
 246 tical coordinate assuming an origin fixed on an arbitrary sinking layer of firn (Johnsen,  
 247 1977; Johnsen et al., 2000; Whillans and Grootes, 1985). Note that  $z'$  accounts for the  
 248 vertical compression of the original profile (Johnsen et al., 2000). Equation 4 is valid where  
 249 the isotopic exchange between firn grains and the surrounding vapor is rapid, where the  
 250 firn grains are well mixed and in isotopic equilibrium with the vapor, and where  $\delta \ll$   
 251 1000‰.

252 The diffusivity coefficient  $D_x$  of each isotope  $x$  depends on the temperature and density  
 253 profile of the firn column Whillans and Grootes (1985); Johnsen et al. (2000):

$$D_x = \frac{m p D_x^{air}}{RT \alpha_x \tau} \left( \frac{1}{\rho} - \frac{1}{\rho_{ice}} \right), \quad (5)$$

254 where  $m$  is the molar weight of water,  $p$  is the saturation pressure of water vapor over  
 255 ice at temperature  $T$  and with gas constant  $R$ ,  $D_x^{air}$  is the diffusivity of each isotopo-  
 256 logue through air,  $\alpha_x$  is the fractionation factor for each isotopic ratio in water vapor  
 257 over ice,  $\tau$  is the tortuosity of the firn,  $\rho$  is the firn density, and  $\rho_{ice}$  is the density of ice.  
 258 Values for these parameters are given in the Supporting Information, Section S1.2.

259 Using the output from the firn-densification model, we calculate water-isotope diffusion  
 260 through the depth-density profile. First, the density profile is used to calculate the dif-  
 261 fusivity of each isotope based on Equation 5. We then solve for the diffusion length  $\sigma_{firn}$   
 262 of a particular isotope ratio in terms of its effective diffusivity coefficient  $D$  and the firn  
 263 density  $\rho$  (Gkinis et al., 2014):

$$\sigma_{firn}^2(\rho) = \frac{1}{\rho^2} \int_{\rho_0}^{\rho} 2\rho^2 \left( \frac{d\rho}{dt} \right)^{-1} D(\rho) d\rho, \quad (6)$$

264 where  $\rho_0$  is the surface density and  $\frac{d\rho}{dt}$  is the material derivative of the density. To cal-  
 265 culate the diffusivity  $D$ , we use an atmospheric pressure of 0.7 atm, the ambient pres-  
 266 sure at the SPC14 site (Severinghaus et al., 2001), which we assume to be constant through  
 267 time.

268 Cumulative vertical strain significantly thins layers in the ice. The thinning function is  
 269 defined as the fractional amount of thinning that has occurred at a given depth in the  
 270 ice sheet. We account for the effects of vertical strain on our modeled firn diffusion length,  
 271  $\sigma_{firn}$ , using a thinning function  $\Gamma$ . We model the diffusion length measured in the ice  
 272 core as  $\sigma_{icecore}$ :

$$\sigma_{icecore} = \sigma_{firn} \times \Gamma. \quad (7)$$

273 Recall that when we compare the modeled diffusion length with the observations, the  
 274 observations have been corrected for diffusion in solid ice.

### 275 3.4 Modeling Annual-Layer Thickness

276 Annual-layer thickness  $\lambda$  is given by the accumulation rate  $\dot{b}$ , in ice-equivalent  $\text{m a}^{-1}$ ,  
 277 multiplied by the thinning function  $\Gamma$ :

$$\lambda = \dot{b} \times \Gamma. \quad (8)$$

## 278 4 Inverse Framework and Results

### 279 4.1 Initialization

280 We use a Bayesian statistical approach to produce an ensemble of possible solutions to  
 281 our inverse problem. Through many iterations, we use the forward model described above  
 282 to solve our forward problem and determine the range of possible model inputs. This  
 283 forward problem is described by the following equation, where the forward model,  $G$ , cal-  
 284 culates the modeled observables, or data parameters,  $d$  as a function of unknown input  
 285 variables, or model parameters,  $m$ :

$$G(m) = d. \quad (9)$$

286 Our forward model  $G$  is nonlinear and cannot be solved analytically. Instead, we use a  
 287 Monte Carlo approach to solve the inverse problem by testing many instances of  $m$  through

the forward model  $G$  to find the output  $d$  that best matches the observations  $d_{obs}$ . The theory and practical implementation of this approach are detailed in the Supporting Information, Section S2 (Tarantola, 1987; Mosegaard and Tarantola, 1995; Gelman et al., 1996; Mosegaard, 1998; Khan et al., 2000; Mosegaard and Sambridge, 2002; Mosegaard and Tarantola, 2002; Steen-Larsen et al., 2010).

We incorporate *a priori* information about model parameters based on their modern values and our best estimate of how they have varied through time. We include this *a priori* information by creating bounds on the allowable model space to explore and use the Metropolis algorithm to randomly create perturbations that sample within the bounded model space (Metropolis et al., 1953). If the algorithm proposes a solution  $m_x$  that falls outside of our bounded model space,  $m_x$  is disregarded and another solution is evaluated. Because we expect the parameters to vary smoothly through time, proposed perturbations are smoothed with a lowpass filter to prevent spurious high-frequency noise from being introduced. Temperature and accumulation-rate perturbations are smoothed with a lowpass filter with a cutoff period of 3000 years, which corresponds to the maximum value of  $\Delta$ age and thus the limit of natural smoothing we expect from the ice-core data. We expect the thinning function to be even smoother and apply a lowpass filter with a cutoff period of 10,000 years to those perturbations.

We also determine initial guesses  $m_1$  for each parameter. Initializing the problem at what is judged to be a reasonable solution  $m_1$  helps to avoid non-physical solutions (MacAyeal, 1993; Gudmundsson and Raymond, 2008). We design initial guesses for each parameter that are simplified versions of our best initial guess, allowing higher-frequency information to be inferred from the optimization. The initial guess of temperature is a step-function version of the water-isotope record. The initial guess for the thinning function is the output of a Dansgaard and Johnsen (1969) (DJ) ice-flow model. This simple model produces an approximation of the dynamics acceptable at many ice-core sites (Hammer et al., 1978). We use a kink height of  $h_0 = 0.2$  to simulate the flank flow at the SPC14 site. To produce an initial guess for accumulation rate, we divide the layer-thickness data by this thinning function and approximate the result with a simplified step function.

Each parameter is bounded based on naïve expectations for its variability. For temperature, we bound the model space with an upper and lower scaling of the step-function initial guess version of the water-isotope record. We create an envelope based on previous estimates of glacial-interglacial temperature change in Antarctica, which allows for solutions with glacial-interglacial changes as small as  $0.5^\circ\text{C}$  and as large as  $15^\circ\text{C}$ . For accumulation rate, the bounded model-parameter range is an envelope about our initial guess defined as  $\pm 0.02 \text{ m a}^{-1}$ . Given the surface and Holocene accumulation-rate fluctuations at South Pole described in Lilien et al. (2018), this range is a reasonable limit on accumulation rate, while still allowing variation in the values tested in each  $m$ . For the ice-equivalent thinning function, we enforce a value of one at the surface but do not provide further constraints on the model space because it is effectively constrained by the bounds on accumulation rate and layer thickness.

## 4.2 *A posteriori* Distributions

The resulting solutions  $m$  from our inverse approach are described by the *a posteriori* distribution. To visualize the high-dimensional *a posteriori* distribution, we plot probability distributions for each parameter. Rather than create separate probability distributions for each of the many parameters in our model space, we plot each probability distribution successively in a single figure to visualize the entire model space at once. Figure 4 shows our results, with the model inputs on the left and outputs on the right. The grey shading shows successive probability distributions. A vertical slice through the shading in each plot represents the probability distribution for a particular parameter (recall that a parameter represents the value of a variable at a specified model timestep, *e.g.*, the value of temperature at the 4th timestep). How often a particular value is ac-

340 cepted for each parameter is represented by the shading, where darker shading denotes  
 341 values that were accepted more often. The solid magenta curves describe the initial guess  
 342 for each parameter, and the dashed magenta curves describe the bounded model space  
 343 (for temperature and accumulation rate). The right three panels of Figure 4 illustrate  
 344 how well the modeled observables  $d(m)$  match with the observations  $d_{obs}$  throughout the  
 345 collection of solutions.

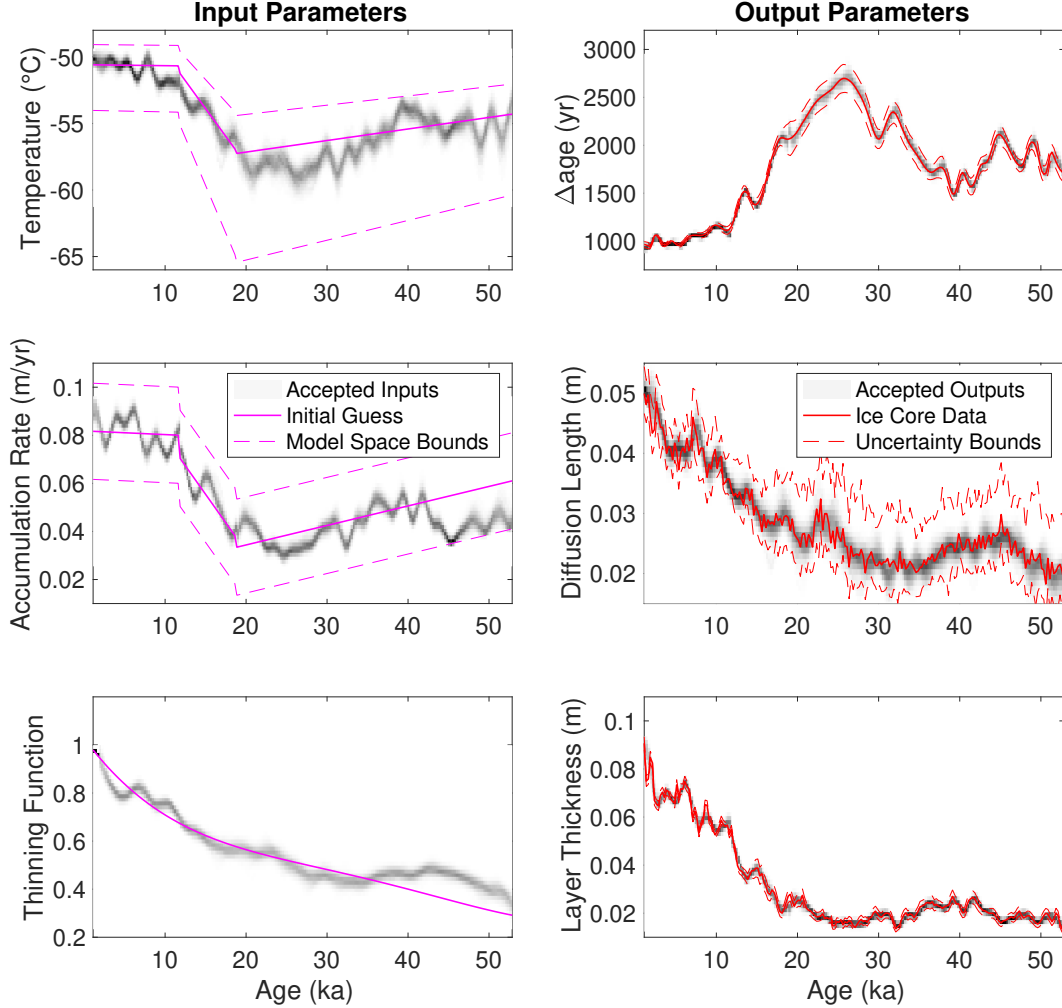


Figure 4: Results of the Monte Carlo inverse calculations, showing the *a posteriori* distribution result compared with *a priori* information. The grey shading in each panel represents probability distributions for each parameter from the *a posteriori* distribution, where darker shading signifies greater likelihood. Left panels show the initial guesses (solid magenta) and model bounds (dashed) for the input parameters: temperature, accumulation rate, and thinning. Right panels show the observational data (solid red) and prescribed uncertainties (dashed) for the output parameters:  $\Delta$ age, diffusion length, and layer thickness.

## 346 5 Sensitivity of Results

347 We evaluate the sensitivity of our results to choices within the forward model and in-  
 348 verse algorithm, as well as to constraints from the data sets included in the inverse prob-  
 349 lem and from independent data.

### 5.1 Sensitivity to Forward Model

350 Within the forward model, we hold the surface density  $\rho_0$  in the firn-densification model  
 351 constant through time. We tested two alternate values of surface density  $\rho_0$  ( $450 \text{ kg m}^{-3}$   
 352 and  $550 \text{ kg m}^{-3}$ ); we find no significant change in the results. We also did two exper-  
 353 iments to assess the impact of the choice of firn-densification model. First, we evaluated  
 354 the depth-density and age-density profiles using a large collection of models (Herron and  
 355 Langway, 1980; Goujon et al., 2003; Ligtenberg et al., 2011; Simonsen et al., 2013; Li and  
 356 Zwally, 2015) within the Community Firn Model framework (Stevens et al., 2020). Sec-  
 357 ond, we implemented two of those models, those of Goujon et al. (2003) (GOU) and Ligten-  
 358 berg et al. (2011) (LIG), within our inverse framework. The results are similar regard-  
 359 less of which firn model is used, but the GOU and LIG models produce consistently lower  
 360 temperatures than the HL model. Because this difference is systematic throughout the  
 361 depth of the core, the magnitude of reconstructed temperature variability, including the  
 362 glacial-interglacial temperature change, is not significantly affected (Figures S3 and S4).  
 363 Our choice of the HL model within our forward model is justified by the good agreement  
 364 with modern temperature compared with these other models and the consistency within  
 365 the interpretation of the temperature result across all models. Details from these sensi-  
 366 tivity tests are given in the Supporting Information, Section S3.1. It has been suggested  
 367 that most firn models (including the HL model) are biased to produce firn columns that  
 368 are too thick at very cold temperatures (Landais et al., 2006; Dreyfus et al., 2010; Fre-  
 369 itag et al., 2013; Bréant et al., 2017), though the magnitude of this bias is disputed. An  
 370 implicit assumption in our method is that the HL model is unbiased. We discuss the im-  
 371 plications of this assumption in Section 6.  
 372

### 5.2 Sensitivity to Inverse Algorithm

373 Within the formulation of the inverse algorithm, we evaluated the sensitivity to differ-  
 374 ent initial guesses for each parameter. Altering the initial guesses within the model space  
 375 bounds do not affect the final results. Additionally, including higher-frequency *a priori*  
 376 information in our initial guesses does not change the results. For example, we evalu-  
 377 ated initial guesses of constant values for each of temperature, accumulation rate, and  
 378 thinning function. These extremely simplified initial guesses produce results indistinguish-  
 379 able from those that include the high-frequency variability of each comparison data set,  
 380 but require many more iterations to reach an equilibrium solution. As recommended in  
 381 Gudmundsson and Raymond (2008), we opted for a middle-ground approach that saves  
 382 time by setting the initial guess close to the expected answer but relies on the optimiza-  
 383 tion to obtain high-frequency information.  
 384

### 5.3 Sensitivity to Included Data Constraints

385 We also examined the sensitivity of the results to each data set individually, as detailed  
 386 in the Supporting Information, Section S3.2. One key conclusion from these tests is that  
 387 all three data sets ( $\Delta$ age, layer thickness, and diffusion length) provide important infor-  
 388 mation for producing a well-constrained result (Figures S6 and S7), although the rela-  
 389 tive importance of each parameter varies with age in the record. In general, we find that  
 390 the diffusion length and layer thickness are sufficient to constrain accumulation rate, and  
 391 the  $\Delta$ age strongly impacts the temperature. However, while it is evident that  $\Delta$ age is  
 392 the most important constraint on temperature for ages less than  $\sim 35$  ka, at greater ages,  
 393 constraints provided by the combination of diffusion length and layer thickness become  
 394 increasingly critical.  
 395

396 We also considered the influence of the temperature-dependence of water-isotope diffu-  
 397 sivity. We evaluated the effect of removing the temperature-dependence (Equation 5),  
 398 so that diffusion-length data affects only the thinning function (Equation 7), and tem-  
 399 perature is primarily driven by the  $\Delta$ age data. The results show a significant difference  
 400 from the main result, demonstrating that the diffusion-length data provide an impor-  
 401 tant constraint on temperature, which has subsequent impact on other parameters. Fur-  
 402 ther details are provided in the Supporting Information, Section S3.2.

#### 5.4 Comparison with $\delta^{15}\text{N}$ data

Finally, we consider the impact on our results of the inclusion of information from measurements of  $\delta^{15}\text{N}$  in  $\text{N}_2$  of air bubbles in SPC14 (Winski et al., 2019; Severinghaus et al., 2019). The enrichment of  $\delta^{15}\text{N}$  in an ice core is a linear function of the original diffusive column height (DCH) of the firn, resulting from gravitational fractionation (Sowers et al., 1992; Buizert et al., 2013). We calculate DCH from  $\delta^{15}\text{N}$  as described in the Supporting Information (Equation S19). As shown in Figure S9, there are significant differences between the DCH calculated from the main reconstruction and that calculated from  $\delta^{15}\text{N}$ . We do not incorporate  $\delta^{15}\text{N}$  data in our full Monte-Carlo inverse procedure because this added constraint over-determines the solution; as we show in the following sensitivity test, no combinations of temperature and accumulation rate can simultaneously satisfy  $\delta^{15}\text{N}$  and the other data constraints at all depths in the core. Instead, we evaluate the impact of the additional constraint of  $\delta^{15}\text{N}$  data as follows.

We use the  $\delta^{15}\text{N}$  data to determine temperature and accumulation-rate pairs that produce a DCH in agreement with the  $\delta^{15}\text{N}$ -based DCH. To determine these pairs, we run a global search algorithm over a set of temperature and accumulation-rate values defined by a small range centered on the mean values from the main reconstruction (Figure 4). For each depth in the core, we use the HL firn model to calculate the DCH for all temperature and accumulation-rate values in the global search, and then select only the temperature and accumulation-rate pairs that produce a DCH within the uncertainty of the DCH calculated from  $\delta^{15}\text{N}$ . The result is shown in light-red shading in Figure 5. Compared with our main reconstruction, the accumulation-rate history remains essentially unchanged, but the mean temperature is greater by  $2.8^\circ\text{C}$  on average for the glacial period (*i.e.*, before about 15 ka). To further refine this suite of solutions, we select the subset of accumulation-rate and temperature values that both satisfy the  $\delta^{15}\text{N}$  constraint on DCH and are consistent (through the HL model) with  $\Delta\text{age}$ , within the uncertainty of the empirical  $\Delta\text{age}$  data. The blue shading in Figure 5 shows this combination of both  $\delta^{15}\text{N}$  and  $\Delta\text{age}$  constraints; the result is a decrease in mean values for both accumulation rate and temperature during the glacial period compared to  $\delta^{15}\text{N}$  alone. Areas of overlap (dark purple shading) between our main reconstruction and the combined  $\delta^{15}\text{N}$  and  $\Delta\text{age}$  constraints show where all constraints – diffusion length, layer thickness,  $\Delta\text{age}$ ,  $\delta^{15}\text{N}$  – are satisfied. Further details on this sensitivity test are given in the Supporting Information, Section S3.3 and Figure S9.

Three important conclusions can be drawn from these comparisons. First, while our temperature and accumulation-rate reconstructions are entirely consistent with  $\delta^{15}\text{N}$  constraints during the Holocene, a combination of warmer temperatures and lower accumulation rates are required to match the  $\delta^{15}\text{N}$  constraint in the glacial period. Second, there is no consistent solution for which all constraints (layer thickness, diffusion length,  $\Delta\text{age}$ , and  $\delta^{15}\text{N}$ ), for all depths in SPC14, are satisfied, implying that further refinements to firn models may be required (Supporting Information, Section S3.3). However, for those depths where all constraints are satisfied, the resulting temperatures are warmer by  $<1^\circ\text{C}$  on average than in our main reconstruction. This means that, third, our results are conservative with respect to the assumption that the HL model produces the correct DCH at very cold temperatures. This also supports the exclusion of  $\delta^{15}\text{N}$  in our main reconstruction, to avoid giving too much weight to the reproduction of the DCH by the HL model. For this reason, we focus on the results from our main reconstruction in the discussion which follows.

## 6 Discussion

We now consider our main reconstructions for accumulation rate, ice thinning, and temperature in comparison with estimates from simpler calculations and independent data. In general, the results are in agreement with naïve expectations, but with some important differences. Because the accumulation-rate and thinning reconstructions are fun-

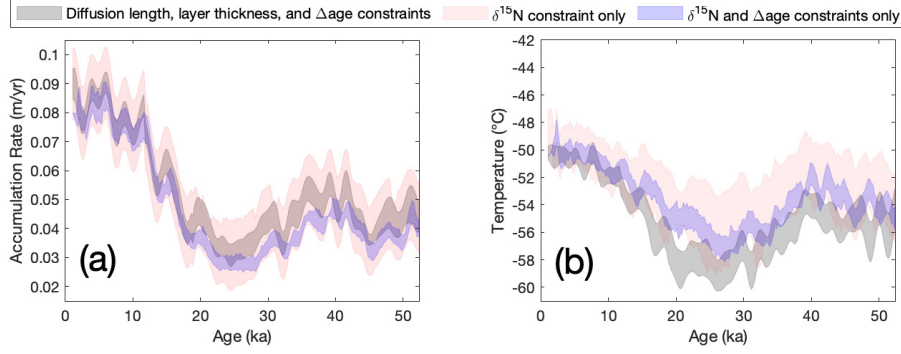


Figure 5: Results from a sensitivity test that includes  $\delta^{15}\text{N}$  as a constraint on diffusive column height (DCH). Panel (a) shows accumulation rate, and panel (b) shows temperature; shading represents 2 s.d. uncertainty for all three reconstructions. The main reconstruction is shown in grey. Results consistent with the  $\delta^{15}\text{N}$  constraints (only) are shown in red. Results consistent with both  $\delta^{15}\text{N}$  and the empirical  $\Delta\text{age}$  data are shown in blue. The overlap of blue and grey shows where all empirical constraints (layer thickness, diffusion length,  $\Delta\text{age}$ , and  $\delta^{15}\text{N}$ ) are satisfied within the framework of the firm model. Further details are given in the Supporting Information, Section S3.3 and Figure S9.

455 fundamentally linked through Equation 8, we discuss them together. We then compare our  
 456 reconstruction for temperature with the traditional water-isotope paleothermometer, and  
 457 discuss the broader implications of our results. The *a posteriori* distribution is near-Gaussian,  
 458 and in this section we plot its mean and standard deviation rather than the full prob-  
 459 ability distributions. Recall that the *a posteriori* distribution comprises only accepted  
 460 solutions, a subset of all iterations.

### 461 6.1 Accumulation Rate and Thinning Function

462 Figure 6 shows the results for the thinning function (panel (a)) and accumulation rate  
 463 (panel (b)). The grey shading denotes a band of two s.d. of the *a posteriori* distribu-  
 464 tion. In general, thinning functions are expected to be smooth and to decrease mono-  
 465 tonically because they integrate the total thinning experienced at a given depth, as il-  
 466 lustrated by the results of a 1-D Dansgaard-Johnsen (DJ) model with  $h_0 = 0.2$  (red curve,  
 467 panel (a)). However, the SPC14 site is far from an ice divide such that variations in the  
 468 bed topography upstream can create more complex thinning histories (e.g., Parrenin et al.,  
 469 2004). Thus, the thinning function result is similar to the DJ-model output, but con-  
 470 tains additional higher-frequency variations. To evaluate the plausibility of these vari-  
 471 ations in the primary reconstruction, we compare with two other independent estimates  
 472 of the thinning function, an ice-flow-model thinning function and a  $\delta^{15}\text{N}$ -based thinning  
 473 function.

474 First, we compare the primary thinning function with one calculated from an ice-flow  
 475 model. We use a 2.5-D flowband model (Koutnik et al., 2016) forced with observations  
 476 of the bedrock topography and the accumulation-rate pattern. Details of the model setup  
 477 are given in the Supporting Information, Section S4 (Nye, 1963; Looyenga, 1965; Gades  
 478 et al., 2000; Neumann et al., 2008; Catania et al., 2010; Jordan et al., 2018). The result-  
 479 ing thinning function is best considered in two segments. The thinning function for the  
 480 past 10 ka (solid black line in Figure 6) is well constrained because the flowline is known  
 481 (Lilien et al., 2018) and the bed topography has been measured along the flowline (Fig-  
 482 ure S11). The key result is that the bed undulations along the flowline cause the same  
 483 structure as is inferred in the primary thinning function. The “reversal” in the thinning  
 484 function at 7 ka, where deeper layers have thinned less than shallower layers, matches

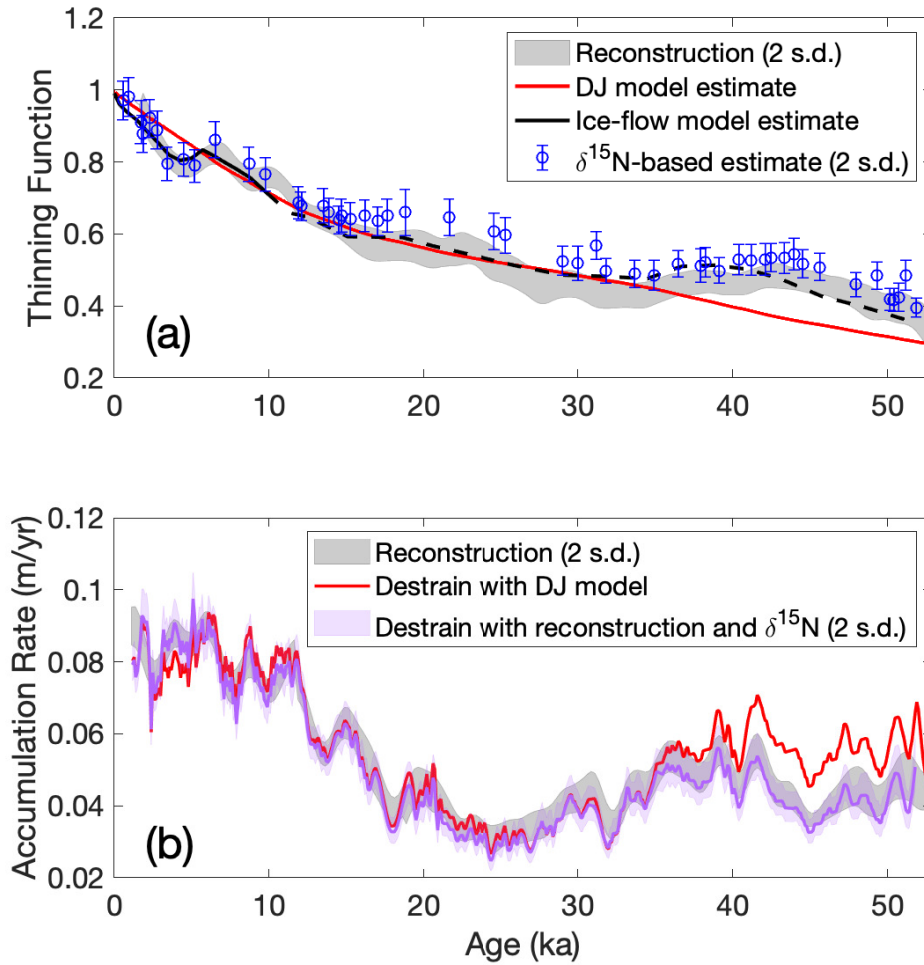


Figure 6: Reconstructions of accumulation rate and thinning function for SPC14. Two s.d. (grey shading) of the *a posteriori* distribution is plotted for each reconstruction alongside comparison estimates. Panel (a) shows the primary thinning function reconstruction (grey) compared to a DJ-model output with  $h_0 = 0.2$  (red), an ice-flow-model thinning function from a 2.5-D flowband model (solid and dashed black), and a  $\delta^{15}\text{N}$ -based thinning function with error bars showing two s.d. uncertainty (blue). The solid black curve shows where the ice-flow-model thinning function is well constrained by data, and the dashed black curve shows where the bed topography is simulated. The thinning function is shown vs. depth in the Supporting Information (Figure S10). Panel (b) shows the accumulation-rate reconstruction compared to two versions of the destriained layer-thickness data. The thinning functions used for destriaining are the DJ-model output (red) and the mean of the reconstruction and the  $\delta^{15}\text{N}$ -based estimate (purple).

485 well in both the primary and ice-flow-model thinning functions. This feature is caused  
 486 by an overdeepening in the bed topography (Figure S18).

487 For ages older than 10 ka, we do not know where the ice originated and thus cannot use  
 488 the ice-flow model to determine the thinning function with confidence. Instead, we aim  
 489 to evaluate whether the primary thinning function is physically plausible, given what we

490 know about the bed topography in the region. Using airborne radar measurements (Fors-  
 491 berg et al., 2017) to create a plausible bed beyond 100 km upstream, we show that the  
 492 ice-flow model (black dashed line) can approximately match the magnitude and struc-  
 493 ture of the primary thinning function. Therefore, the primary thinning function is con-  
 494 sistent with expectations, given plausible variations in bedrock topography.

495 Second, we compare the primary thinning function with a  $\delta^{15}\text{N}$ -based thinning function  
 496 (blue circles; error bars show two s.d. uncertainty). We obtain this estimate following  
 497 the methods described in Parrenin et al. (2012), who showed that the thinning function  
 498 scales with the ratio of “ $\Delta\text{depth}$ ” to the DCH, where  $\Delta\text{depth}$  is given by  $\Delta\text{age}$  multi-  
 499 plied by the depth/age slope from the ice-core timescale. The thinning function  $\Gamma$  is then  
 500 given by (Parrenin et al., 2012):

$$\Gamma = \frac{\Delta\text{depth}}{A \times \text{LID}}, \quad (10)$$

501 where  $A$  is a scaling factor that accounts for the ice-equivalent thickness of the original  
 502 firn column (Winski et al., 2019), and the lock-in depth,  $\text{LID} = \text{DCH} + 3$ , accounting  
 503 for a 3-m convective zone. We use our temperature reconstruction to incorporate the im-  
 504 pact of thermal fractionation in our calculation of the LID (Grachev and Severinghaus,  
 505 2003; Cuffey and Paterson, 2010; Fudge et al., 2019). Full details on this approach and  
 506 its uncertainties are given in the Supporting Information, Section S5.

507 Figure 6a shows that the structure of the  $\delta^{15}\text{N}$ -based thinning function generally agrees  
 508 with the primary reconstruction, showing the same high-frequency variations and mean  
 509 estimates whose error bars in general overlap with the uncertainty of the primary recon-  
 510 struction. There is the least agreement between ages of about 15 and 30 ka, where the  
 511  $\delta^{15}\text{N}$ -based thinning function is shifted appreciably towards higher values (less thinning).  
 512 This is consistent with the observation that the modeled DCH from our main reconstruc-  
 513 tion tends to be higher than that calculated from  $\delta^{15}\text{N}$ . We note that the uncertainties  
 514 for the  $\Delta\text{depth}$  calculation are not depth-independent; many known sources of error are  
 515 expected to be systematic. For example, if the WAIS Divide  $\Delta\text{age}$  data set were system-  
 516 atically too large during the glacial period, correcting for this would result in smaller es-  
 517 timates for the SPC14  $\Delta\text{depth}$ , and therefore smaller values (more thinning) in the  $\delta^{15}\text{N}$ -  
 518 based thinning function. The same adjustment to  $\Delta\text{age}$  results in no significant change  
 519 in the primary thinning function, thus improving the agreement between the means of  
 520 the two independent estimates. We discuss further quantification of uncertainties in these  
 521 calculations in Section 5.4 and Section S5.1 in the Supporting Information.

522 For comparison with the accumulation-rate reconstruction, Figure 6b shows two versions  
 523 of high-frequency estimates produced by destraining the layer-thickness data with es-  
 524 timates of the thinning function. The red curve uses the 1-D Dansgaard-Johnsen thin-  
 525 ning function; the resulting accumulation-rate estimate deviates from the reconstruction  
 526 at the oldest ages. Thus, the reconstruction reflects a significantly smaller accumulation  
 527 rate before 40 ka than would be inferred using a DJ model. The purple curve shows our  
 528 best estimate for high-frequency accumulation rate by combining the information from  
 529 both the primary thinning function and the  $\delta^{15}\text{N}$ -based thinning function; we use the  
 530 mean of these two thinning functions to destrain the layer-thickness data. We incorpo-  
 531 rate information from both thinning functions in order to include all available informa-  
 532 tion in our best estimate. The uncertainty is estimated by combining the uncertainties  
 533 of both thinning functions.

## 534 6.2 Temperature Reconstruction

535 The temperature reconstruction is shown in Figure 7. For comparison, we show two scaled  
 536 versions of the measured  $\delta^{18}\text{O}$ , corrected for secular variations in the  $\delta^{18}\text{O}$  of sea-water,  
 537 following Bintanja and van de Wal (2008). Recall that while we used diffusion length de-  
 538 termined from the  $\delta^{18}\text{O}$  power spectrum in our reconstruction, we do not use the abso-

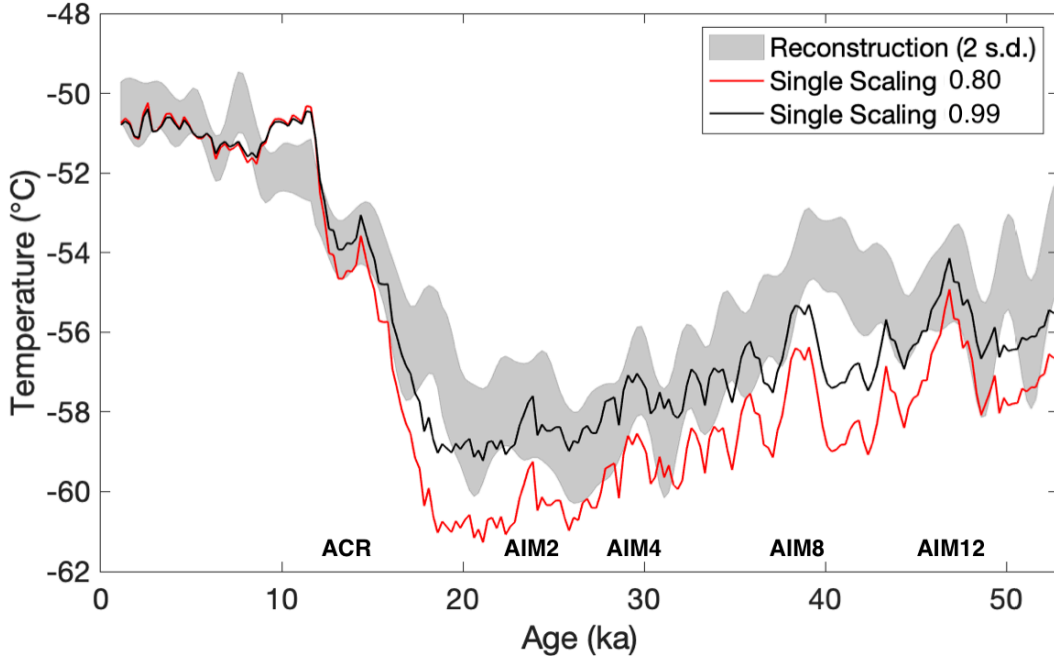


Figure 7: Reconstruction of temperature and relationship with  $\delta^{18}\text{O}$ . Grey shading shows two s.d. of the *a posteriori* distribution. Solid lines show scaled versions of  $\delta^{18}\text{O}$ , discretely averaged to 250-year resolution. The  $\delta^{18}\text{O}$  is scaled by  $0.8\text{‰}^{\circ}\text{C}^{-1}$  (red), the modern surface relationship, and by  $0.99\text{‰}^{\circ}\text{C}^{-1}$  (black), the calibrated linear relationship with the mean of the temperature reconstruction.

539 lute  $\delta^{18}\text{O}$  values; hence, these comparisons serve as an independent calibration of the tra-  
 540 ditional water-isotope thermometer, similar to what has been done previously with bore-  
 541 hole thermometry (Cuffey et al., 1995, 2016) but maintaining higher-frequency informa-  
 542 tion. The red curve in Figure 7 uses a scaling of  $\partial(\delta^{18}\text{O})/\partial T = 0.8\text{‰}^{\circ}\text{C}^{-1}$ , which is both  
 543 the observed modern surface isotope-temperature relationship at the site (Fudge et al.,  
 544 2020) and the value commonly used in the literature for Antarctica (e.g., Jouzel et al.,  
 545 2003), for which Masson-Delmotte et al. (2008) report a 1 s.d. error of  $0.01\text{‰}^{\circ}\text{C}^{-1}$ . The  
 546 black curve shows the best-fit linear calibration between  $\delta^{18}\text{O}$  and the mean of our re-  
 547 construction; this has a significantly greater slope of  $0.99\pm 0.03\text{‰}^{\circ}\text{C}^{-1}$  (2 s.d.). Our es-  
 548 timate of uncertainty on the slope accounts for errors in both variables, following the method  
 549 of York et al. (2004), with errors on temperature given by the *a posteriori* distribution  
 550 (Figure 7) and errors on  $\delta^{18}\text{O}$  ( $0.1\text{‰}$ , 1 s.d.) obtained from replicate continuous-flow mea-  
 551 surements made on the South Pole ice core as reported in Steig et al. (2021). Results  
 552 from the sensitivity tests (Section 5) using other firm models, and using independent  $\delta^{15}\text{N}$   
 553 constraints, yield the same result: slopes vary from 0.97 to greater than  $1.2\text{‰}^{\circ}\text{C}^{-1}$ . Cor-  
 554 relation with the  $\delta^{18}\text{O}$  is greatest ( $r=0.94$ ) with our main reconstruction (see Support-  
 555 ing Information, Section S3.4).

556 There are interesting similarities and differences between the calibrated  $\delta^{18}\text{O}$  and our  
 557 independent temperature reconstruction. For example, the prominent Antarctic Isotope

558 Maximum 12 (AIM12) event, at about 47 ka, is similar in both our reconstruction and  
 559 the scaled  $\delta^{18}\text{O}$  data, and suggests a temperature change of about  $2^\circ\text{C}$ . On the other hand,  
 560 our temperature reconstruction for AIM8, at about 38 ka, is part of a low-frequency vari-  
 561 ation longer than that indicated by the  $\delta^{18}\text{O}$  data, and the mean reconstruction suggests  
 562 that AIM8 was warmer than AIM12, while a simple linear scaling of the  $\delta^{18}\text{O}$  implies  
 563 the opposite. Another interesting feature is AIM2 ( $\sim 24$  ka), which is muted in most East  
 564 Antarctic records, but is prominent in the WAIS Divide ice core (WAIS Divide Project  
 565 Members, 2013). AIM2 is clearly evident in both our reconstruction and in the scaled  
 566  $\delta^{18}\text{O}$  data, as is AIM4 ( $\sim 30$  ka) and the Antarctic Cold Reversal (ACR) ( $\sim 13$  ka).

567 In contrast, the early-Holocene isotope maximum (centered at about 10 ka) is muted in  
 568 our temperature reconstruction. This is perhaps surprising, given the prevalence of this  
 569 feature in the  $\delta^{18}\text{O}$  records, both at South Pole and elsewhere in East Antarctica. On  
 570 the other hand, there is no early-Holocene peak in the WAIS Divide record, in either the  
 571  $\delta^{18}\text{O}$  or the borehole-calibrated temperature reconstruction (WAIS Divide Project Mem-  
 572 bers, 2013; Cuffey et al., 2016). Furthermore, the temperature reconstruction suggests  
 573 an earlier onset of deglacial warming (at about 22 ka) than the isotope data suggest, but  
 574 similar to both the isotope data and the temperature reconstruction at WAIS Divide (WAIS  
 575 Divide Project Members, 2013; Cuffey et al., 2016). Because large changes in the  $\delta^{18}\text{O}$ -  
 576 temperature relationship can occur, for example, from changes in seasonality (Steig et al.,  
 577 1994; Werner et al., 2000), we cannot assume that either result (*i.e.*, our main recon-  
 578 struction or the scaled  $\delta^{18}\text{O}$ ) is the more faithful representation of temperature. Rec-  
 579 onciling the differences would benefit from transient simulations, including water isotopes,  
 580 of the AIM events and the early-Holocene maximum, as recently achieved for Dansgaard-  
 581 Oeschger events in Greenland (Sime et al., 2019), and of the deglaciation.

582 Clearly, a single  $\partial(\delta^{18}\text{O})/\partial T$  scaling does not capture all of the variability in our tem-  
 583 perature reconstruction. We explored calibrations separated by frequency and time pe-  
 584 riod (*i.e.*, millennial versus glacial-interglacial frequencies and Holocene versus glacial  
 585 time periods), but find the resulting fits were not statistically distinguishable from that  
 586 of the single scaling. Thus, there is no evidence of the large change in scaling that has  
 587 been observed in Greenland ice cores (Cuffey et al., 1995), attributable primarily to changes  
 588 in the seasonality of precipitation (Steig et al., 1994; Werner et al., 2000). Our results  
 589 agree well with the assumption generally made in East Antarctica that the slope remains  
 590 constant through time (*e.g.*, Jouzel et al. (2003)), but show that this slope cannot be as-  
 591 sumed to be the same as the modern spatial relationship.

592 While our calibration yields a significantly greater slope than has been generally used  
 593 in previous work, this slope is consistent with isotope-modeling results. Modeling work  
 594 has shown that the sensitivity of  $\delta^{18}\text{O}$  to temperature should increase at sites with colder  
 595 mean-annual temperatures and higher elevations in Antarctica. For example, Markle (2017)  
 596 obtains  $\partial(\delta^{18}\text{O})/\partial T \sim 0.8\text{‰}^\circ\text{C}^{-1}$  for a location like WAIS Divide, in agreement with  
 597 the borehole temperature calibration, and  $\partial(\delta^{18}\text{O})/\partial T \sim 1\text{‰}^\circ\text{C}^{-1}$  for South Pole. This  
 598 difference in sensitivity occurs because air masses traveling to higher elevations are on  
 599 different moist isentropic surfaces and experience greater rainout for a given change in  
 600 temperature (Bailey et al., 2019).

## 6.3 Upstream Corrections and Site Reconstructions

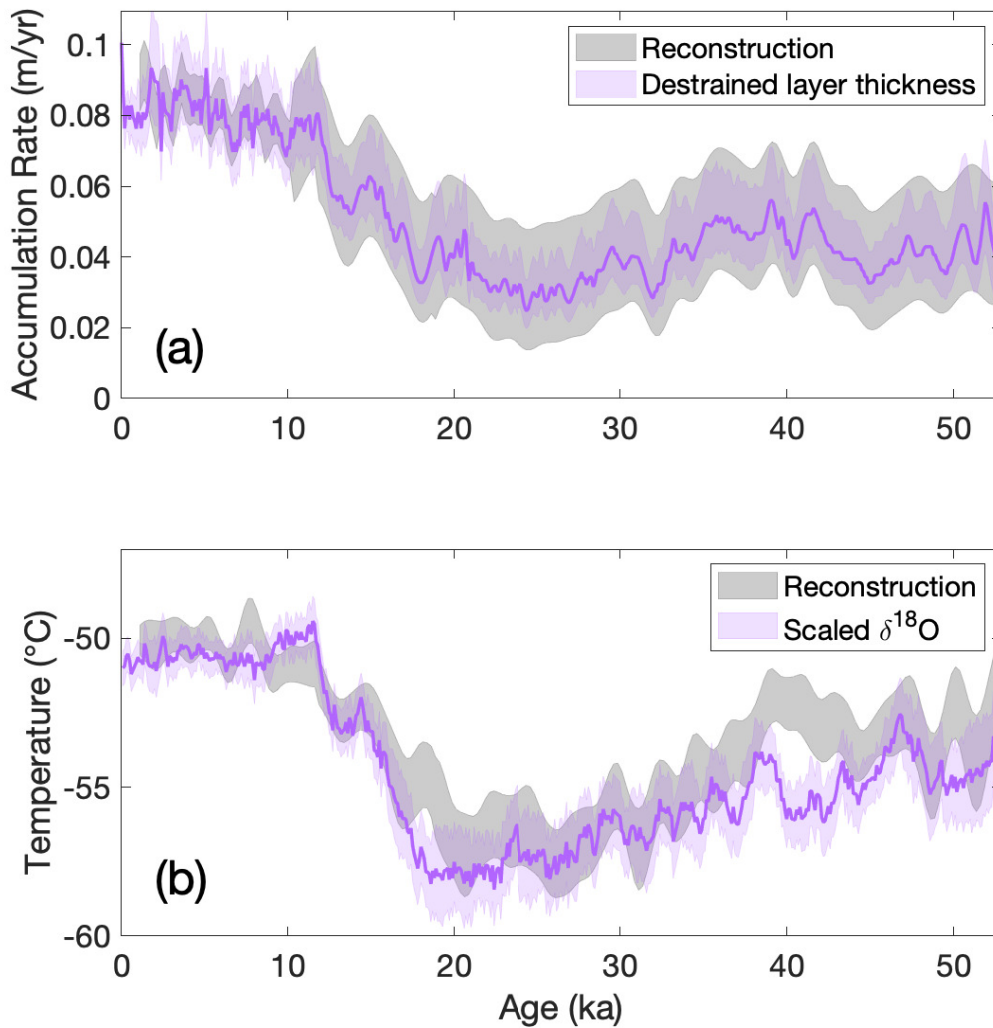


Figure 8: Advection-corrected reconstructions of accumulation rate and temperature at the South Pole site. Advection corrections are based on Lilien et al. (2018) and Fudge et al. (2020), as described in the text. All shading indicates two s.d. uncertainty. Panel (a) shows two advection-corrected accumulation-rate histories: the main reconstruction (grey) and the high-frequency accumulation-rate history from destaining 100-year average layer thicknesses (purple), corresponding to the ice-core histories shown in Figure 6b. Panel (b) compares the advection-corrected temperature estimates from our reconstruction and from the scaled  $\delta^{18}\text{O}$ , averaged to 100-year resolution. Uncertainty takes into account the correlation coefficient between the temperature reconstruction and the scaled isotope estimate.

Because SPC14 was drilled far from the divide, deeper ice in the core originated increasingly farther upstream. To obtain accurate climate histories, it is necessary to remove the influence of flow from upstream where the climate conditions are different. We cor-

605 rect for advection of ice based on Lilien et al. (2018) and Fudge et al. (2020). Using mea-  
 606 surements of surface velocities and the pattern of modern accumulation rate upstream  
 607 along the flowline, Lilien et al. (2018) correlated the measured ice-core layer thicknesses  
 608 with the expected layer thickness due to advection through the upstream accumulation-  
 609 rate pattern. This provides a unique constraint on the origin of ice for the past 10 ka and  
 610 indicates an increase in surface flow speed of about 15% through that time period. We  
 611 rely on this novel constraint for our advection correction rather than the advection pre-  
 612 dicted with the steady-state flowband model, and we note that the two approaches give  
 613 similar trajectories for the reversal in the thinning function at 7 ka (Figure S13). Fudge  
 614 et al. (2020) measured  $\delta^{18}\text{O}$  values using 10-m firn cores at 12.5 km intervals along the  
 615 flowline to determine an appropriate correction for  $\delta^{18}\text{O}$ . Fudge et al. (2020) also mea-  
 616 sured 10-m firn temperatures, and while the results were inconclusive, they were con-  
 617 sistent with a typical  $10^\circ\text{C km}^{-1}$  lapse rate (dry adiabatic). Using this information, we  
 618 apply corrections to the “ice core” reconstructions described above to produce “site” re-  
 619 constructions of accumulation rate and temperature.

620 The upstream correction to accumulation rate is separated into two time intervals. For  
 621 ages younger than 10.2 ka, the surface accumulation-rate pattern upstream of the core  
 622 is known (Lilien et al., 2018). We apply these modern surface variations as a correction  
 623 by adding the deviation from the mean value to the accumulation-rate ice-core recon-  
 624 struction. This correction damps the variability of Holocene accumulation rate in the  
 625 site reconstruction compared with the ice-core reconstruction, but it does not affect the  
 626 trend of the mean. For ages older than 10.2 ka, there is an insignificant linear trend in  
 627 the accumulation rate along the 100 km flowline such that Fudge et al. (2020) suggest  
 628 no long-term advection correction. Thus we make no correction to the ice-core recon-  
 629 struction for ages older than 10.2 ka. We do not attempt to correct for the impact of spa-  
 630 tial variability on the ice-core reconstruction for these older ages, but note that non-climate  
 631 variations of roughly 15% are expected to occur on millennial timescales. We estimate  
 632 the uncertainty in the accumulation-rate upstream correction using the variations in ac-  
 633 cumulation rate along the flowline. For ages older than 10.2 ka, we assume the  $1\sigma$  un-  
 634 certainty is equal to the standard deviation of the upstream accumulation-rate pattern.  
 635 For ages younger than 10.2 ka, the uncertainty is lower because we have removed much  
 636 of the impact of advection; however, the correction is not perfect. Roughly 2/3 of the  
 637 variance in the measured annual-layer thicknesses is explained by advection (Lilien et al.,  
 638 2018). We thus conservatively assume a  $1\sigma$  uncertainty is equivalent to half the stan-  
 639 dard deviation. Adding this uncertainty in quadrature to the uncertainty of the ice-core  
 640 accumulation-rate estimates shown in Figure 6b, we produce the site accumulation-rate  
 641 histories and their uncertainty bounds shown in Figure 8a. The grey bounds show the  
 642 advection-corrected accumulation-rate reconstruction from our inverse approach and the  
 643 purple bounds show the advection-corrected high-frequency accumulation-rate estimate  
 644 from destraining the layer-thickness data with our thinning function reconstruction.

645 To correct the ice-core temperature reconstruction, we apply the dry adiabatic lapse rate  
 646 of  $10^\circ\text{C km}^{-1}$  to the elevation correction given by Fudge et al. (2020) to produce the grey  
 647 shading in Figure 8b. We do not quantify uncertainty associated with this correction.  
 648 For comparison with the water-isotope record, we correct the  $\delta^{18}\text{O}$  with the water-isotope  
 649 correction given by Fudge et al. (2020) and scale the record using the best-fit linear cal-  
 650 ibration with the site reconstruction (also  $0.99\text{‰}^\circ\text{C}^{-1}$ ) to produce the purple curve in  
 651 Figure 8b. The uncertainty in the advection correction takes into account the correla-  
 652 tion coefficient between the temperature reconstruction and the scaled isotope estimate.

653 We use our site temperature reconstruction to determine the magnitude of glacial-interglacial  
 654 temperature change at South Pole. We define this change as the difference in the mean  
 655 temperature within the intervals of 0.5 - 2.5 ka and 19.5 - 22.5 ka. Note that our recon-  
 656 struction ends at 0.5 ka, not the present, because the upper  $\sim 500$  years of the record is  
 657 in the firn; hence,  $\Delta\text{age}$  is undefined and diffusion of water isotopes is still in progress.

658 The choice of the last glacial maximum (LGM) window avoids the prominent warming  
 659 of the Antarctic Isotope Maximum (AIM2) event. The site temperature reconstruction  
 660 gives a glacial-interglacial temperature change at the South Pole site of  $6.65 \pm 0.96^\circ\text{C}$  (one  
 661 s.d.). The site scaled  $\delta^{18}\text{O}$  gives a glacial-interglacial temperature change of  $7.15 \pm 0.68^\circ\text{C}$   
 662 (one s.d.).

663 Our site temperature estimate indicates a 2 to  $3.5^\circ\text{C}$  lower glacial-interglacial surface tem-  
 664 perature change than that reconstructed from other ice cores in east Antarctica, which  
 665 is generally taken to be  $9^\circ\text{C}$  (Parrenin et al., 2013). Importantly, assessment of uncer-  
 666 tainty in our calculations suggests that this key finding is conservative. In particular, there  
 667 is some indication that firn-densification models may be biased to produce diffusive col-  
 668 umn heights that are too large at cold temperatures (Landais et al., 2006; Dreyfus et al.,  
 669 2010; Freitag et al., 2013; Bréant et al., 2017). If the Herron-Langway model were in fact  
 670 unbiased, then even warmer LGM temperatures would be required.

671 The difference between our results and the conventional  $9^\circ\text{C}$  value cannot be readily at-  
 672 tributed to elevation change at South Pole, which is unlikely to have been more than 100 m  
 673 thinner during the last glacial maximum, thus accounting for at most about  $1^\circ\text{C}$  of the  
 674 difference, assuming a dry adiabatic lapse rate of  $10^\circ\text{C km}^{-1}$ . (Constraints from ice sheet  
 675 models and geodetic data (Pollard and DeConto, 2009; Whitehouse et al., 2012; Briggs  
 676 et al., 2014; Argus et al., 2014; Golledge et al., 2014; Roy and Peltier, 2015) show a near-  
 677 zero mean elevation change, with a standard deviation of 50 m.)

678 Our results show that the commonly-used  $9^\circ\text{C}$  value for glacial-interglacial change in East  
 679 Antarctica, which is based on water isotopes unconstrained by the independent estimates  
 680 we use here, is too large. This finding may resolve an apparent disagreement, first rec-  
 681 ognized at least three decades ago (Crowley and North, 1991), between ice-core-based  
 682 temperature estimates and results from general circulation models (GCMs), which pro-  
 683 duce cold-enough LGM temperatures only if surface elevations significantly higher than  
 684 present are assumed (e.g., Masson-Delmotte et al., 2006; Lee et al., 2008; Werner et al.,  
 685 2018), or other boundary conditions, such as extensive sea ice, are imposed (Schoene-  
 686 mann et al., 2014). Such GCM estimates are in better agreement with our results if cor-  
 687 rected for the prescribed elevation changes, consistent with the smaller changes in East  
 688 Antarctic ice elevations during the LGM indicated by more recent results than those sug-  
 689 gested by earlier work (e.g., Peltier, 2004).

## 690 7 Conclusions

691 The South Pole ice core (SPC14) provides the opportunity to obtain reconstructions of  
 692 important climate variables using multiple independent constraints. SPC14 has an em-  
 693 pirical measure of the gas-age ice-age difference,  $\Delta\text{age}$ , obtained independently of firn-  
 694 densification modeling (Epifanio et al., 2020). We also present a new continuous record  
 695 of water-isotope diffusion length. Both  $\Delta\text{age}$  and diffusion length depend on firn prop-  
 696 erties, which in turn depend on the snow-accumulation rate and firn temperature. The  
 697 water-isotope diffusion length provides an important additional constraint on the ice-  
 698 thinning function, which relates measured layer thickness with the original accumula-  
 699 tion rate at the surface. Layer thickness variations in SPC14 are well constrained by the  
 700 ice timescale for the core, developed by annual-layer counting through the Holocene and  
 701 by stratigraphic matches with the well-dated West Antarctic Ice Sheet Divide ice core  
 702 (Winski et al., 2019). We have used a statistical inverse approach to combine informa-  
 703 tion from all these data sets to obtain an ensemble of self-consistent temperature, accumula-  
 704 tion-rate, and ice-thinning histories.

705 Our estimate of the thinning function for SPC14 indicates greater variations in thinning  
 706 rate, in particular less thinning at depth, than can be captured with a simple one-dimensional  
 707 ice-flow parameterization such as the commonly-used Dansgaard-Johnsen model. Vari-  
 708 ations in thinning comparable in timing and magnitude to our results are supported by

709 a 2.5-D flowband model that accounts for variations in bedrock topography upstream  
 710 of the drill site. The thinning function reconstruction is particularly important because  
 711 SPC14 was drilled more than 200 km away from the ice divide and the surface velocity  
 712 is high ( $10 \text{ m a}^{-1}$ ) (Casey et al., 2014). Our results demonstrate the value of using water-  
 713 isotope diffusion length, in conjunction with annual-layer thickness, to more precisely  
 714 constrain the thinning function. This approach, also employed by Gkinis et al. (2014)  
 715 for a Greenland ice core, is entirely independent of the  $\delta^{15}\text{N}$  method of Parrenin et al.  
 716 (2012), and provides an important new observational constraint on ice-sheet flow.

717 Our temperature reconstruction serves two important purposes. First, it provides the  
 718 first empirical, high-frequency estimate of temperature for an East Antarctic ice-core site  
 719 that does not depend on the traditional water-isotope paleothermometer. It thus enables  
 720 an independent calibration of the isotope-temperature sensitivity,  $\partial(\delta^{18}\text{O})/\partial T$ , similar  
 721 to what has been done in central Greenland and in West Antarctica using borehole ther-  
 722 mometry (Cuffey et al., 1995, 2016). Moreover, our approach preserves additional high-  
 723 frequency information that is not available from the highly diffused borehole-temperature  
 724 measurements. We find no evidence of a time- or frequency-dependence to the  $\partial(\delta^{18}\text{O})/\partial T$   
 725 relationship, in contrast to the case for Greenland. Second, our results indicate a smaller  
 726 glacial-interglacial temperature change at South Pole than previously estimated elsewhere  
 727 in East Antarctica. Our results yield a glacial-interglacial change of  $6.7 \pm 1.0^\circ\text{C}$  (one s.d.).  
 728 This value is in better agreement with results from climate models, which generally match  
 729 the much colder LGM temperatures obtained from traditional isotope-temperature scal-  
 730 ing only when high ice-sheet elevations are assumed. The difficulty of reconciling tem-  
 731 perature estimates from climate models and ice-core data has been noted in the liter-  
 732 ature for more than three decades (Crowley and North, 1991; Masson-Delmotte et al.,  
 733 2005; Lee et al., 2008; Schoenemann et al., 2014). Our results thus lend greater confi-  
 734 dence to the fidelity of climate-model simulations of last glacial maximum climate.

## 735 8 Data Availability

736 The published data set associated with this paper, including water isotope diffusion lengths  
 737 and all of the reconstructions discussed in this manuscript, can be accessed through the  
 738 USAP Data Center (DOI: 10.15784/601396). The SPC14 high-resolution water stable  
 739 isotope record published with this paper can also be accessed through the USAP Data  
 740 Center (DOI: 10.15784/601239). The radar data used in the ice-flow modeling can be  
 741 accessed through the USAP Data Center at <https://www.usap-dc.org/view/project/p0000200>.  
 742 The code used in this work is publicly available at <https://doi.org/10.5281/zenodo.4579416>,  
 743 and the Community Firn Model is available at <https://doi.org/10.5281/zenodo.3585885>.

## 744 Acknowledgments

745 This work was funded through grants from the US National Science Foundation (E.J.S.  
 746 (1143105 and 1141839), C.B. (1643394 and 1443472), M.R.K. and others (1443471)). We  
 747 thank J.P. Severinghaus for providing  $^{15}\text{N}$  data collected under grant NSF1443710. We  
 748 thank G.H. Roe, B.R. Markle, and D. Shapero for suggestions on this work, and M. Twick-  
 749 ler and J. Souney for their work administering the SPICEcore project. We thank the SPICEcore  
 750 field team, the 109th New York Air National Guard, and the National Science Founda-  
 751 tion Ice Core Facility, for the collection, transport, processing, and storage of the core.  
 752 Finally, we thank the two reviewers of this manuscript for their very thorough comments  
 753 and suggestions, which helped considerably in compiling the final publication.

## 754 References

755 Argus, D. F., Peltier, W. R., Drummond, R. & Moore, A. W. (2014). The Antarc-  
 756 tica component of postglacial rebound model ICE-6G C (VM5a) based upon GPS  
 757 positioning, exposure age dating of ice thicknesses, and relative sea level histories.  
 758 *Geophys. J. Int.*, 198(1), 537–563. <https://doi.org/10.1093/gji/ggu140>

- 759 Bailey, A., Singh, H. K. A., & Nusbaumer, J. (2019). Evaluating a moist isen-  
760 tropic framework for poleward moisture transport: implications for water  
761 isotopes over Antarctica. *Geophysical Research Letters*, *46*(13), 7819–7827.  
762 <https://doi.org/10.1029/2019GL082965>
- 763 Barkan, E., & Luz, B. (2007). Diffusivity fractionations of  $\text{H}_2^{16}\text{O}/\text{H}_2^{17}\text{O}$   
764 and  $\text{H}_2^{16}\text{O}/\text{H}_2^{18}\text{O}$  in air and their implications for isotope hydrology.  
765 *Rapid Communications in Mass Spectrometry*, *21*(18), 2999–3005.  
766 <https://doi.org/10.1002/rcm.3180>
- 767 Bazin, L., Landais, A., Lemieux-Dudon, B., Toyé Mahamadou Kele, H., Veres, D.,  
768 Parrenin, F., et al. (2013). An optimized multi-proxy, multi-site Antarctic ice and  
769 gas orbital chronology (AICC2012): 120–800 ka. *Climate of the Past*, *9*, 1715–  
770 1731. <https://doi.org/10.5194/cp-9-1715-2013>
- 771 Bintanja, R., & van de Wal, R. S. W. (2008). North American ice-sheet dynam-  
772 ics and the onset of 100,000-year glacial cycles. *Nature*, *454*(7206), 869–872.  
773 <https://doi.org/10.1038/nature07158>
- 774 Blunier, T., & Schwander, J. (2000). Gas enclosure in ice: age difference and frac-  
775 tionation. *Physics of Ice Core Records* 307–326. Hokkaido University Press.
- 776 Bréant, C., Martinerie, P., Orsi, A., Arnaud, L., & Landais, A. (2017). Mod-  
777 elling firn thickness evolution during the last deglaciation: constraints on  
778 sensitivity to temperature and impurities. *Climate of the Past*, *13*, 833–853.  
779 <https://doi.org/10.5194/cp-13-833-2017>
- 780 Briggs, R. D., Pollard, T., & Tarasov, L. (2014). A data-constrained large ensemble  
781 analysis of Antarctic evolution since the Eemian. *Quaternary Science Reviews*,  
782 *103*, 91–115. <https://doi.org/10.1016/j.quascirev.2014.09.003>
- 783 Buizert, C., Martinerie, P., Petrenko, V. V., Severinghaus, J. P., Trudinger, C. M.,  
784 Witrant, E., Steele, L. P., et al. (2012). Gas transport in firn: multiple-tracer  
785 characterisation and model intercomparison for NEEM, Northern Greenland. *At-  
786 mospheric Chemistry and Physics*, *12*(9), 4259–4277. [https://doi.org/10.5194/acp-  
787 12-4259-2012](https://doi.org/10.5194/acp-12-4259-2012)
- 788 Buizert, C., Sowers, T., & Blunier, T. (2013). Assessment of diffu-  
789 sive isotopic fractionation in polar firn, and application to ice core  
790 trace gas records. *Earth and Planetary Science Letters*, *361*, 110–119.  
791 <https://doi.org/10.1016/j.epsl.2012.11.039>
- 792 Buizert, C., Gkinis, V., Severinghaus, J. P., He, F., Lecavalier, B. S., Kindler,  
793 P., Brook, E. J., et al. (2014). Greenland temperature response to cli-  
794 mate forcing during the last deglaciation. *Science*, *345*(6201), 1177–1180.  
795 <https://doi.org/10.1126/science.1254961>
- 796 Buizert, C., Cuffey, K. M., Severinghaus, J. P., Baggenstos, D., Fudge, T. J., Steig,  
797 E. J., Sowers, T. A., et al. (2015). The WAIS divide deep ice core WD2014  
798 chronology–Part 1: methane synchronization (68–31 kaBP) and the gas age–ice  
799 age difference. *Climate of the Past*, *11*, 153–173. [https://doi.org/10.5194/cp-11-  
800 153-2015](https://doi.org/10.5194/cp-11-153-2015)
- 801 Casey, K. A., Fudge, T. J., Neumann, T. A., Steig, E. J., Cavitte, M. G. P.,  
802 & Blankenship, D. D. (2014). The 1500 m South Pole ice core: Recover-  
803 ing a 40 ka environmental record. *Annals of Glaciology*, *55*(68), 137–146.  
804 <https://doi.org/10.3189/2014AoG68A016>
- 805 Catania, G, C. Hulbe, & Conway, H. (2010). Grounding-line basal melt rates deter-  
806 mined using radar-derived internal stratigraphy. *Journal of Glaciology*, *56*(197),  
807 545–554. <https://doi.org/10.3189/002214310792447842>
- 808 Crowley, T. J., & North, G. R. (1991). *Paleoclimatology*. New York, NY: Oxford  
809 University Press.
- 810 Cuffey, K. M., & Steig, E. J. (1998). Isotopic diffusion in polar firn: Implica-  
811 tions for interpretation of seasonal climate parameters in ice-core records,  
812 with emphasis on central Greenland. *Journal of Glaciology*, *44*(147), 273–284.

- 813 <https://doi.org/10.3189/S0022143000002616>
- 814 Cuffey, K. M., & Paterson, W. S. B. (2010). The physics of glaciers. Academic Press.
- 815 Cuffey, K. M., Clow, G. D., Alley, R. B., Stuiver, M., Waddington, E.  
816 D., & Saltus, R. W. (1995). Large arctic temperature change at the  
817 Wisconsin-Holocene glacial transition. *Science*, *270*(5235), 455–458.  
818 <https://doi.org/10.1126/science.270.5235.455>
- 819 Cuffey, K. M., Clow, G. D., Steig, E. J., Buizert, C., Fudge, T. J., Koutnik, M.,  
820 Severinghaus, J. P., et al. (2016). Deglacial temperature history of West Antarc-  
821 tica. *Proceedings of the National Academy of Sciences*, *113*(50), 14249–14254.  
822 <https://doi.org/10.1073/pnas.1609132113>
- 823 Dahl-Jensen, D., Mosegaard, K., Gundestrup, N., Clow, G. D., Johnsen,  
824 S. J., Hansen, A. W., & Balling, N. (1998). Past temperatures di-  
825 rectly from the Greenland ice sheet. *Science*, *282*(5387), 268–271.  
826 <https://doi.org/10.1126/science.282.5387.268>
- 827 Dansgaard, W. (1964). Stable isotopes in precipitation. *Tellus B*, *16*(4), 436–468.  
828 <https://doi.org/10.3402/tellusa.v16i4.8993>
- 829 Dansgaard, W., & Johnsen, S. J. (1969). A flow model and a time scale for the  
830 ice core from Camp Century, Greenland. *Journal of Glaciology*, *8*(53), 215–223.  
831 <https://doi.org/10.3189/S0022143000031208>
- 832 Dreyfus, G. B., Jouzel, J., Bender, M. L., Landais, A., Masson-Delmotte,  
833 V., & Leuenberger, M. (2010). Firn processes and  $\delta^{15}\text{N}$ : potential for a  
834 gas-phase climate proxy. *Quaternary Science Reviews*, *29*(1-2), 28-42.  
835 <https://doi.org/10.1016/j.quascirev.2009.10.012>
- 836 Epifanio, J. A., Brook, E. J., Buizert, C., Edwards, J. S., Sowers, T. A., Kahle, E.  
837 C., Severinghaus, J. P., Steig, E. J., Winski, D. A., Osterberg, E. C., Fudge, T.  
838 J., Aydin, M., Hood, E., Kalk, M., Kreutz, K. J., Ferris, D. G., & Kennedy, J.  
839 A. (2020). The SP19 chronology for the South Pole Ice Core—Part 2: gas chronol-  
840 ogy,  $\Delta\text{age}$ , and smoothing of atmospheric records. *Climate of the Past*, *16*(6),  
841 2431–2444. <https://doi.org/10.5194/cp-16-2431-2020>
- 842 EPICA Community Members. 2004. Eight glacial cycles from an Antarctic ice core.  
843 *Nature*, *429*, 623–628. <https://doi.org/10.1038/nature02599>
- 844 Fausto, R. S., Box, J. E., Vandecrux, B. R. M., van As, D., Steffen, K., MacFerrin,  
845 M. J., Charalampidis, C., et al. (2018). A snow density dataset for improving sur-  
846 face boundary conditions in Greenland ice sheet firn modeling. *Frontiers in Earth*  
847 *Science*, *6*, 51. <https://doi.org/10.3389/feart.2018.00051>
- 848 Forsberg, R., Olesen, A. V., Ferraccioli, F., Jordan, T., Corr, H., & Mat-  
849 suoka, K. (2017). PolarGap 2015/16: Filling the GOCE polar gap in Antarc-  
850 tica and ASIRAS flight around South Pole. Radar grids available at: *ftp* :  
851 [//ftp.bas.ac.uk/tomj/PolarGAP/PolarGAP\\_radar\\_grids.zip](ftp://ftp.bas.ac.uk/tomj/PolarGAP/PolarGAP_radar_grids.zip)
- 852 Freitag, J., Kipfstuhl, S., Laepple, T., & Wilhelms, F. (2013). Impurity-controlled  
853 densification: a new model for stratified polar firn. *Journal of Glaciology*, *59*(218),  
854 1163–1169. <https://doi.org/10.3189/2013JoG13J042>
- 855 Fudge, T. J., Waddington, E. D., Conway, H., Lundin, J. M. D., & Taylor, K.  
856 (2014). Interpolation methods for Antarctic ice-core timescales: application to  
857 Byrd, Siple Dome and Law Dome ice cores. *Climate of the Past*, *10*(3), 1195–  
858 1209. <https://doi.org/10.5194/cp-10-1195-2014>
- 859 Fudge, T. J., Markle, B. R., Cuffey, K. M., Buizert, C., Taylor, K. C., Steig, E.  
860 J., Koutnik, M., et al. (2016). Variable relationship between accumulation and  
861 temperature in West Antarctica for the past 31,000 years. *Geophysical Research*  
862 *Letters*, *43*(8), 3795–3803. <https://doi.org/10.1002/2016GL068356>
- 863 Fudge, T. J., Biyani, S. C., Clemens-Sewall, D., & Hawley, R. L. (2019). Constraining  
864 geothermal flux at coastal domes of the Ross Ice Sheet, Antarctica. *Geophys-  
865 ical Research Letters*, *46*(22), 13090–13098. <https://doi.org/10.1029/2019GL084332>

- 866 Fudge, T. J., Lilien, D. A., Koutnik, M., Conway, H., Stevens, C. M., Waddington,  
867 E. D., Steig, E. J., Schauer, A. J., & Holschuh, N. (2020). Advection and non-  
868 climate impacts on the South Pole Ice Core. *Climate of the Past*, *16*, 819–832.  
869 <https://doi.org/10.5194/cp-16-819-2020>
- 870 Gades, A. M., Raymond, C. F., Conway, H., & Jacobel, R. W., (2000). Bed prop-  
871 erties of Siple Dome and adjacent ice streams West Antarctica, inferred from  
872 radio-echo sounding measurements. *Journal of Glaciology*, *46*(152), 88–94.  
873 <https://doi.org/10.3189/172756500781833467>
- 874 Gelman, A., Roberts, G. & Gilks W. (1996). Efficient Metropolis jumping rules, in  
875 Bayesian Statistics 5, Berger, J. O., Bernardo, J. M., Dawid, A. P. and Smith, A.  
876 F. M. (eds), Oxford University Press.
- 877 Gkinis, V., Simonsen, S. B., Buchardt, S. L., White, J. W. C., & Vinther, B. M.  
878 (2014). Water isotope diffusion rates from the NorthGRIP ice core for the last  
879 16,000 years - glaciological and paleoclimatic implications. *Earth and Planetary*  
880 *Science Letters*, *405*, 132–141. <https://doi.org/10.1016/j.epsl.2014.08.022>
- 881 Gkinis, V., Holme, C., Kahle, E.C., Stevens, C.M., Steig, E.J., & Vinther,  
882 B.M. (2021). Numerical experiments on firn isotope diffusion with  
883 the Community Firn Model. *Journal of Glaciology*, *67*(263), 450-472.  
884 <https://doi.org/10.1017/jog.2021.1>
- 885 Gолledge, N. R., Menviel, L., Carter, L., Fogwill, C. J., England, M. H., Cortese,  
886 G., & Levy, R. H. (2014). Antarctic contribution to meltwater pulse 1A from  
887 reduced Southern Ocean overturning. *Nature Communications*, *5*(1), 1–10.  
888 <https://doi.org/10.1038/ncomms6107>
- 889 Goujon, C., Barnola, J. M., & Ritz, C. (2003). Modeling the densification of polar  
890 firn including heat diffusion: Application to close-off characteristics and gas iso-  
891 topic fractionation for Antarctica and Greenland sites. *Journal of Geophysical*  
892 *Research: Atmospheres*, *108*(D24). <https://doi.org/10.1029/2002JD003319>
- 893 Grachev, A. M., & Severinghaus, J. P. (2003). Laboratory determination of ther-  
894 mal diffusion constants for  $^{29}\text{N}_2/^{28}\text{N}_2$  in air at temperatures from 60 to 0 C for  
895 reconstruction of magnitudes of abrupt climate changes using the ice core fos-  
896 sil-air paleothermometer. *Geochimica et Cosmochimica Acta*, *67*(3), 345–360.  
897 [https://doi.org/10.1016/S0016-7037\(02\)01115-8](https://doi.org/10.1016/S0016-7037(02)01115-8)
- 898 Gudmundsson, G. H., & Raymond, M. (2008). On the limit to resolution and in-  
899 formation on basal properties obtainable from surface data on ice streams. *The*  
900 *Cryosphere*, *2*(3), 413–445. <https://doi.org/10.5194/tc-2-167-2008>
- 901 Guillevic, M., Bazin, L., Landais, A., Kindler, P., Orsi, A., Masson-Delmotte, V.,  
902 Martinerie, P., et al. (2013). Spatial gradients of temperature, accumulation and  
903  $\delta^{18}\text{O}$ -ice in Greenland over a series of Dansgaard-Oeschger events. *Climate of the*  
904 *Past*, *9*(3), 1029–1051. <https://doi.org/10.5194/cp-9-1029-2013>
- 905 Hammer, C. U., Clausen, H. B., Dansgaard, W., Gundestrup, N., Johnsen, S. J.,  
906 & Reeh, N. (1978). Dating of Greenland ice cores by flow models, isotopes,  
907 volcanic debris, and continental dust. *Journal of Glaciology*, *20*(82), 3–26.  
908 <https://doi.org/10.3189/S0022143000021183>
- 909 Herron, M. M., & Langway, C. C. (1980). Firn densification:  
910 an empirical model. *Journal of Glaciology*, *25*(93), 373–385.  
911 <https://doi.org/10.3189/S0022143000015239>
- 912 Holme, C., Gkinis, V., & Vinther, B. M. (2018). Molecular diffusion of stable water  
913 isotopes in polar firn as a proxy for past temperatures. *Geochimica et Cosmochim-*  
914 *ica Acta*, *225*, 128–145. <https://doi.org/10.1016/j.gca.2018.01.015>
- 915 Huber, C., Leuenberger, M., Spahni, R., Flückiger, J., Schwander, J., Stocker, T.  
916 F., Jouzel, J., et al. (2006). Isotope calibrated Greenland temperature record over  
917 Marine Isotope Stage 3 and its relation to  $\text{CH}_4$ . *Earth and Planetary Science*  
918 *Letters*, *243*(3-4), 504–519. <https://doi.org/10.1016/j.epsl.2006.01.002>

- 919 Johnsen, S. J. (1977). Stable isotope homogenization of polar firn and ice, in *Proc.*  
 920 *of Symp. on Isotopes and Impurities in Snow and Ice*, pp. 210–219, Int. Assoc. of  
 921 Hydrol. Sci., Gentbrugge, Belgium.
- 922 Johnsen, S. J., Clausen, H. B., Cuffey, K. M., Hoffmann, G., Schwander, J., &  
 923 Creyts, T. (2000). Diffusion of stable isotopes in polar firn and ice: The isotope  
 924 effect in firn diffusion. T. Hondoh (Ed.), *Physics of Ice Core Records*, Hokkaido  
 925 University Press, Sapporo (2000), pp. 121–140.
- 926 Jones, T. R., Cuffey, K. M., White, J. W. C., Steig, E. J., Buizert, C., Markle,  
 927 B. R., McConnell, J. R., & Sigl, M. (2017a). Water isotope diffusion in the WAIS  
 928 Divide ice core during the Holocene and last glacial. *Journal of Geophysical Re-*  
 929 *search: Earth Surface*, *122*(1), 290–309. <https://doi.org/10.1002/2016JF003938>
- 930 Jones, T. R., White, J. W. C., Steig, E. J., Vaughn, B. H., Morris, V., Gkinis, V.,  
 931 Markle, B. R., & Schoenemann, S. W. (2017b). Improved methodologies for con-  
 932 tinuous flow analysis of stable water isotopes in ice cores. *Atmospheric Measure-*  
 933 *ment Techniques*, *10*, 617–632. <https://doi.org/10.5194/amt-10-617-2017>
- 934 Jordan, T. A., Martin, C., Ferraccioli, F., Matsuoka, K., Corr, H., Forsberg, R., Ole-  
 935 sen, A., & Siegert, M. (2018). Anomalously high geothermal flux near the South  
 936 Pole. *Scientific Reports*, *8*(1), 1–8. <https://doi.org/10.1038/s41598-018-35182-0>
- 937 Jouzel, J., Barkov, N. I., Barnola, J. M., Bender, M., Chappellaz, J., Gen-  
 938 thon, C., Raynaud, D., et al. (1993). Extending the Vostok ice-core record of  
 939 palaeoclimate to the penultimate glacial period. *Nature*, *364*(6436), 407–412.  
 940 <https://doi.org/10.1038/364407a0>
- 941 Jouzel, J., Vimeux, F., Caillon, N., Delaygue, G., Hoffmann, G., Masson-Delmotte,  
 942 V., & Parrenin, F. (2003). Magnitude of isotope/temperature scaling for inter-  
 943 pretation of central Antarctic ice cores. *Journal of Geophysical Research: Atmo-*  
 944 *spheres*, *108*(D12). <https://doi.org/10.1029/2002JD002677>
- 945 Jouzel, J., Masson-Delmotte, V., Cattani, O., Dreyfus, G., Falourd, S., Hoff-  
 946 mann, G., Fischer, H., et al. (2007). Orbital and millennial Antarctic cli-  
 947 mate variability over the past 800,000 years. *Science*, *317*(5839), 793–796.  
 948 <https://doi.org/10.1126/science.1141038>
- 949 Kahle, E. C., Holme, C., Jones, T. R., Gkinis, V., & Steig, E. J. (2018). A gener-  
 950 alized approach to estimating diffusion length of stable water isotopes from ice-  
 951 core data. *Journal of Geophysical Research: Earth Surface*, *123*(10), 2377–2391.  
 952 <https://doi.org/10.1029/2018JF004764>
- 953 Kahle, E. C. (2020). Climate reconstructions from ice cores: New techniques to un-  
 954 derstand the information preserved in the South Pole ice core (Doctoral disserta-  
 955 tion, University of Washington, Seattle, USA). <http://hdl.handle.net/1773/45398>
- 956 Khan, A., Mosegaard, K., & Rasmussen, K. L. (2000). A new seismic ve-  
 957 locity model for the Moon from a Monte Carlo inversion of the Apollo  
 958 lunar seismic data. *Geophysical Research Letters*, *27*(11), 1591–1594.  
 959 <https://doi.org/10.1029/1999GL008452>
- 960 Kindler, P., Guillevic, M., Baumgartner, M. F., Schwander, J., Landais, A.,  
 961 & Leuenberger, M. (2014). Temperature reconstruction from 10 to 120  
 962 kyr b2k from the NGRIP ice core. *Climate of the Past*, *10*(2), 887–902.  
 963 <https://doi.org/10.5194/cp-10-887-2014>
- 964 Koutnik, M. R., Fudge, T. J., Conway, H., Waddington, E. D., Neumann, T. A.,  
 965 Cuffey, K. M., Taylor, K. C., et al. (2016). Holocene accumulation and ice flow  
 966 near the West Antarctic Ice Sheet Divide ice core site. *Journal of Geophysical*  
 967 *Research: Earth Surface*, *121*(5), 907–924. <https://doi.org/10.1002/2015JF003668>
- 968 Lamb, K. D., Clouser, B. W., Bolot, M., Sarkozy, L., Ebert, V., Saathoff, H.,  
 969 Mohler, O., & Moyer, E. J. (2017). Laboratory measurements of HDO/H<sub>2</sub>O  
 970 isotopic fractionation during ice deposition in simulated cirrus clouds.  
 971 *Proceedings of the National Academy of Sciences*, *114*(22), 5612–5617.  
 972 <https://doi.org/10.1073/pnas.1618374114>

- 973 Landais, A., Barnola, J.M., Kawamura, K., Caillon, N., Delmotte, M., van Om-  
 974 men, T., Dreyfus, G., Jouzel, J., Masson-Delmotte, V., Minster, B., Freitag, J.,  
 975 Leuenberger, M., Schwander, J., Huber, C., Etheridge, D., & Morgan, V. (2006).  
 976 Firn-air  $\delta^{15}\text{N}$  in modern polar sites and glacial-interglacial ice: a model-data mis-  
 977 match during glacial periods in Antarctica? *Quaternary Science Reviews*, *25*(1-2),  
 978 499–62. <https://doi.org/10.1016/j.quascirev.2005.06.007>
- 979 Lazzara, M. A., Keller, L. M., Markle, T., & Gallagher, J. (2012). Fifty-year  
 980 Amundsen–Scott South Pole station surface climatology. *Atmospheric Research*,  
 981 *118*, 240–259. <https://doi.org/10.1016/j.atmosres.2012.06.027>
- 982 Lee, J.-E., Fung, I., DePaolo, D. J., & Otto-Bliesner, B. (2008). Water isotopes dur-  
 983 ing the Last Glacial Maximum: New general circulation model calculations. *Jour-  
 984 nal of Geophysical Research*, *113*(D19). <https://doi.org/10.1029/2008JD009859>
- 985 Li, J., & Zwally, H. J. (2015). Response times of ice-sheet surface heights to  
 986 changes in the rate of Antarctic firn compaction caused by accumulation  
 987 and temperature variations. *Journal of Glaciology*, *61*(230), 1037–1047.  
 988 <https://doi.org/10.3189/2015JoG14J182>
- 989 Ligtenberg, S. R. M., Helsen, M. M., & Van den Broeke, M. R. (2011). An improved  
 990 semi-empirical model for the densification of Antarctic firn. *The Cryosphere*, *5*,  
 991 809–819. <https://doi.org/10.5194/tc-5-809-2011>
- 992 Lilien, D. A., Fudge, T. J., Koutnik, M. R., Conway, H., Osterberg, E. C., Fer-  
 993 ris, D. G., Stevens, C. M., et al. (2018). Holocene Ice-Flow Speedup in the  
 994 Vicinity of the South Pole. *Geophysical Research Letters*, *45*(13), 6557–6565.  
 995 <https://doi.org/10.1029/2018GL078253>
- 996 Looyenga, H. (1965). Dielectric constants of heterogeneous mixtures. *Physica*, *31*(3),  
 997 401–406. [https://doi.org/10.1016/0031-8914\(65\)90045-5](https://doi.org/10.1016/0031-8914(65)90045-5)
- 998 Lorius, C., Jouzel, J., Raynaud, D., Hansen, J., & Le Treut, H. (1990). The ice-core  
 999 record: climate sensitivity and future greenhouse warming. *Nature*, *347*(6289),  
 1000 139–145. <https://doi.org/10.1038/347139a0>
- 1001 Lundin, J. M., Stevens, C. M., Arthern, R., Buizert, C., Orsi, A., Ligtenberg, S. R.,  
 1002 Harris, P., et al. (2017). Firn Model Intercomparison Experiment (FirnMICE).  
 1003 *Journal of Glaciology*, *63*(239), 401–422. <https://doi.org/10.1017/jog.2016.114>
- 1004 Luz, B., & Barkan, E. (2010). Variations of  $^{17}\text{O}/^{16}\text{O}$  and  $^{18}\text{O}/^{16}\text{O}$  in me-  
 1005 teoritic waters. *Geochimica et Cosmochimica Acta*, *74*(22), 6276–6286.  
 1006 <https://doi.org/10.1016/j.gca.2010.08.016>
- 1007 MacAyeal, D. R. (1993). Binge/purge oscillations of the Laurentide ice sheet as a  
 1008 cause of the North Atlantic’s Heinrich events. *Paleoceanography*, *8*(6), 775–784.  
 1009 <https://doi.org/10.1029/93PA02200>
- 1010 Majoube, B. (1970). Fractionation factor of  $^{18}\text{O}$  between water vapour and ice.  
 1011 *Nature*, *226*, 1242. <https://doi.org/10.1038/2261242a0>
- 1012 Markle, B. R. (2017). *Climate dynamics revealed in ice cores: advances in tech-  
 1013 niques, theory, and interpretation* (Thesis (PH. D.) – University of Washington,  
 1014 208 pp.). <http://hdl.handle.net/1773/40391>
- 1015 Martinerie, P., Lipenkov, V. Y., Raynaud, D., Chappellaz, J., Barkov, N. I., & Lo-  
 1016 rorius, C. (1994). Air content paleo record in the Vostok ice core (Antarctica): A  
 1017 mixed record of climatic and glaciological parameters. *Journal of Geophysical  
 1018 Research*, *99*(D5), 10565. <https://doi.org/10.1029/93JD03223>
- 1019 Masson-Delmotte, V., Jouzel, J., Landais, A., Stievenard, M., Johnsen, S.J., White,  
 1020 J. W. C., Werner, M., Sveinbjornsdottir, A. and Fuhrer, K. (2005). GRIP deu-  
 1021 terium excess reveals rapid and orbital-scale changes in Greenland moisture origin.  
 1022 *Science*, *309*, 118–121. <https://doi.org/10.1126/science.1108575>
- 1023 Masson-Delmotte, V., Kageyama, M., Braconnot, P., Charbit, S., Krinner, G., Ritz,  
 1024 C., Gladstone, R. M., et al. (2006). Past and future polar amplification of cli-  
 1025 mate change: climate model intercomparisons and ice-core constraints. *Climate  
 1026 Dynamics*, *26*(5), 513–529. <https://doi.org/10.1007/s00382-005-0081-9>

- 1027 Masson-Delmotte, V., Hou, S., Ekaykin, A., Jouzel, J., Aristarain, A., Bernardo, R.  
 1028 T., Frezzotti, M., et al. (2008). A review of Antarctic surface snow isotopic com-  
 1029 position: Observations, atmospheric circulation, and isotopic modeling. *Journal of*  
 1030 *Climate*, *21*(13), 3359–3387. <https://doi.org/10.1175/2007JCLI2139.1>
- 1031 Metropolis, N., Rosenbluth, A. W., Rosenbluth, M. N., Teller, A. H., & Teller, E.  
 1032 (1953). Equation of state calculations by fast computing machines. *The Journal of*  
 1033 *Chemical Physics*, *21*(6), 1087–1092. <https://doi.org/10.1063/1.1699114>
- 1034 Monnin, E., Steig, E. J., Siegenthaler, U., Kawamura, K., Schwander, J., Stauff-  
 1035 fer, B., Morse, D. L., Stocker, T. F., Barnola, J. M., Bellier, B., Raynaud, D.,  
 1036 & Fischer, H. (2004). Evidence for substantial accumulation rate variability in  
 1037 Antarctica during the Holocene through synchronization of CO<sub>2</sub> in the Taylor  
 1038 Dome, Dome C and DML ice cores. *Earth and Planetary Science Letters*, *224*,  
 1039 45–54. <https://doi.org/10.1016/j.epsl.2004.05.007>
- 1040 Mosegaard, K., & Tarantola, A. (1995). Monte Carlo sampling of solutions to inverse  
 1041 problems. *Journal of Geophysical Research: Solid Earth*, *100*(B7), 12431–12447.  
 1042 <https://doi.org/10.1029/94JB03097>
- 1043 Mosegaard, K. (1998). Resolution analysis of general inverse problems  
 1044 through inverse Monte Carlo sampling. *Inverse Problems*, *14*(3), 405.  
 1045 <https://doi.org/10.1088/0266-5611/14/3/004>
- 1046 Mosegaard, K., & Tarantola, A. (2002). Probabilistic approach to inverse problems.  
 1047 In W. Lee, P. Jennings, C. Kisslinger, & H. Kanamori (Eds.), *International Hand-*  
 1048 *book of Earthquake & Engineering Seismology (Part A)* (237–265). Academic  
 1049 Press.
- 1050 Mosegaard, K., & Sambridge, M. (2002). Monte Carlo analysis of inverse problems.  
 1051 *Inverse problems*, *18*(3), R29. <https://doi.org/10.1088/0266-5611/18/3/201>
- 1052 Neumann, T. A., Conway, H., Price, S., Waddington, E. D., & Morse, D. L. (2008).  
 1053 Holocene accumulation and ice-sheet dynamics in central West Antarctica. *Jour-*  
 1054 *nal of Geophysical Research*, *113*, (F2). <https://doi.org/10.1029/2007JF000764>
- 1055 Nye, J. (1963). Correction factor for accumulation measured by the thickness  
 1056 of the annual layers in an ice sheet. *Journal of Glaciology*, *4*(36), 785–788.  
 1057 <https://doi.org/10.3189/S0022143000028367>
- 1058 Parrenin, F., Remy, F., Ritz, C., Siegert, M. J., & Jouzel, J. (2004). New mod-  
 1059 eling of the Vostok ice flow line and implication of the glaciological chronol-  
 1060 ogy of the Vostok ice core. *Journal of Geophysical Research*, *109*, (D20).  
 1061 <https://doi.org/10.1029/2004JD004561>
- 1062 Parrenin, F., Barker, S., Blunier, T., Chappellaz, J., Jouzel, J., Landais,  
 1063 A., Veres, D., et al. (2012). On the gas-ice depth difference ( $\Delta$ depth)  
 1064 along the EPICA Dome C ice core. *Climate of the Past*, *8*(2), 1089–1131.  
 1065 <https://doi.org/10.5194/cpd-8-1089-2012>
- 1066 Parrenin, F., Masson-Delmotte, V., Kohler, P., Raynaud, D., Paillard, D., Schwan-  
 1067 der, J., Jouzel, J., et al. (2013). Synchronous change of atmospheric CO<sub>2</sub> and  
 1068 Antarctic temperature during the last deglacial warming. *Science*, *339*(6123),  
 1069 1060–1063. <https://doi.org/10.1126/science.1226368>
- 1070 Peltier, W.R. (2004). Global glacial isostasy and the surface of the ice-age Earth:  
 1071 The ICE-5G (VM2) Model and GRACE. *Ann. Rev. Earth and Planet. Sci.*, *32*,  
 1072 111–149. <https://doi.org/10.1146/annurev.earth.32.082503.144359>
- 1073 Pollard, D., & DeConto, R. M. (2009). Modelling West Antarctic ice sheet growth  
 1074 and collapse through the past five million years. *Nature*, *458*(7236), 329–332.  
 1075 <https://doi.org/10.1038/nature07809>
- 1076 Price, P. B., Nagornov, O. V., Bay, R., Chirkin, D., He, Y., Miocinovic, P., Richards,  
 1077 A., Woschnagg, K., Koci, B., & Zagorodnov, V., (2002). Temperature profile  
 1078 for glacial ice at the South Pole: implications for life in a nearby subglacial  
 1079 Lake. *Proceedings of the National Academy of Sciences*, *99*(12), 7844–7847.  
 1080 <https://doi.org/10.1073/pnas.082238999>

- 1081 Raymond, C. (1983). Deformation in the vicinity of ice divides. *Journal of Glaciol-*  
 1082 *ogy*, 29(103), 357–373. <https://doi.org/10.3189/S0022143000030288>
- 1083 Roy, K., & Peltier, W. R. (2015). Glacial isostatic adjustment, relative sea level  
 1084 history and mantle viscosity: reconciling relative sea level model predictions for  
 1085 the US East coast with geological constraints. *Geophysical Journal International*,  
 1086 201(2), 1156–1181. <https://doi.org/10.1093/gji/ggv066>.
- 1087 Schoenemann, S. W., Steig, E. J., Ding, Q., Markle, B. R., & Schauer, A.  
 1088 J. (2014). Triple water-isotopologue record from WAIS Divide, Antarc-  
 1089 tica: Controls on glacial-interglacial changes in  $^{17}\text{O}_{\text{excess}}$  of precipita-  
 1090 tion. *Journal of Geophysical Research: Atmospheres*, 119(14), 8741–8763.  
 1091 <https://doi.org/10.1002/2014JD021770>
- 1092 Schwander, J., & Stauffer, B. (1984). Age difference between polar  
 1093 ice and the air trapped in its bubbles. *Nature*, 311(5981), 45–47.  
 1094 <https://doi.org/10.1038/311045a0>
- 1095 Schwander, J., Stauffer, B., & Sigg, A. (1988). Air mixing in firn and  
 1096 the age of the air at pore close-off. *Annals of Glaciology*, 10, 141–145.  
 1097 <https://doi.org/10.3189/S0260305500004328>
- 1098 Schwander, J. The transformation of snow to ice and the occlusion of gases, in: H.  
 1099 Oeschger, C.C. Langway Jr. (Eds.), *The Environmental Record in Glaciers and Ice*  
 1100 *Sheets*, John Wiley, New York, 1989, pp. 53–67.
- 1101 Severinghaus, J. P., Sowers, T., Brook, E. J., Alley, R. B., & Bender, M. L. (1998).  
 1102 Timing of abrupt climate change at the end of the Younger Dryas interval  
 1103 from thermally fractionated gases in polar ice. *Nature*, 391(6663), 141–146.  
 1104 <https://doi.org/10.1038/34346>
- 1105 Severinghaus, J. P., Grachev, A., & Battle, M. (2001). Thermal fractionation of  
 1106 air in polar firn by seasonal temperature gradients. *Geochemistry, Geophysics,*  
 1107 *Geosystems*, 2(7). <https://doi.org/10.1029/2000GC000146>
- 1108 Severinghaus, J. (2019) “South Pole (SPICECORE)  $^{15}\text{N}$ ,  $^{18}\text{O}$ ,  $\text{O}_2/\text{N}_2$  and  $\text{Ar}/\text{N}_2$ ”  
 1109 U.S. Antarctic Program (USAP) Data Center. <https://doi.org/10.15784/601152>.
- 1110 Sigl, M., Fudge, T. J., Winstrup, M., Cole-Dai, J., Ferris, D., McConnell, J. R., Bisi-  
 1111 aux, M., et al. (2016). The WAIS Divide deep ice core WD2014 chronology–Part  
 1112 2: Annual-layer counting (0–31 ka BP). *Climate of the Past*, 12(3), 769–786.  
 1113 <https://doi.org/10.5194/cp-12-769-2016>
- 1114 Sime, L. C., Hopcroft, P. O., & Rhodes, R. H. (2019). Impact of abrupt  
 1115 sea ice loss on Greenland water isotopes during the last glacial period.  
 1116 *Proceedings of the National Academy of Sciences*, 116(10), 4099–4104.  
 1117 <https://doi.org/10.1073/pnas.1807261116>
- 1118 Simonsen, S. B., Johnsen, S. J., Popp, T. J., Vinther, B. M., Gkinis, V., & Steen-  
 1119 Larsen, H. C. (2011). Past surface temperatures at the NorthGRIP drill site from  
 1120 the difference in firn diffusion of water isotopes. *Climate of the Past*, 7(4), 1327–  
 1121 1335. <https://doi.org/10.5194/cp-7-1327-2011>
- 1122 Simonsen, S. B., Stenseng, L., Aðalgeirsdóttir, G., Fausto, R. S., Hvidberg, C. S., &  
 1123 Lucas-Picher, P. (2013). Assessing a multilayered dynamic firn-compaction model  
 1124 for Greenland with ASIRAS radar measurements. *Journal of Glaciology*, 59(215),  
 1125 545–558. <https://doi.org/10.3189/2013JoG12J158>
- 1126 Sowers, T., Bender, M., Raynaud, D., & Korotkevich, Y. S. (1992).  $\delta^{15}\text{N}$  of  $\text{N}_2$  in air  
 1127 trapped in polar ice: A tracer of gas transport in the firn and a possible constraint  
 1128 on ice age-gas age differences. *Journal of Geophysical Research: Atmospheres*,  
 1129 97(D14), 15683–15697. <https://doi.org/10.1029/92JD01297>
- 1130 Steen-Larsen, H. C., Waddington, E. D., & Koutnik, M. R. (2010). Formulating an  
 1131 inverse problem to infer the accumulation-rate pattern from deep internal layering  
 1132 in an ice sheet using a Monte Carlo approach. *Journal of Glaciology*, 56(196),  
 1133 318–332. <https://doi.org/10.3189/002214310791968476>

- 1134 Steig, E. J., Grootes, P. M., & Stuiver, M. (1994). Seasonal pre-  
 1135 cipitation timing and ice core records. *Science*, *266*, 1885–1886.  
 1136 <https://doi.org/10.1126/science.266.5192.1885>
- 1137 Steig, E. J., Ding, Q., White, J. W. C., Küttel, M., Rupper, S. B., Neumann,  
 1138 T. A., Neff, P. D., Gallant, A. J. E., Mayewski, P. A., Taylor, K. C., Hoff-  
 1139 mann, G., Dixon, D. A., Schoenemann, S., Markle B. M., Schneider, D. P.,  
 1140 Fudge, T. J., Schauer, A. J., Teel, R. P., Vaughn, B., Burgener, L., Williams,  
 1141 J., & Korotkikh, E. (2013). Recent climate and ice-sheet change in West  
 1142 Antarctica compared to the past 2000 years. *Nature Geoscience*, *6*(5), 372.  
 1143 <https://doi.org/10.1038/ngeo1778>
- 1144 Steig, E. J., Gkinis, V., Schauer, A. J., Schoenemann, S. W., Samek, K., Hoffnagle,  
 1145 J., Tan, S. M., et al. (2014). Calibrated high-precision  $^{17}\text{O}$ -excess measurements  
 1146 using cavity ring-down spectroscopy with laser-current-tuned cavity resonance. *At-*  
 1147 *mospheric Measurement Techniques*, *7*, 2421–2435. [https://doi.org/10.5194/amt-7-](https://doi.org/10.5194/amt-7-2421-2014)  
 1148 [2421-2014](https://doi.org/10.5194/amt-7-2421-2014)
- 1149 Steig, E. J., T. R. Jones, A. J. Schauer, E. C. Kahle, V. A. Morris, B. H. Vaughan,  
 1150 L. Davidge, & White, J. W. C. (2021). Continuous-flow analysis of  $\delta^{17}\text{O}$ ,  $\delta^{18}\text{O}$ ,  
 1151 and  $\delta\text{D}$  of  $\text{H}_2\text{O}$  on an ice core from the South Pole. *Frontiers in Earth Science*, *9*,  
 1152 640292. <https://doi.org/10.3389/feart.2021.640292>
- 1153 Stevens, C. M., Verjans, V., Lundin, J., Kahle, E. C., Horlings, A. N., Horlings,  
 1154 B. I., & Waddington, E. D. (2020). The Community Firn Model (CFM) v1. 0.  
 1155 *Geoscientific Model Development*, *13*(9), 4355–4377. [https://doi.org/10.5194/gmd-](https://doi.org/10.5194/gmd-13-4355-2020)  
 1156 [13-4355-2020](https://doi.org/10.5194/gmd-13-4355-2020)
- 1157 Tarantola, A. (1987). Inverse problem theory: Methods for data fitting and model  
 1158 parameter estimation. *Elsevier Science*, Amsterdam.
- 1159 van der Wel, G., Fischer, H., Oerter, H., Meyer, H., & Meijer, H. A. J. (2015). Esti-  
 1160 mation and calibration of the water isotope differential diffusion length in ice core  
 1161 records. *The Cryosphere*, *9*(4), 1601–1616. <https://doi.org/10.5194/tc-9-1601-2015>
- 1162 Veres, D., Bazin, L., Landais, A., Toyé Mahamadou Kele, H., Lemieux-Dudon,  
 1163 B., Parrenin, F., Chappellaz, J., et al. (2013). The Antarctic ice core chronol-  
 1164 ogy (AICC2012): an optimized multi-parameter and multi-site dating ap-  
 1165 proach for the last 120 thousand years. *Climate of the Past*, *9*(4), 1733–1748.  
 1166 <https://doi.org/10.5194/cp-9-1733-2013>
- 1167 WAIS Divide Project Members (2013). Onset of deglacial warming in West  
 1168 Antarctica driven by local orbital forcing. *Nature*, *500*(7463), 440–444.  
 1169 <https://doi.org/10.1038/nature12376>
- 1170 Werner, M., Mikolajewicz, U., Heimann, M., & Hoffmann, G. (2000). Borehole ver-  
 1171 sus isotope temperatures on Greenland: Seasonality does matter. *Geophysical*  
 1172 *Research Letters*, *27*(5), 723–726. <https://doi.org/10.1029/1999GL006075>
- 1173 Werner, M., Jouzel, J., Masson-Delmotte, V., & Lohmann, G. (2018). Rec-  
 1174 onciling glacial Antarctic water stable isotopes with ice sheet topography  
 1175 and the isotopic paleothermometer. *Nature Communications*, *9*(1), 1–10.  
 1176 <https://doi.org/10.1038/s41467-018-05430-y>
- 1177 Whillans, I. M., & Grootes P. M. (1985). Isotopic diffusion in cold  
 1178 snow and firn. *Journal of Geophysical Research*, *90*(D2), 3910–3918.  
 1179 <https://doi.org/10.1029/JD090iD02p03910>
- 1180 Whitehouse, P. L., Bentley, M. J., & Le Brocq, A. M. (2012). A deglacial model for  
 1181 Antarctica: geological constraints and glaciological modelling as a basis for a new  
 1182 model of Antarctic glacial isostatic adjustment. *Quaternary Science Reviews*, *32*,  
 1183 1–24. <https://doi.org/10.1016/j.quascirev.2011.11.016>
- 1184 Winski, D. A., Fudge, T. J., Ferris, D. G., Osterberg, E. C., Fegyveresi, J. M., Cole-  
 1185 Dai, J., Buizert, C., Epifanio, J., Brook, E. J., Beaudette, R., Severinghaus, J.,  
 1186 Sowers, T., Steig, E. J., Kahle, E. C., Jones, T. R., Morris, V., Aydin, M., Nice-  
 1187 wonger, M. R., Casey, K. A., Alley, R. B., Waddington, E. D., & Iverson, N.

- 1188 A. (2019). The SP19 chronology for the South Pole Ice Core—Part 1: volcanic  
1189 matching and annual layer counting. *Climate of the Past*, 15(5), 1793–1808.  
1190 <https://doi.org/10.5194/cp-15-1793-2019>
- 1191 York, D., Evensen, N. M., Martinez, M. L., & De Basabe Delgado, J. (2004). Unified  
1192 equations for the slope, intercept, and standard errors of the best straight line.  
1193 *American Journal of Physics*, 72(3), 367–375. <https://doi.org/10.1119/1.1632486>

1 **Reconstruction of Temperature, Accumulation Rate,**  
2 **and Layer Thinning from an Ice Core at South Pole**  
3 **Using a Statistical Inverse Method**

Emma C. Kahle<sup>1</sup>, Eric J. Steig<sup>1</sup>, Tyler R. Jones<sup>2</sup>, T.J. Fudge<sup>1</sup>, Michelle R.

Koutnik<sup>1</sup>, Valerie A. Morris<sup>2</sup>, Bruce H. Vaughn<sup>2</sup>, Andrew J. Schauer<sup>1</sup>, C.

Max Stevens<sup>1</sup>, Howard Conway<sup>1</sup>, Edwin D. Waddington<sup>1</sup>, Christo Buizert<sup>3</sup>,

Jenna Epifanio<sup>3</sup>, James W. C. White<sup>2</sup>

4 <sup>1</sup>Department of Earth and Space Sciences, University of Washington, Seattle WA 98195, USA

5 <sup>2</sup>Institute of Arctic and Alpine Research, University of Colorado, Boulder CO 80309, USA

6 <sup>3</sup>College of Earth Ocean and Atmospheric Sciences, Oregon State University, Corvallis OR 97331, USA

7 **Contents of this file**

8 1. Text S1 to S5

9 2. Figures S1 to S19

---

Corresponding author: Emma C. Kahle, Department of Earth and Space Sciences, University  
of Washington, Seattle WA 98195, USA. (eckahle@uw.edu)

10 **Introduction.** This supporting information document provides further details on meth-  
11 ods used in the analysis described in the main text. We include information about:

12 S1. Diffusion-length data and modeling

13 S2. Inverse methods

14 S3. Sensitivity tests

15 S4. Ice-flow modeling

16 S5. The  $\delta^{15}\text{N}$ -based thinning function

## 17 **Text S1. Diffusion-length data and modeling**

### 18 *S1.1 Corrections to diffusion-length data*

19 We make two corrections to the estimates of diffusion length calculated from the spectra  
20 of the water-isotope data.

21 First, we correct for the effect on the water-isotope data from the continuous-flow-analysis  
22 (CFA) measurement system. As melted ice samples are transported through the tubing  
23 and reservoirs of the CFA system, some smoothing of the high-frequencies of the natural  
24 water-isotope variations occurs. This smoothing is minimized by design of the components  
25 of the CFA-system, but still impacts the measured signal. The extent of this system  
26 smoothing can be quantified by measuring the system response to a step change in isotopic  
27 value using laboratory-produced ice (Jones et al., 2017b). The system diffusion length for  
28 the CFA system used in this analysis is 0.07 cm for  $\delta^{17}\text{O}$  and  $\delta^{18}\text{O}$ , and 0.08 cm for  $\delta\text{D}$   
29 (Jones et al., 2017b).

30 Second, we correct for the additional diffusion that occurred in the solid ice below the  
31 bottom of the firn, following Gkinis et al. (2014). To calculate the solid-ice diffusion length,  
32 we assume the modern borehole temperature profile  $T(z)$  remains constant through time  
33 to find the diffusivity profile  $D_{ice}(z)$ , following Gkinis et al. (2014):

$$D_{ice}(z) = 9.2 \times 10^{-4} \times \exp\left(\frac{-7186}{T(z)}\right), \quad (1)$$

34 with  $T(z)$  given in K and  $D_{ice}(z)$  given in  $\text{m}^2 \text{s}^{-1}$ . For  $T(z)$  at SPC14, we use borehole  
35 temperature measurements from the nearby neutrino observatory (Price et al., 2002).

36 The solid-ice diffusion length is also affected by vertical strain in the ice sheet. We assume  
 37 a simple thinning function from a 1-D ice-flow model (Dansgaard and Johnsen, 1969) with  
 38 a kink-height  $h_0 = 0.2$  for this calculation. We describe the total thinning experienced by  
 39 a layer  $S(t)$  in a given time interval  $t = 0$  to  $t = t'$  as:

$$S(t') = \exp\left(\int_0^{t'} \dot{\epsilon}_z(t) dt\right), \quad (2)$$

40 where  $\dot{\epsilon}_z(t)$  is the vertical strain rate calculated from the thinning function. The solid-ice  
 41 diffusion length,  $\sigma_{ice}$ , is then calculated as (Gkinis et al., 2014):

$$\sigma_{ice}^2(t') = S(t')^2 \int_0^{t'} 2D_{ice}(t)S(t)^{-2} dt. \quad (3)$$

42 To produce the corrected diffusion-length data set used in this analysis, we subtract in  
 43 quadrature both the system diffusion length,  $\sigma_{CFA}$ , and the solid-ice diffusion length,  
 44  $\sigma_{solid}$ , from the total measured diffusion length,  $\sigma_{meas}$ :

$$\sigma^2 = \sigma_{meas}^2 - \sigma_{CFA}^2 - \sigma_{solid}^2. \quad (4)$$

45 The diffusion length  $\sigma$  represents the diffusion that occurred within the firn column and  
 46 that has experienced the effects of vertical strain in the ice sheet (*i.e.*,  $\sigma = S(z)\sigma_{firn}$ ).  
 47 Figure S1 shows the effect of these corrections on the estimated diffusion length.

### 48 *S1.2 Modeling firn diffusion length*

49 Within the forward model of the inverse problem, we model diffusion length in the firn  
 50 column. We use the following values in calculating the diffusivity coefficients,  $D_x$ , for each  
 51 water-isotope ratio:

$$D_{\delta^{18}O}^{air} = \frac{D^{air}}{1.0285} \quad (\text{Johnsen et al., 2000}) \quad (5)$$

$$D_{\delta^{17}O}^{air} = \frac{D^{air}}{1.01466} \quad (\text{Luz and Barkan, 2010}) \quad (6)$$

$$D_{\delta D}^{air} = \frac{D^{air}}{1.0251} \quad (\text{Johnsen et al., 2000}) \quad (7)$$

52 where:

$$D^{air} = 0.211 \times 10^{-4} \times \left( \frac{T}{273.15} \right)^{1.94} \times \frac{P_0}{P} \quad (\text{Johnsen et al., 2000}) \quad (8)$$

53 is the diffusivity of water vapor in air.  $T$  is temperature given in Kelvin and  $P$  is the  
54 atmospheric pressure compared to a reference pressure of  $P_0 = 1$  atm.

55 We use the following values in calculating the fractionation factors,  $\alpha_x$ , for each water-  
56 isotope ratio, for the equilibrium of water vapor over ice:

$$\alpha_{18} = \exp\left(\frac{11.839}{T} - 28.224 \times 10^{-3}\right) \quad (\text{Majoube, 1970}) \quad (9)$$

$$\alpha_{17} = \exp(0.529 \times \log(\alpha_{18})) \quad (\text{Barkan and Luz, 2007}) \quad (10)$$

$$\alpha_D = \exp\left(-0.0559 + \frac{13525}{T^2}\right) \quad (\text{Lamb et al., 2017}) \quad (11)$$

57 The tortuosity parameter  $\tau$  used in Equation 5 in the main text is given by (Schwander  
58 et al., 1988; Johnsen et al., 2000):

$$\frac{1}{\tau} = \begin{cases} 1 - b \times \left( \frac{\rho}{\rho_{ice}} \right)^2 & , \text{ for } \rho \leq \frac{\rho_{ice}}{\sqrt{b}} \\ 0 & , \text{ for } \rho > \frac{\rho_{ice}}{\sqrt{b}} \end{cases} \quad (12)$$

59 using a tortuosity parameter  $b = 1.3$ .

The solution to Equation 4 in the main text for the isotope profile at a given depth  $z$  and time  $t$  is given by:

$$\delta(z, t) = S(t) \frac{1}{\sigma\sqrt{2\pi}} \int_{-\infty}^{\infty} \delta(z, 0) \exp\left(\frac{-(z-u)^2}{2\sigma^2}\right) du, \quad (13)$$

60 as described in (Gkinis et al., 2014) and fully derived in Kahle et al. (2020), where  $\sigma$  is  
 61 the diffusion length and the factor  $S(t)$  is the total thinning a layer has experienced due  
 62 to ice flow, as described in Equation 2 of this supplement.

### 63 **Text S2. Inverse methods**

64 The statistical inverse method used in this work relates the three variables that span the  
 65 model space with the three data variables that span the data space. We define the model  
 66 space as a vector space with a dimension for each of the unknown input parameters; a  
 67 particular point in the model space represents a specific set of input parameters  $m$ . The  
 68 data space is defined similarly, where each data parameter in  $d$  represents a dimension,  
 69 and our observations  $d_{obs}$  exist at a particular point in the data space. Because the data  
 70 have measurement uncertainties, the “true” values in the data space may differ from  $d_{obs}$ .  
 71 Because we have three model parameters across 208 depth points (624 total unknown  
 72 parameters), our problem spans a high dimensional model space, and an exhaustive search  
 73 of all possible solutions  $m$  is not practical. We limit the number of instances of  $m$  to  
 74 evaluate by using an importance-sampling algorithm. We use a Markov Chain Monte  
 75 Carlo algorithm to combine *a priori* information about which solutions  $m$  are plausible  
 76 for realistic ice-sheet conditions and information from our data sets. This algorithm  
 77 efficiently explores the parameter space by favoring instances of  $m$  that are similar to  
 78 those that have already produced good fits with the observations  $d_{obs}$ .

79 In this section, we describe the theoretical framework (S2.1 and S2.2) and the practical  
 80 implementation (S2.3) of the inverse approach we use. In general, the solution of this type  
 81 of inverse problem depends on the formulation of the problem, including what information  
 82 is included in the constraints and how the output is analyzed. We detail below each of  
 83 the choices that we make in our approach.

### 84 *S2.1 Bayesian framework*

85 We use a statistical Bayesian framework to solve this inverse problem. Rather than seek a  
 86 single best-fit solution, we consider the likelihood of different solutions based on probabil-  
 87 ity distributions within the parameter spaces of the data and the model. This framework  
 88 combines *a priori* model parameter information with data measurement uncertainties.  
 89 Unlike a regularization approach, such as Tikhonov regularization, a Bayesian approach  
 90 does not require a subjective choice about how well the final set of solutions should fit  
 91 the data (Tarantola, 1987; Steen-Larsen et al., 2010).

92 We characterize the *a priori* information describing the model inputs  $m$  as a probability  
 93 distribution in the model space. This distribution, denoted as  $\rho_m(m)$ , represents the  
 94 likelihood of solutions  $m$  based on data-independent prior knowledge about what values  
 95 are realistic for that particular parameter (Mosegaard and Tarantola, 1995; Mosegaard  
 96 & Sambridge, 2002). To produce the complete solution to the problem, the *a priori*  
 97 information is combined with the likelihood function, which describes how well the output  
 98  $d$  from a given solution  $G(m)$  matches our observations  $d_{obs}$ . The likelihood function  $L(m)$   
 99 is defined as (Mosegaard and Tarantola, 1995):

$$L(m) = C_L \exp(-M(m)), \tag{14}$$

100 where  $C_L$  is a normalization constant and  $M(m)$  is a misfit function that measures the  
 101 deviation between  $d$  and  $d_{obs}$  in the data space.

102 The likelihood function  $L(m)$  is combined with the *a priori* distribution  $\rho_m(m)$  to define  
 103 the *a posteriori* distribution  $f(m)$  (Tarantola, 1987):

$$f(m) = C_f L(m) \rho_m(m). \quad (15)$$

104 Note that in our implementation, detailed in S2.3, we directly incorporate *a priori* in-  
 105 formation into the model space bounds and thus directly compare values of the misfit  
 106 function  $M(m)$  calculated for each solution  $m$ . Specific values for  $C_L$ ,  $C_f$ , and  $\rho_m$  are not  
 107 required.

108 The *a posteriori* distribution  $f(m)$  contains all the information we have to constrain  
 109 the inverse problem and thus represents its complete solution. The region of maximum  
 110 values of  $f(m)$  denote the most likely solutions to the problem. This distribution may be  
 111 Gaussian-like and simple to interpret, or may be multi-modal and require a more complex  
 112 interpretation. We cannot produce this *a posteriori* distribution analytically, but we can  
 113 sample its values at discrete points. For each solution  $m$  that we test in our forward model  
 114  $G$ , we calculate a discrete value of  $f(m)$ .

### 115 *S2.2 Sampling strategy*

116 Our sampling strategy uses an algorithm to determine which solutions  $m$  to test, with  
 117 the goal of producing  $f(m)$  after sufficient iterations (Mosegaard and Tarantola, 1995).  
 118 The algorithm explores the model space by randomly stepping from one solution  $m_i$  to  
 119 a neighbor  $m_j$ . In each iteration, the algorithm follows two stages, designed such that it  
 120 asymptotically produces  $f(m)$  (Mosegaard, 1998; Mosegaard & Sambridge, 2002).

121 First, an exploration stage defines how the algorithm selects a proposal for  $m_j$  given its  
 122 starting place at  $m_i$ . The selection depends on how far in model space the algorithm  
 123 is allowed to step in a single iteration. While the magnitude and direction of the step  
 124 are determined randomly, the magnitude is scaled by a base step-size. The choice of  
 125 base step-size balances the exploration of more of the model space (larger steps) with the  
 126 exploration of regions that result in high values of  $f(m)$  (smaller steps). In practice, we  
 127 must tune the step size in order to strike this balance (*e.g.*, Steen-Larsen et al. (2010)).

128 Second, an exploitation stage defines the transition probability that the proposed step  
 129 will be accepted. If the proposed step is rejected, the current solution  $m_i$  is repeated for  
 130 an additional iteration. The simplest choice for the transition probability is the Metropo-  
 131 lis acceptance probability (Metropolis et al., 1953; Mosegaard, 1998; Mosegaard & Sam-  
 132 bridge, 2002):

$$p_{\text{accept}} = \min \left( 1, \frac{f(m_j)}{f(m_i)} \right). \quad (16)$$

133 This formulation will always accept the proposed step to  $m_j$  if the *a posteriori* distribution  
 134 is greater at that point ( $f(m_j) > f(m_i)$ ), but may still accept the proposed step even if  
 135 the *a posteriori* distribution is smaller at that point ( $f(m_j) < f(m_i)$ ) by a probability  
 136 proportional to  $\frac{f(m_j)}{f(m_i)}$ . This design prevents the algorithm from getting stuck at a local  
 137 maximum of  $f(m)$ , while still favoring samples from regions of the model space with a  
 138 relatively high value of  $f(m)$ .

139 After sufficient iterations, the sampling of this algorithm will converge on  $f(m)$ . The  
 140 number of iterations required for convergence, the convergence time, depends on the base  
 141 step-size chosen. Step size is tuned to minimize the number of iterations required while

142 appropriately sampling the model space. Related to the convergence time is the burn-in  
143 time, which refers to the number of iterations completed before the sampled values of  
144  $f(m)$  become relatively stationary. After this point, the algorithm continues to sample  
145 only highly likely solutions  $m$ . Prior work has found that after the burn-in time, the  
146 acceptance rate of the algorithm should be 25-50% (Gelman et al., 1996) in order to strike  
147 a balance between exploration (bigger steps) and efficiency (smaller steps).

### 148 *S2.3 Implementation of sampling*

149 To sample and estimate the *a posteriori* distribution, we implement the theory described  
150 above. We initiate the problem with our initial guess  $m_1$  for each parameter and begin  
151 evaluating successive solutions from that point. Our sampling strategy uses Equation 16  
152 and the associated ideas about sampling efficiency.

153 In the exploration stage of the algorithm, rather than perturb only one parameter within  
154  $m_i$  at a time, all 624 parameters (*i.e.*, values at each depth point for temperature, ac-  
155 cumulation rate, and thinning function) are perturbed in each iteration. This design  
156 improves the efficiency of the algorithm. Each perturbation is constructed with the same  
157 low-frequency, red-noise slope in its power spectral density as that of a comparison data  
158 set. The comparison data set for temperature is the water-isotope record, for accumu-  
159 lation rate is a destrained version of the annual-layer thicknesses, and for the thinning  
160 function is a DJ-model output. Because in reality we expect temperature, accumulation  
161 rate, and thinning to vary smoothly through time, each proposed perturbation must vary  
162 smoothly as well. Furthermore, the  $\Delta$ age and diffusion-length data sets are inherently  
163 smooth because they integrate information over the depth of the firn column. To pre-

164 vent spurious high-frequency noise from being introduced into the proposed solution  $m$ ,  
 165 we apply a low-pass filter to the perturbation. To the temperature and accumulation-  
 166 rate perturbations, we apply a lowpass filter at a 3000-year period, which corresponds  
 167 to the maximum value of  $\Delta\text{age}$ . We apply a lowpass filter at a 10,000-year period to  
 168 the thinning-function perturbations because we expect the thinning function to be even  
 169 smoother. The perturbations are then added to the previous accepted solution to generate  
 170 the next proposed solution.

171 In the exploitation stage, the algorithm determines whether to accept the proposed solu-  
 172 tion  $m_{i+1}$  by calculating and comparing the values of the *a posteriori* distribution at  $m_i$   
 173 and  $m_{i+1}$ . Equation 15 describes how the *a posteriori* distribution is calculated from the  
 174 likelihood function  $L(m)$  and the *a priori* distribution  $\rho(m)$ . Because we have already in-  
 175 corporated our prior knowledge directly into the model space bounds, we simply compare  
 176 the value of the likelihood function evaluated at  $m_i$  and  $m_{i+1}$  (Mosegaard, 1998):

$$p_{\text{accept}} = \min \left( 1, \frac{L(m_{i+1})}{L(m_i)} \right). \quad (17)$$

177 We define the likelihood function, as in Equation 14, with a misfit function  $M(m)$  defined  
 178 as (Khan et al., 2000; Mosegaard & Sambridge, 2002):

$$M(m) = \sum_n \frac{|d^{(n)}(m) - d_{\text{obs}}^{(n)}|}{\sigma_n}, \quad (18)$$

179 where  $d^{(n)}(m)$  denotes the modeled output,  $d_{\text{obs}}^{(n)}$  the observation, and  $\sigma_n$  the standard de-  
 180 viation of the observation for the  $n$ th datum. This misfit function minimizes the influence  
 181 of outliers, compared to a root-mean-square formulation.

182 We run the algorithm until we have 100,000 accepted samples of the *a posteriori* distribu-  
 183 tion. With an acceptance rate of 30-40%, this requires approximately 300,000 iterations

184 in total. The burn-in time is reached after approximately 10,000 iterations, and we con-  
185 sider solutions  $m$  only after this point. We repeat this process five times to account for  
186 any persistent impacts from early perturbations, combining all accepted solutions after  
187 the burn-in time to create the final set of results. Because only a small perturbation is  
188 made between iterations, successive iterations are correlated. Analysis of the *a posteriori*  
189 distribution requires a collection of statistically independent models, so we consider only  
190 a subset of all accepted models (Mosegaard, 1998; Dahl-Jensen et al., 1998). Through an  
191 autocorrelation analysis of the accepted models, we conclude that saving every 300th solu-  
192 tion produces a statistically independent set. Out of a total of 500,000 accepted solutions,  
193 1500 solutions are included in our analysis of the *a posteriori* distribution.

### 194 **Text S3. Sensitivity tests**

#### 195 *S3.1 Sensitivity to Firn Model*

196 To evaluate the sensitivity of the results to the choice of firn model, we perform two  
197 sets of experiments comparing different firn models. First, we use the Community Firn  
198 Model (CFM) (Stevens et al., 2020; Gkinis et al., 2021) to calculate  $\Delta\text{age}$  using our full  
199 ensemble of accumulation-rate and temperature reconstructions as inputs for five different  
200 models: a dynamic version of Herron-Langway, Goujon et al. (2003), Li and Zwally (2015),  
201 Ligtenberg et al. (2011), and Simonsen et al. (2013). (Solving the full inverse problem  
202 with any of these dynamic models, which do not have analytical solutions, is impractical,  
203 but we address this issue in the second set of experiments below.) Comparison of the  
204 outputs of the five different models and the  $\Delta\text{age}$  data is given in Figure S2. The results  
205 show that while the Ligtenberg et al. (2011) and Li and Zwally (2015) models produce

206 similar results for the glacial period, the Goujon et al. (2003) and Simonsen et al. (2013)  
207 models systematically underestimate  $\Delta\text{age}$  by about 500 years. As currently formulated,  
208 none of these models other than Herron-Langway are consistent with the modern depth-  
209 density profiles at South Pole. Because the accumulation rate and thinning function are  
210 tightly constrained by the diffusion-length and layer-thickness data, the only available  
211 free parameter that could be used to reconcile these other models with the empirical  
212  $\Delta\text{age}$  data is temperature. For the Goujon et al. (2003) model, for example, adjusting  
213 the temperature to match  $\Delta\text{age}$  requires reducing the temperature by about  $2^\circ\text{C}$  in the  
214 glacial and by  $> 3^\circ\text{C}$  in the Holocene; the latter is implausible and would require an even  
215 smaller glacial-interglacial temperature change than our reconstruction indicates. Thus,  
216 our choice of Herron-Langway is motivated by the fact that it produces results most  
217 consistent with multiple, independent, empirical constraints.

218 In a second set of experiments, we further examine the sensitivity of our results to the  
219 choice of firn model by implementing two of the models, Goujon et al. (2003) (GOU) and  
220 Ligtenberg et al. (2011) (LIG), within our inverse model framework. These two models are  
221 representative end-members (Figure S2). We use the CFM to run these models to steady  
222 state using a range of temperature and accumulation-rate pairs that span the climate of  
223 the SPC14 record. We save the model output in a format that is accessible from within  
224 the inverse procedure, allowing the appropriate firn age-depth-density profile to be used  
225 for the corresponding temperature and accumulation-rate value in each iteration.

226 Figure S3 shows the results of these experiments compared with the main result using the  
227 Herron-Langway analytic model (HLA). Both the GOU and LIG firn models produce lower  
228 temperatures throughout the record, lower accumulation-rate values in the Holocene, and

229 slightly higher thinning function values through the Holocene and glacial transition, com-  
230 pared to the main HLA result. Although the Last Glacial Maximum (LGM) temperature  
231 in the GOU and LIG results is lower than that of the HLA result, the glacial-interglacial  
232 temperature change is similar for all three models, as shown in Figure S4. This shows  
233 that the relatively small glacial-interglacial change, one of the key results in this paper, is  
234 not a consequence of our model choice. Building on the result of the first set of firn-model  
235 experiments, it also further demonstrates that the HLA model is an appropriate model  
236 for South Pole.

### 237 *S3.2 Sensitivity to Measured Data Sets*

238 To determine the extent to which each of our three data sets affects the results, we  
239 tested our approach by excluding different combinations of the data sets. We used the  
240 same inverse framework as before, but took into account only how well the output  $d$   
241 matches the data observations  $d_{obs}$  for the data sets included in that test. Excluding all  
242 data sets evaluates the effect of the perturbation construction by resampling the *a priori*  
243 distribution (Mosegaard and Tarantola, 2002). Figure S5 illustrates that this null test, in  
244 which there are *no* constraints from the data, successfully recovers the prior; the mean  
245 of the *a priori* distribution is approximately the mean of the bounded model space. This  
246 result shows that no spurious information is produced by the sampling procedure.

247 Building up from the null test, we tested two suites of three runs each to evaluate the  
248 sensitivity of results to each of the data sets. The first suite includes only one data set  
249 at a time, and the second suite includes two data sets at a time. The results from both  
250 suites are similar, and we show here only the results from the second. Figure S6 shows

251 the mean solution from each run of the second suite: excluding  $\Delta$ age (purple), excluding  
252 diffusion length (blue), and excluding layer thickness (green), compared alongside the  
253 full results including all parameters (black). The right three panels show the effect on  
254 the fit of the data parameters, producing, as expected, the worst fit to each data set  
255 when that information is excluded from the problem. The left three panels of Figure S6  
256 show how the exclusion of each data set impacts the mean of each set of solutions. The  
257 result for the thinning function suggests that, from 40 - 54 ka, the diffusion-length record  
258 pulls the thinning function to greater values (less thinning), while the layer thickness  
259 pulls the thinning function to smaller values (more thinning). The accumulation-rate  
260 reconstruction is most sensitive to diffusion length and layer thickness. To assess the  
261 sensitivity of the temperature reconstruction, we ran our two suites of sensitivity tests  
262 again, this time prescribing accumulation rate to the mean solution. Figure S7 shows the  
263 results for temperature for each of the four types of tests. The results suggest that  $\Delta$ age  
264 is most important for temperature at ages younger than 35 ka. At ages older than 35 ka,  
265 no single data set is most important for temperature, but the results of the 2-parameter  
266 suite suggest that the combined information from diffusion length and layer thickness has  
267 the greatest impact on the temperature result.

268 Additionally, we tested the impact of the diffusion-length data set on the temperature re-  
269 sult by isolating the temperature-dependence of the water-isotope diffusion model within  
270 the forward model. We used a linear step-change input for temperature within the diffu-  
271 sion model (solid magenta line in temperature panel of Figure S8), not allowing changes  
272 of temperature in each iteration to influence the misfit of the modeled diffusion lengths to  
273 the data set. These results (blue shading in Figure S8) show a significant difference in the

274 results for all three variables (temperature, accumulation rate, and thinning function),  
275 particularly during the LGM. This occurs because the fixed temperature we use for the  
276 diffusivity increases the modeled firn diffusion length, requiring more thinning to match  
277 the diffusion-length data. To accommodate the increased thinning, accumulation rate  
278 must increase to match the layer-thickness data. To compensate for a higher accumula-  
279 tion rate, a colder temperature is required to match the  $\Delta\text{age}$  data. In this particular  
280 example, the glacial-interglacial temperature change is reduced by  $1.4^\circ\text{C}$  from the main  
281 results, a significant difference. Setting a constant diffusion temperature colder than the  
282 main result would have the opposite effect. This sensitivity test demonstrates that the  
283 water-isotope diffusion model provides a critical constraint on temperature, comparable  
284 in significance to  $\Delta\text{age}$ .

### 285 *S3.3 Sensitivity to $\delta^{15}\text{N}$ data*

286 As detailed in Section 5.4 of the main text, we use the  $\delta^{15}\text{N}$ -based diffusive column height  
287 (DCH) to assess the impact of the  $\delta^{15}\text{N}$  data on our main result. We run a global search  
288 algorithm over a range of temperature and accumulation-rate values to find those that are  
289 in agreement with the  $\delta^{15}\text{N}$ -based DCH. The temperature and accumulation-rate values  
290 included in our global search are defined by a small range about the corresponding mean  
291 values in the main reconstruction. For temperature values, we define the range as  $\pm 5^\circ\text{C}$ ,  
292 and for accumulation-rate values, we define the range as  $\pm 0.01 \text{ m a}^{-1}$ . Given the variability  
293 in each parameter, the temperature range is relatively larger than the accumulation-rate  
294 range, which is appropriate since the accumulation rate is fairly well constrained.

295 Accompanying Figure 5 in the main text, Figure S9 shows the DCH as calculated with  
296 the accumulation-rate and temperature results shown in Figure 5. The red shading,  
297 corresponding to the red shading in Figure 5, shows the DCH calculated when the  $\delta^{15}\text{N}$   
298 constraint is applied to the accumulation rate and temperature solutions. The red shading  
299 exactly spans the uncertainty of the  $\delta^{15}\text{N}$ -based DCH, demonstrating that the solutions  
300 shown in Figure 5 are consistent with the  $\delta^{15}\text{N}$  data. A change in the global search ranges  
301 of temperature and accumulation-rate has a minor effect on the width of the red shading,  
302 but no impact on the mean values. We note that the equivalent representation of the blue  
303 shading from Figure 5 in Figure S9 is identical to that of the red shading.

304 As noted in the main text, these results show that the Herron-Langway firn model (and all  
305 other firn models we examined) cannot simultaneously accommodate all data constraints  
306 at all depths. We emphasize that while  $\delta^{15}\text{N}$  tightly constrains the DCH,  $\delta^{15}\text{N}$  does not  
307 depend on the details of the depth-density profile, nor on the amount of time represented  
308 by the DCH, and therefore cannot constrain either of these variables independently. In  
309 contrast,  $\Delta\text{age}$  is a measure of the firn densification time, and water-isotope diffusion  
310 length depends on both the densification time and the depth-density structure. Within  
311 the firn-model framework, warmer temperatures than our main reconstruction permit  
312 agreement with  $\delta^{15}\text{N}$ , but reduce agreement with diffusion-length constraints. We consider  
313 our reconstruction conservative with respect to the key result of a relatively warm last  
314 glacial maximum. We suggest that water-isotope diffusion-length data, such as we present  
315 in this paper, should be used to a greater extent in developing further refinements to firn  
316 models in the future (Gkinis et al., 2021).

### 317 *S3.4 Sensitivity of Isotope-Temperature Relationship*

318 In Section 6.2 of the main text, we show that the  $\delta^{18}\text{O}$ -temperature relationship indicated  
319 by our reconstruction, based on the HL firn model, is  $0.99\text{‰}\text{C}^{-1}$ . Table S1 shows results of  
320 the same calculation for the sensitivity tests using other firn models (Figure S3), and from  
321 the  $\delta^{15}\text{N}$  and  $\Delta\text{age}$  constraints (main text Figure 5). We also report the correlation coef-  
322 ficient  $r$  between the  $\delta^{18}\text{O}$  record and each temperature reconstruction. All  $\partial(\delta^{18}\text{O})/\partial T$   
323 slopes are significantly greater than the modern surface slope of  $0.8\text{‰}\text{C}^{-1}$ . While all  
324 correlations are significant, the maximum correlation is for the main reconstruction.

#### 325 **Text S4. Ice-flow modeling**

326 We use a 2.5-D flowband ice-flow model to estimate a thinning function for SPC14 to  
327 compare with the primary thinning function reconstruction described in the main text.  
328 As described in the main text, the primary thinning reconstruction contains more high-  
329 frequency variation than a 1-D Dansgaard-Johnsen model output. For emphasis, Fig-  
330 ure S10 shows this comparison in the depth domain to highlight the main discrepancies  
331 in the estimates, particularly from 200 to 500 m depth and from 1400 to 1750 m depth.  
332 This ice-flow-model thinning function is constrained by data for ages younger than 10 ka,  
333 producing an independent data-based estimate of ice thinning. Beyond 10 ka, we do not  
334 have sufficient knowledge of past ice flow direction and the associated bed topography  
335 along that flow path in order to fully constrain the model. For the older ice, the goal  
336 with the ice-flow-model thinning function is to determine if the structure in the primary  
337 thinning function is physically plausible. To this end, our flowband modeling suggests  
338 that variations in the primary thinning function can indeed be explained by observed  
339 variations in bedrock topography.

#### 340 *S4.1 Flowband model*

341 The flowband model was developed to calculate the time-dependent ice-surface evolution  
342 and velocity distribution along a flowline in the ice-sheet interior. The model has been  
343 described in Koutnik et al. (2016) where it was applied near the WAIS Divide ice-core  
344 site. The model calculates the ice-flow field using the Shallow Ice Approximation, which  
345 is appropriate for relatively slow-flowing interior ice that is not beneath an ice divide.  
346 Necessary boundary conditions and initial inputs to the model include the accumulation  
347 rate (Figure S11A), bed topography (Figure S11C), and ice temperature along the flowline,  
348 as well as the ice flux and ice-sheet thickness at one location.

349 The flow field described by the model is defined within a flowband domain extending  
350 200 km along the flow line. The downstream edge of the domain is located 10 km from  
351 the SPC14 site; the upstream edge marks the location of the ice divide, 190 km upstream  
352 of the SPC4 site. The width of the flowband domain (Figure S11B) is a tunable parameter  
353 and is determined such that the model matches the measured surface velocities and surface  
354 elevations described below (Text S4.2). The ice flux and ice-surface elevation are specified  
355 at one point in the domain, which we chose to be near to the drill site.

356 For this work, we calculate a steady-state flow field, rather than consider the transient  
357 response to time-varying forcing. A steady-state model is justified for three main reasons.  
358 First, the steady-state model provides a good fit to the observed depth-age relationship  
359 for the Holocene (Figure S12), where the flowline location and corresponding bed topog-  
360 raphy are well defined. The steady-state model also compares well with the ice advection  
361 estimated by Lilien et al. (2018) (Figure S13), which included a  $\sim 15\%$  speed up of sur-

362 face ice over the last 10 ka. Second, temporal variations in the accumulation rate have  
363 little impact on the cumulative thinning as a function of depth (*e.g.*, Nye, 1963). We  
364 calculate the thinning as a function of depth and then convert to a function of age based  
365 on the SP19 timescale (Winski et al., 2019). Third, while accumulation-rate variations  
366 and other changes to the boundary conditions affect ice-particle-path trajectories, these  
367 inputs require knowledge of the flowline and bed topography, which are poorly known  
368 beyond 65 km upstream from SPC14. Without specification of where the ice flowed, we  
369 cannot determine these time-variable inputs, and a time-dependent model has limited  
370 value. Additionally, we find that a steady-state model satisfies our goal of evaluating the  
371 physical plausibility of the primary thinning function reconstruction.

#### 372 *S4.2 Model Inputs*

373 *Velocity, elevation, spatial pattern of accumulation rate, and flowline determination:* Mea-  
374 surements of the surface velocity, surface elevation, and the determination of the flowline  
375 from these measurements are described in Lilien et al. (2018), with data available from  
376 the United States Antarctic Program Data Center (USAP-DC) at: [https://www.usap-  
377 dc.org/view/project/p0000200](https://www.usap-dc.org/view/project/p0000200). The surface velocity was measured at a network of stakes  
378 with 12.5 km spacing along the lines of longitude every 10° from 110° E to 180° E and  
379 out to a distance of 100 km from SPC14. The modern surface velocities were used to  
380 determine the modern flowline. The accumulation-rate pattern along the flowline (Figure  
381 S11A) was inferred using traced layers imaged with a 200 MHz radar. By comparing the  
382 measured layer thickness in SPC14 to the expected layer thickness due to advection of  
383 the upstream accumulation-rate pattern, the flowline was confidently determined for a

384 distance of 65 km upstream of SPC14, spanning the past 10.1 ka (Lilien et al., 2018). For  
385 ice older than 10 ka, we are uncertain what path the ice took.

386 *Bedrock topography:* The bed topography along the domain of the flowline (from SPC14  
387 to the ice divide) is a necessary model input, and can be grouped into three sections  
388 based on the data available (Figure S11C). 1) From 0 to 65 km upstream of SPC14,  
389 we are confident that the ice flowed over the bedrock topography imaged with radar  
390 along the modern flowline. 2) For 65 km to 100 km upstream from SPC14, we use the  
391 bedrock topography measured along the modern flowline; however, we cannot be sure  
392 that ice reaching the SPC14 site flowed along this path. 3) From 100 km to a divide at  
393 approximately 190 km upstream, we have no information about the modern flowline, nor  
394 do we know the bed topography. However, we can obtain a plausible example of the bed  
395 topography from an airborne radar survey in this region.

396 For the first and second sections, the bedrock topography along 100 km of the modern flow-  
397 line upstream of SPC14 was imaged with a ground-based, bistatic impulse radar with cen-  
398 ter frequency of 7 MHz (Figure S14). The radar system has been used widely in Antarctica  
399 (Gades et al., 2000; Neumann et al., 2008; Catania et al., 2010). The radar data and bed  
400 picks are posted at the USAP-DC at: <https://www.usap-dc.org/view/project/p0000200>.

401 For the third section, to provide additional information about the spatial variability in the  
402 bed topography beyond 100 km, we use the PolarGAP airborne radar survey (Forsberg  
403 et al., 2017). Although PolarGAP data were collected along 135° E and 142.5° E (Figure  
404 S14), the data are publicly available as a gridded product. We interpolate the gridded  
405 data to extract the bed topography along the two flight lines. The bed topography along

our flowline and the two PolarGAP lines are shown in Figure S15. The three profiles track together well until about 70 km upstream of SPC14 where they diverge as the spacing between the lines increases. To obtain a model input for bed topography that produces thinning variations similar to the primary thinning function (recall that our goal is to evaluate whether these variations are physically plausible), we combine information from the two PolarGAP lines. We connect two points (green circles in Figures S15 and S16) that yield a flowline over a high in the bed topography. The orientation of this flowline is nearly perpendicular to the modern flowline, so the ice is unlikely to have flowed over it; however, this example illustrates that the magnitude of topographic variation required to match the structure of the primary thinning function does exist in the region.

*Ice temperature:* An ice-temperature profile is specified using a 1-D thermal model fit to the measurements from the AMANDA and IceCube projects (Price et al., 2002), forced to reach the pressure melting point at the bed. This temperature profile is held constant in time and is scaled linearly as a function of ice thickness along the flowline to estimate the full temperature field in our model domain.

*Basal melt rate:* We test two choices for basal melt rate to gain insight into the sensitivity of the thinning result to this parameter. With all other parameters taken to be the same, one case has no basal melt and one case has  $1 \text{ cm a}^{-1}$  of basal melt across the whole domain. A  $1 \text{ cm a}^{-1}$  melt rate is similar to the value inferred by Jordan et al. (2018) farther upstream of SPC14. The difference between the resulting thinning functions increases with depth, but differs by only 17% during the last 10,000 years of the core. For simplicity, we plot only the non-basal melt result in Figure 6 of the main text.

### 428 *S4.3 Tuning the model*

429 The flux out the downstream edge of the domain was specified to obtain a velocity of  
430  $10 \text{ m a}^{-1}$  to match modern observations (Lilien et al., 2018). To approximately match the  
431 velocities measured at 12.5 km intervals out to a farthest distance of 100 km upstream  
432 (Figure S11E), the width of the flowband was increased with distance upstream (Fig-  
433 ure S11B). This represents convergent flow, as indicated for this region from the surface  
434 topography. The velocity measurements (Lilien et al., 2018) are not precise enough to al-  
435 low reliable convergence estimates, and we therefore assumed a linear change in flowband  
436 width for 100 km upstream. Beyond 100 km upstream, the flowband width continues  
437 to increase, at a different rate, such that the divide position is approximately 190 km  
438 upstream at an elevation of 3075 m, consistent with a likely ice origin at Titan Dome  
439 (Fudge et al., 2020).

### 440 *S4.4 Comparison with measured layers*

441 The modeled layers are shown in comparison to 7 internal layers imaged by radar (Figure  
442 S17). There is a good fit at the core site, which is also reflected in Figure S12, comparing  
443 the modeled depth-age profile and the measured data from SP19. The match to the radar  
444 layers is not nearly as good upstream where the amplitude of the modeled layers at the  
445 bedrock bump is less than what is observed in the measured layers. The discrepancy may  
446 be related to the greater uncertainty in the flowband model inputs farther upstream from  
447 SPC14.

### 448 *S4.5 Ice-flow-model thinning function*

449 The ice-flow-model thinning function (Figure 6 in main text) is calculated from the mod-  
450 eled layer thickness at the core site divided by the original thickness (the accumulation  
451 rate) when that ice was deposited at the surface. The numerical calculation can become  
452 noisy due to the finite model mesh and the difficulty of establishing the accumulation rate  
453 at the point of origin given variations in the surface accumulation pattern. Therefore,  
454 we smooth the thinning function with a moving average over a depth interval of 50 m.  
455 The jaggedness of the thinning function is the most noticeable in the deepest layers where  
456 there are smaller depth differences for the same age interval. Because we have used a  
457 steady-state model, the modeled age for a given depth is too young for ages prior to the  
458 Holocene (since we do not account for the lower accumulation rates of the glacial pe-  
459 riod). Because the cumulative thinning as a function of depth is insensitive to temporal  
460 variations in accumulation (*e.g.*, Nye, 1963), we convert modeled depth to age using the  
461 measured depth-age relationship (SP19; Winski et al. (2019)).

462 The most prominent feature in the thinning function calculated for the Holocene period  
463 is at about 7 ka. The  $\sim 7$  ka layers have thinned less than the layers above, which we  
464 term a “reversal” in the thinning function; for example, Parrenin et al. (2004) noted  
465 such features for the Vostok ice core. For SPC14, reversals can occur because the strain  
466 thinning of layers is affected by changes in ice thickness along the flow line (Figure S18).  
467 As the ice flows from a bedrock high into a trough, the thickening of the ice column  
468 either reduces the vertical thinning or can even cause vertical thickening. Therefore, ice  
469 parcels reaching the  $\sim 7$  ka layer have thinned less than if the bedrock were flat because  
470 the ice column thickened. Ice parcels reaching younger layers, for example the 6 ka layer,  
471 have not experienced this thickening. As the ice flows out of this overdeepening, the rise

472 in bed topography causes thinning of the full ice column (*i.e.*, both the 6 ka and 7 ka  
 473 particles). For the bed topography along the flowline spanning the Holocene time period  
 474 (from SPC14 to 65 km upstream), this bed overdeepening is the only feature that has a  
 475 significant impact on the structure of the thinning function.

#### 476 **Text S5. $\delta^{15}\text{N}$ -based thinning function**

477 We use a thinning function estimated from measurements of  $\delta^{15}\text{N}$  in SPC14 for an ad-  
 478 ditional comparison with the primary thinning function reconstruction described in the  
 479 main text (Figure 6 in main text). Following Parrenin et al. (2012), the  $\delta^{15}\text{N}$ -based thin-  
 480 ning function uses the diffusive column height as calculated from the  $\delta^{15}\text{N}$  measurements  
 481 and the  $\Delta\text{depth}$  as calculated from the ice age scale to determine how much thinning has  
 482 occurred since that ice was at the surface (see main text Section 6.1).

483 We calculate the DCH with (Parrenin et al., 2012):

$$\text{DCH}(t) = (\delta^{15}\text{N}(t) - \Omega(T)\Delta T_{diff}) \left( \frac{\Delta m g \times 1000}{RT(t)} \right)^{-1}, \quad (19)$$

484 where  $\Omega(T)$  is the thermal diffusivity,  $T_{diff}$  is the temperature difference between the top  
 485 and bottom of the diffusive column,  $\Delta m$  is the difference in molar mass between  $^{15}\text{N}$  and  
 486  $^{14}\text{N}$  in  $\text{kg mol}^{-1}$ ,  $g$  is the gravitational acceleration ( $9.81 \text{ m s}^{-2}$ ),  $R$  is the gas constant  
 487 ( $8.314 \text{ J mol}^{-1} \text{ K}^{-1}$ ), and  $T(t)$  is the temperature history in K. We use the temperature  
 488 reconstruction from the optimization in the main text to estimate the temperature history.  
 489 The temperature difference in the firn is calculated using a 1-D ice-and-heat flow model  
 490 (Fudge et al., 2019), also forced by the accumulation-rate reconstruction. The temperature  
 491 dependence of the thermal diffusivity is from Grachev and Severinghaus (2003).

492 The  $\Delta\text{depth}$  is conceptually similar to the  $\Delta\text{age}$  except that it is the difference in depth in  
 493 the core, rather than age, of the same climate event in the ice and gas phases. The  $\Delta\text{depth}$   
 494 is found for each gas tie point used to develop the SP19 gas timescale (Epifanio et al.,  
 495 2020). The depth of the ice of the same age is then found from the SP19 ice timescale  
 496 (Winski et al., 2019).

497 The  $\delta^{15}\text{N}$ -based thinning function ( $\Gamma$ ) can be described:

$$\Gamma(t) = \frac{\Delta\text{depth}(t)}{\int_0^{\text{LID}(t)} D(z, t) dz} = \frac{\Delta\text{depth}(t)}{\text{LIDIE}(t)} = \frac{\Delta\text{depth}(t)}{A \times \text{LID}(t)}, \quad (20)$$

498 where

$$\text{LID}(t) = \text{DCH}(t) + \text{CZ} = \text{DCH}(t) + 3. \quad (21)$$

499  $D(z, t)$  is the density profile of the firn relative to density of ice at a given time,  $\text{LID}(t)$  is  
 500 the lock-in depth,  $\text{LIDIE}(t)$  is the lock-in depth in ice equivalent,  $\text{DCH}(t)$  is the diffusive  
 501 column height, and  $\text{CZ}$  is the thickness of the convective zone, which we set to 3 m (a  
 502 typical value found in firn air pumping experiments).

503 Parrenin et al. (2012) showed that the  $\text{LID}/\text{LDIE}$  ratio changes relatively little for different  
 504 climate conditions at Dome C and thus we can use a constant factor to convert  $\text{LID}$  to  
 505  $\text{LIDIE}$ . We obtain a value of  $A=0.717$  by integrating the SPC14 density profile (Winski  
 506 et al., 2019) from the surface to a density of  $824 \text{ kg m}^{-3}$ . In the following sections, we  
 507 discuss the primary sources of uncertainty in the  $\delta^{15}\text{N}$ -based thinning function.

### 508 *S5.1 Uncertainties*

509 We estimate the uncertainties in the calculation of this thinning function by calculating the  
510 change in the thinning function with a different input for the seven main parameters below  
511 (Figure S19). We choose values which we believe yield approximately 95% confidence (*i.e.*,  
512 2 standard deviation).

513 *Density and depth of firn column:* Converting the LID to LIDIE has two primary un-  
514 certainties: uncertainty in the measured modern density profile and how much variation  
515 there is through time. We estimate the first using six firn cores, two at SPC14 and two  
516 near South Pole, as well as two at 50 km upstream (Lilien et al., 2018). We assume lock-in  
517 density at  $824 \text{ kg m}^{-3}$  with an uncertainty  $\pm 5 \text{ kg m}^{-3}$ . The conversion factor,  $A$ , to get  
518 LIDIE from LID is equivalent to the average density of the firn column relative to the  
519 density of ice, and hence is unitless. To estimate the uncertainty of this conversion factor  
520  $A$ , we find a maximum difference of 0.015 among the six firn cores relative to measured  
521 value for SPC14.

522 For the time-varying uncertainty in the conversion factor  $A$ , we use the pairs of temper-  
523 ature and accumulation rate for each time step found in the primary reconstruction to  
524 force a Herron-Langway densification model. We also allow the surface density to vary by  
525  $\pm 30 \text{ kg m}^{-3}$  from the SPC14 surface density value. We find the largest difference from  
526 the modern SPC14 value to define an uncertainty of 0.023 (2 standard deviation).

527 *Convective zone impact on diffusive column height:* The modern convective zone is 3 m  
528 and we assume the uncertainty is  $\pm 3$  m.

529 *Vertical thinning of firn column due to ice flow:* Separate from firn compaction, there  
530 is vertical thinning caused by the lateral stretching due to ice flow and the effectively

531 incompressible nature of ice under these conditions. Measurements of englacial vertical  
532 velocities have become possible with phase sensitive radars; however, separating the ver-  
533 tical thinning due to ice flow from the vertical compaction of the firn is not yet possible.  
534 Therefore, we approximate this vertical thinning assuming a uniform, ice-equivalent ver-  
535 tical strain rate (*e.g.*, Nye, 1963). We develop the uncertainty by assuming either no  
536 vertical thinning or double our default vertical thinning.

537  *$\Delta$ depth:* We estimate the uncertainty of the  $\Delta$ depth from the  $\Delta$ age uncertainties devel-  
538 oped for the SP19 gas timescale (Epifanio et al., 2020). To find the uncertainty, we take  
539 the difference in depths that correspond to the maximum and minimum gas ages and  
540 divide it in half.

541 *Measurement uncertainty and variability:* The DCH is calculated from the  $\delta^{15}\text{N}$  of  $\text{N}_2$  data  
542 using Equation 19. The uncertainty in determining the DCH depends on three things:  
543 1) the measurement uncertainty of the  $\delta^{15}\text{N}$ ; 2) variability in how well the measurement  
544 represents the actual DCH; and 3) the uncertainty in interpolation from the closest mea-  
545 surement. The  $\delta^{15}\text{N}$  has been measured at 50- to 100-year resolution for much of the  
546 core, such that the interpolation distances are small. To jointly assess these measurement  
547 uncertainty and variability, we compared the DCH estimates of the three closest mea-  
548 surements. On average, the three measurements differed by slightly less than 2 m. The  
549 differences among the three measurements did not have a temporal trend, so we calculate  
550 the uncertainty with a constant 2 m uncertainty. This is the smallest uncertainty for most  
551 of the measurements.

552 *Thermal fractionation:* The thermal fractionation of  $\delta^{15}\text{N}$  is calculated using a 1-D ice-  
553 and-heat flow model (Fudge et al., 2019). The firn-density profile is assumed constant  
554 through time, with the temperature and accumulation-rate histories from the main re-  
555 construction presented here as the primary forcings. The thermal conductivity in the firn  
556 follows the Van Dusen formula (Cuffey and Paterson, 2010). The temperature difference is  
557 calculated from top and bottom of the diffusive column. The isothermal diffusive column  
558 height is used initially in the temperature difference calculation; a new diffusive column  
559 height is computed including thermal fractionation and the temperature difference is then  
560 recalculated. One iteration is sufficient to reach a stable diffusive column height. The  
561 amount of thermal fractionation increases in the glacial compared to the Holocene. This  
562 is driven by the lower glacial accumulation rates, which decrease the vertical advection in  
563 the firn column. Because the base of the firn column is warmer than the surface, warming  
564 will tend to mute the temperature gradient in the firn, while cooling will enhance the  
565 temperature gradient. Thus, the average temperature only weakly impacts the thermal  
566 fractionation, but the trend in the temperature history is important.

567 Developing an uncertainty for the trend in the temperature history is not straightforward  
568 because it requires making assumptions about the magnitude of timing of temperature  
569 change on multi-centennial to millennial timescales. The difference between the main  
570 reconstruction and the scaled water isotopes (Figure 8 in the main text) illustrates the  
571 uncertainty in these higher frequency trends. Therefore, we seek a simple approximation to  
572 capture the main features of the uncertainty to allow comparison with the other sources of  
573 uncertainty in determining the thinning function. We assume an uncertainty in the glacial  
574 period of 3 m, which is half the maximum impact of including thermal fractionation. To

575 reflect the lower uncertainty due to increasing accumulation rates during the transition  
576 into the Holocene, we linearly decrease the uncertainty to 1.5 m from 20 ka to 12 ka,  
577 where it is then constant through the present.

### 578 *S5.2 Total uncertainty on thinning function*

579 To calculate the total uncertainty on the  $\delta^{15}\text{N}$ -based thinning function, we combine the  
580 uncertainty calculated for each of the seven terms above. The uncertainties for each term  
581 are shown in Figure S19. We combine the six sources of uncertainty in quadrature to find  
582 the total uncertainty. For glacial-aged ice, the dominant uncertainty is that for  $\Delta\text{depth}$ .  
583 This is driven by the larger uncertainty in  $\Delta\text{age}$  primarily due to the larger  $\Delta\text{age}$  at  
584 WAIS Divide during the glacial. During the Holocene, all of the terms are more similar  
585 in magnitude, but the uncertainty due to temporal variations in the density profile is the  
586 largest. Our use of a uniform value (.023) for temporal density for the full record is likely  
587 too simplistic, and perhaps too conservative, since the uncertainty is based on glacial  
588 values which differ from modern value far more than the Holocene values.

## 589 References

- 590 Barkan, E & Luz, B. (2007). Diffusivity fractionations of  $\text{H}_2^{16}\text{O}/\text{H}_2^{17}\text{O}$  and  $\text{H}_2^{16}\text{O}/\text{H}_2^{18}\text{O}$   
591 in air and their implications for isotope hydrology. *Rapid Communications in Mass*  
592 *Spectrometry*, 21(18), 2999–3005. <https://doi.org/10.1002/rcm.3180>
- 593 Catania, G, C. Hulbe, & H. Conway, 2010. Grounding-line basal melt rates de-  
594 termined using radar-derived internal stratigraphy, *J. Glaciol.* 56(197), 545–554  
595 <https://doi.org/10.3189/002214310792447842>
- 596 Cuffey, K. M., & Paterson, W. S. B. (2010). The physics of glaciers. Academic Press.
- 597 Dahl-Jensen, D., Mosegaard, K., Gundestrup, N., Clow, G. D., Johnsen, S. J., Hansen,  
598 A. W., & Balling, N. (1998). Past temperatures directly from the Greenland ice sheet.  
599 *Science*, 282(5387), 268–271. <https://doi.org/10.1126/science.282.5387.268>
- 600 Dansgaard, W., & Johnsen, S. J. (1969). A flow model and a time scale for the  
601 ice core from Camp Century, Greenland. *Journal of Glaciology*, 8(53), 215–223.  
602 <https://doi.org/10.3189/S0022143000031208>
- 603 Epifanio, J. A., Brook, E. J., Buizert, C., Edwards, J. S., Sowers, T. A., Kahle, E. C.,  
604 Severinghaus, J. P., Steig, E. J., Winski, D. A., Osterberg, E. C., Fudge, T. J., Aydin,  
605 M., Hood, E., Kalk, M., Kreutz, K. J., Ferris, D. G., & Kennedy, J. A. (2020). The SP19  
606 chronology for the South Pole Ice Core–Part 2: gas chronology,  $\Delta\text{age}$ , and smoothing of  
607 atmospheric records. *Climate of the Past*, 16(6), 2431–2444. [https://doi.org/10.5194/cp-](https://doi.org/10.5194/cp-16-2431-2020)  
608 [16-2431-2020](https://doi.org/10.5194/cp-16-2431-2020)
- 609 Forsberg, R., A.V. Olesen, F. Ferraccioli, T. Jordan, H, Corr, & K. Matsuoka (2017).  
610 PolarGap 2015/16: Filling the GOCE polar gap in Antarctica and ASIRAS flight around  
611 South Pole. Radar grids available at:

- 612 `ftp://ftp.bas.ac.uk/tomj/PolarGAP/PolarGAP_radar_grids.zip`
- 613 Fudge, T. J., Biyani, S. C., Clemens-Sewall, D., & Hawley, R. L. (2019). Constraining  
614 geothermal flux at coastal domes of the Ross Ice Sheet, Antarctica. *Geophysical Research  
615 Letters*, 46(22), 13090–13098. <https://doi.org/10.1029/2019GL084332>
- 616 Fudge, T. J., Lilien, D. A., Koutnik, M., Conway, H., Stevens, C. M., Waddington, E. D.,  
617 Steig, E. J., Schauer, A. J., & Holschuh, N. (2020). Advection and non-climate impacts  
618 on the South Pole Ice Core. *Clim. Past*, 16, 819–832. [https://doi.org/10.5194/cp-16-  
619 819-2020](https://doi.org/10.5194/cp-16-819-2020)
- 620 Gades, A. M., Raymond, C. F., Conway, H., & Jacobel, R. W. (2000). Bed  
621 properties of Siple Dome and adjacent ice streams West Antarctica, inferred  
622 from radio-echo sounding measurements. *Journal of Glaciology*, 46(152), 88–94.  
623 <https://doi.org/10.3189/172756500781833467>
- 624 Gelman, A., Roberts, G. & Gilks W. (1996). Efficient Metropolis jumping rules, in  
625 Bayesian Statistics 5, Berger, J. O., Bernardo, J. M., Dawid, A. P. and Smith, A.  
626 F. M. (eds), Oxford University Press.
- 627 Gkinis, V., Simonsen, S. B., Buchardt, S. L., White, J. W. C., & Vinther, B. M. (2014).  
628 Water isotope diffusion rates from the NorthGRIP ice core for the last 16,000 years -  
629 glaciological and paleoclimatic implications. *Earth and Planetary Science Letters*, 405,  
630 132–141. <https://doi.org/10.1016/j.epsl.2014.08.022>
- 631 Gkinis, V., Holme, C., Kahle, E.C., Stevens, C.M., Steig, E.J., & Vinther, B.M. (2021).  
632 Numerical experiments on firn isotope diffusion with the Community Firn Model. *Jour-  
633 nal of Glaciology*, 1–23. doi:10.1017/jog.2021.1

- 634 Goujon, C., Barnola, J. M., & Ritz, C. (2003). Modeling the densification of polar firn in-  
635 cluding heat diffusion: Application to close-off characteristics and gas isotopic fractiona-  
636 tion for Antarctica and Greenland sites. *Journal of Geophysical Research: Atmospheres*,  
637 108(D24). <https://doi.org/10.1029/2002JD003319>
- 638 Grachev, A. M., & Severinghaus, J. P. (2003). Laboratory determination of thermal dif-  
639 fusion constants for  $^{29}\text{N}_2/^{28}\text{N}_2$  in air at temperatures from 60 to 0 C for reconstruction  
640 of magnitudes of abrupt climate changes using the ice core fossil–air paleothermome-  
641 ter. *Geochimica et Cosmochimica Acta*, 67(3), 345–360. [https://doi.org/10.1016/S0016-](https://doi.org/10.1016/S0016-7037(02)01115-8)  
642 [7037\(02\)01115-8](https://doi.org/10.1016/S0016-7037(02)01115-8)
- 643 Herron, M. M., & Langway, C. C. (1980). Firn densification: an empirical model. *Journal*  
644 *of Glaciology*, 25(93), 373–385. <https://doi.org/10.3189/S0022143000015239>
- 645 Johnsen, S. J., Clausen, H. B., Cuffey, K. M., Hoffmann, G., Schwander, J., & Creyts,  
646 T. (2000). Diffusion of stable isotopes in polar firn and ice: The isotope effect in firn  
647 diffusion. T. Hondoh (Ed.), *Physics of Ice Core Records*, Hokkaido University Press,  
648 Sapporo (2000), pp. 121–140.
- 649 Jones, T. R., White, J. W. C., Steig, E. J., Vaughn, B. H., Morris, V., Gkinis, V.,  
650 Markle, B. R., & Schoenemann, S. W. (2017b). Improved methodologies for continuous  
651 flow analysis of stable water isotopes in ice cores. *Atmospheric Measurement Techniques*,  
652 10, 617–632. <https://doi.org/10.5194/amt-10-617-2017>
- 653 Jordan, T. A., Martin, C., Ferraccioli, F., Matsuoka, K., Corr, H., Forsberg, R., Ole-  
654 sen, A., & Siegert, M. (2018). Anomalously high geothermal flux near the South Pole.  
655 *Scientific reports*, 8(1), 1–8. <https://doi.org/10.1038/s41598-018-35182-0>

- 656 Kahle, E. C. (2020). Climate reconstructions from ice cores: New techniques to un-  
657 derstand the information preserved in the South Pole ice core (Doctoral dissertation,  
658 University of Washington, Seattle, USA). <http://hdl.handle.net/1773/45398>
- 659 Khan, A., Mosegaard, K., & Rasmussen, K. L. (2000). A new seismic velocity model for  
660 the Moon from a Monte Carlo inversion of the Apollo lunar seismic data. *Geophysical*  
661 *Research Letters*, 27(11), 1591–1594. <https://doi.org/10.1029/1999GL008452>
- 662 Koutnik, M. R., Fudge, T. J., Conway, H., Waddington, E. D., Neumann, T. A., Cuffey,  
663 K. M., Taylor, K. C., et al. (2016). Holocene accumulation and ice flow near the West  
664 Antarctic Ice Sheet Divide ice core site. *Journal of Geophysical Research: Earth Surface*,  
665 121(5), 907–924. <https://doi.org/10.1002/2015JF003668>
- 666 Lamb, K. D., Clouser, B. W., Bolot, M., Sarkozy, L., Ebert, V., Saathoff, H., Mohler, O.,  
667 & Moyer, E. J. (2017). Laboratory measurements of HDO/H<sub>2</sub>O isotopic fractionation  
668 during ice deposition in simulated cirrus clouds. *Proceedings of the National Academy*  
669 *of Sciences*, 114(22), 5612–5617. <https://doi.org/10.1073/pnas.1618374114>
- 670 Li, J. & Zwally, H. J. (2015). Response times of ice-sheet surface heights to changes in the  
671 rate of Antarctic firn compaction caused by accumulation and temperature variations.  
672 *Journal of Glaciology*, 61(230), 1037–1047. <https://doi.org/10.3189/2015JoG14J182>
- 673 Ligtenberg, S. R. M., Helsen, M. M., & Van den Broeke, M. R. (2011). An improved  
674 semi-empirical model for the densification of Antarctic firn. *The Cryosphere*, 5, 809–  
675 819. <https://doi.org/10.5194/tc-5-809-2011>
- 676 Lilien, D. A., Fudge, T. J., Koutnik, M. R., Conway, H., Osterberg, E. C.,  
677 Ferris, D. G., & Stevens, C. M. et al. (2018). Holocene Ice-Flow Speedup in  
678 the Vicinity of the South Pole. *Geophysical Research Letters*, 45(13), 6557–6565.

- 679 <https://doi.org/10.1029/2018GL078253>
- 680 Looyenga, H. (1965). Dielectric constants of heterogeneous mixtures. *Physica*, 31(3), 401–  
681 406. [https://doi.org/10.1016/0031-8914\(65\)90045-5](https://doi.org/10.1016/0031-8914(65)90045-5)
- 682 Luz, B. & Barkan, E. (2010). Variations of 17O/16O and 18O/16O in  
683 meteoric waters. *Geochimica et Cosmochimica Acta*, 74(22), 6276–6286.  
684 <https://doi.org/10.1016/j.gca.2010.08.016>
- 685 Majoube, B. (1970). Fractionation factor of <sup>18</sup>O between water vapour and ice. *Nature*  
686 226, 1242. <https://doi.org/10.1038/2261242a0>
- 687 Metropolis, N., Rosenbluth, A. W., Rosenbluth, M. N., Teller, A. H., & Teller, E. (1953).  
688 Equation of state calculations by fast computing machines. *The Journal of Chemical*  
689 *Physics*, 21(6), 1087–1092. <https://doi.org/10.1063/1.1699114>
- 690 Mosegaard, K. & Tarantola, A. (1995). Monte Carlo sampling of solutions to in-  
691 verse problems. *Journal of Geophysical Research: Solid Earth*, 100(B7), 12431–12447.  
692 <https://doi.org/10.1029/94JB03097>
- 693 Mosegaard, K. (1998). Resolution analysis of general inverse problems through inverse  
694 Monte Carlo sampling. *Inverse Problems*, 14(3), 405. [https://doi.org/10.1088/0266-](https://doi.org/10.1088/0266-5611/14/3/004)  
695 [5611/14/3/004](https://doi.org/10.1088/0266-5611/14/3/004)
- 696 Mosegaard, K., & Tarantola, A. (2002). Probabilistic approach to inverse problems. In  
697 W. Lee, P. Jennings, C. Kisslinger, & H. Kanamori (Eds.), *International Handbook of*  
698 *Earthquake & Engineering Seismology (Part A)* (237–265). Academic Press.
- 699 Mosegaard, K. & Sambridge, M. (2002). Monte Carlo analysis of inverse problems. *Inverse*  
700 *problems*, 18(3), R29. <https://doi.org/10.1088/0266-5611/18/3/201>

- 701 Neumann, T. A., Conway, H., Price, S., Waddington, E. D., & Morse, D. L. (2008).  
702 Holocene accumulation and ice-sheet dynamics in central West Antarctica. *Journal of*  
703 *Geophysical Research*, 113(F2). <https://doi.org/10.1029/2007JF000764>
- 704 Nye, J. 1963. Correction factor for accumulation measured by the thickness  
705 of the annual layers in an ice sheet. *Journal of Glaciology*, 4(36), 785–788.  
706 <https://doi.org/10.3189/S0022143000028367>
- 707 Parrenin, F., Remy, F., Ritz, C., Siegert, M. J., & Jouzel, J. (2004). New modeling of the  
708 Vostok ice flow line and implication of the glaciological chronology of the Vostok ice core.  
709 *Journal of Geophysical Research*, 109, (D20). <https://doi.org/10.1029/2004JD004561>
- 710 Parrenin, F., Barker, S., Blunier, T., Chappellaz, J., Jouzel, J., Landais, A., Veres, D.  
711 et al. (2012). On the gas-ice depth difference ( $\Delta$ depth) along the EPICA Dome C ice  
712 core. *Climate of the Past*, 8(2), 1089–1131. <https://doi.org/10.5194/cpd-8-1089-2012>
- 713 Price, P. B., Nagornov, O. V., Bay, R., Chirkin, D., He, Y., Miocinovic, P.,  
714 Richards, A., Woschnagg, K., Koci, B., & Zagorodnov, V. (2002). Temperature  
715 Profile for Glacial Ice at the South Pole: Implications for Life in a Nearby Sub-  
716 glacial Lake. *Proceedings of the National Academy of Sciences*, 99(12), 7844–7847.  
717 <https://doi.org/10.1073/pnas.082238999>
- 718 Raymond, C. (1983). Deformation in the vicinity of ice divides. *Journal of Glaciology*,  
719 29(103), 357–373. <https://doi.org/10.3189/S0022143000030288>
- 720 Schwander, J., Stauffer, B., & Sigg, A. (1988). Air mixing in firn and  
721 the age of the air at pore close-off. *Annals of Glaciology*, 10, 141–145.  
722 <https://doi.org/10.3189/S0260305500004328>

- 723 Simonsen, S. B., Stenseng, L., Adalgeirsdottir, G., Fausto, R. S., Hvidberg, C. S., &  
724 Lucas-Picher, P. (2013). Assessing a multilayered dynamic firn-compaction model for  
725 Greenland with ASIRAS radar measurements. *Journal of Glaciology*, 59 (215), 545–558.  
726 <https://doi.org/10.3189/2013JoG12J158>
- 727 Steen-Larsen, H. C., Waddington, E. D., & Koutnik, M. R. (2010). Formulating an  
728 inverse problem to infer the accumulation-rate pattern from deep internal layering in  
729 an ice sheet using a Monte Carlo approach. *Journal of Glaciology*, 56(196), 318–332.  
730 <https://doi.org/10.3189/002214310791968476>
- 731 Stevens, C. M., Verjans, V., Lundin, J., Kahle, E. C., Horlings, A. N., Horlings, B. I.,  
732 & Waddington, E. D. (2020). The Community Firn Model (CFM) v1. 0. *Geoscientific*  
733 *Model Development*, 13(9), 4355–4377. <https://doi.org/10.5194/gmd-13-4355-2020>
- 734 Tarantola, A. (1987). Inverse problem theory: Methods for data fitting and model pa-  
735 rameter estimation. *Elsevier Science*, Amsterdam.
- 736 Winski, D. A., Fudge, T. J., Ferris, D. G., Osterberg, E. C., Fegyveresi, J. M., Cole-Dai,  
737 J., Buizert, C. et al. (2019). The SP19 chronology for the South Pole Ice Core–Part 1:  
738 volcanic matching and annual layer counting. *Climate of the Past*, 15(5), 1793–1808.  
739 <https://doi.org/10.5194/cp-15-1793-2019>

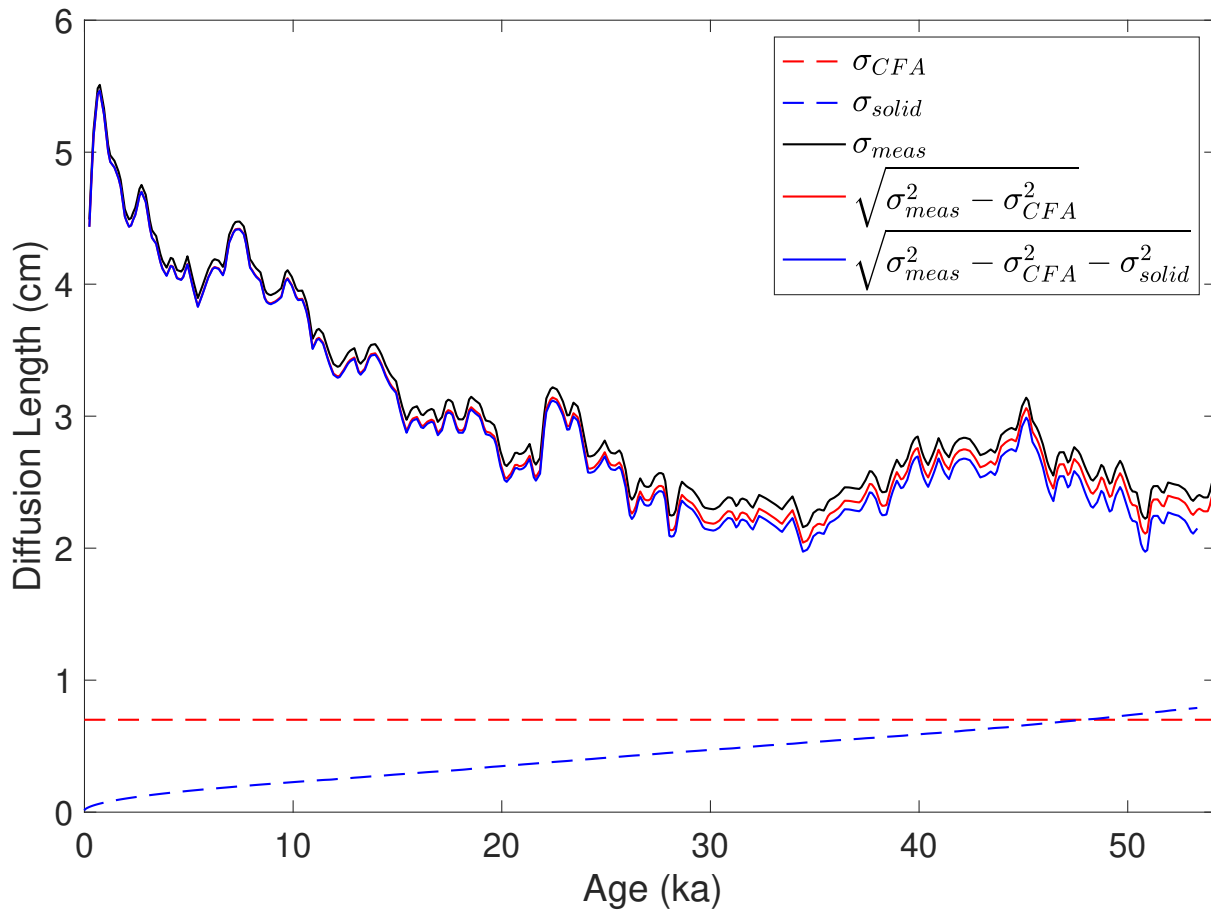


Figure S1: Impact of corrections applied to diffusion-length measurements. Dashed curves show the effective diffusion length resulting from the continuous-flow system (CFA, red), and from diffusion in solid ice (blue). Solid curves show diffusion lengths obtained from the water-isotope data before (black) and after correction for the CFA (red) and solid-ice diffusion (blue).

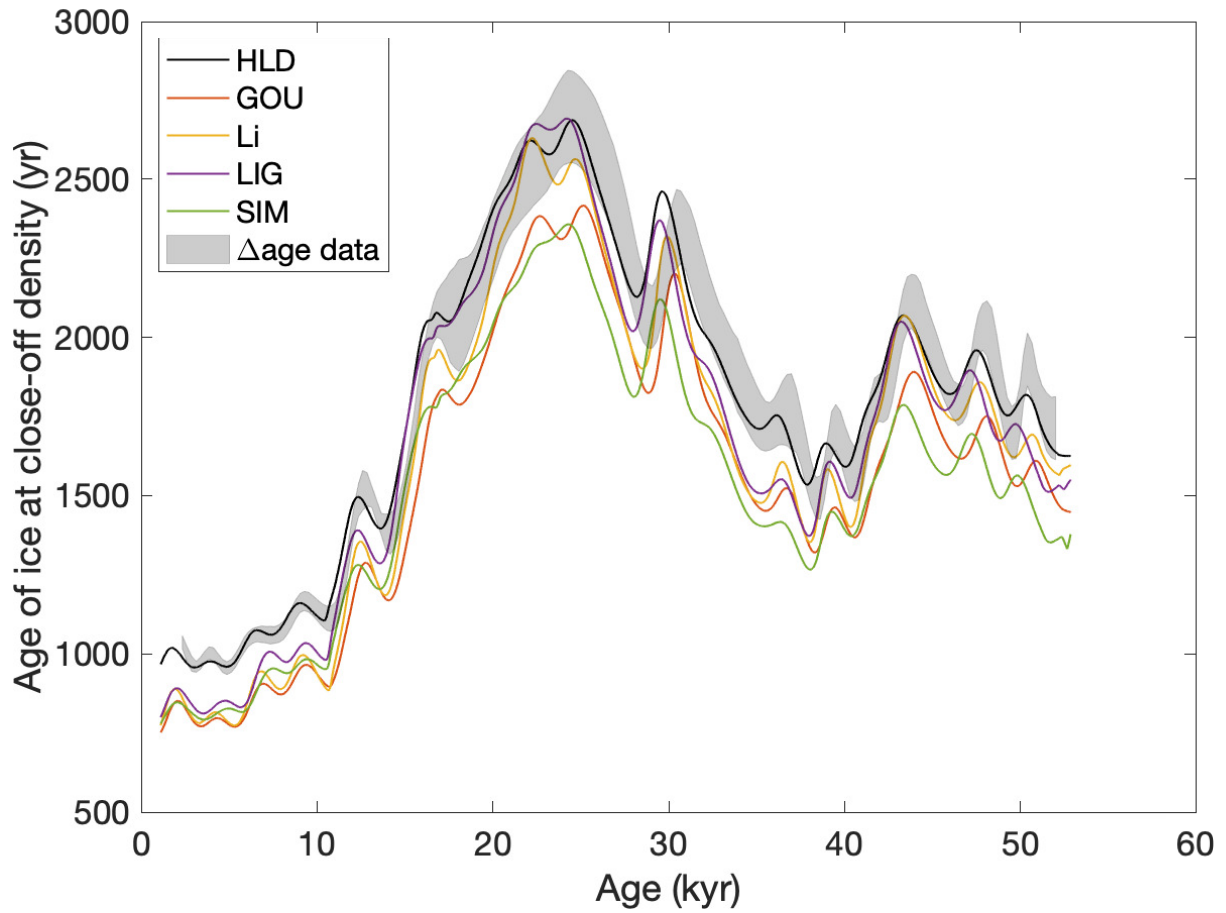


Figure S2: Close-off age as a function of age for a collection of models from the Community Firn Model framework (HLD = Herron and Langway (1980), GOU = Goujon et al. (2003), Li = Li and Zwally (2015), LIG = Ligtenberg et al. (2011), SIM = Simonsen et al. (2013)). The grey shading shows the  $\Delta$ age data and two s.d. uncertainty.

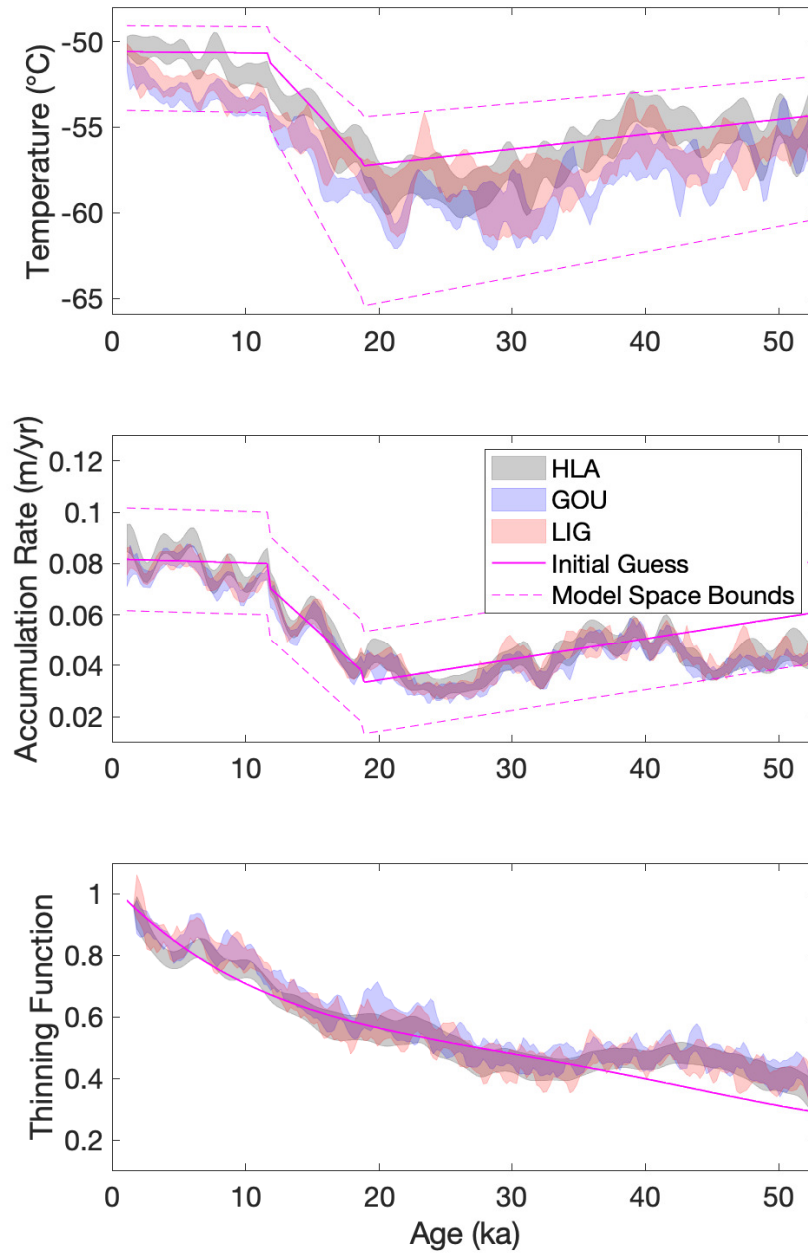


Figure S3: Results of inverse procedure using three different firn models. Grey, blue, and red shading show two s.d. results for Herron and Langway (1980) (HLA), Goujon et al. (2003) (GOU), and Ligtenberg et al. (2011) (LIG), respectively.

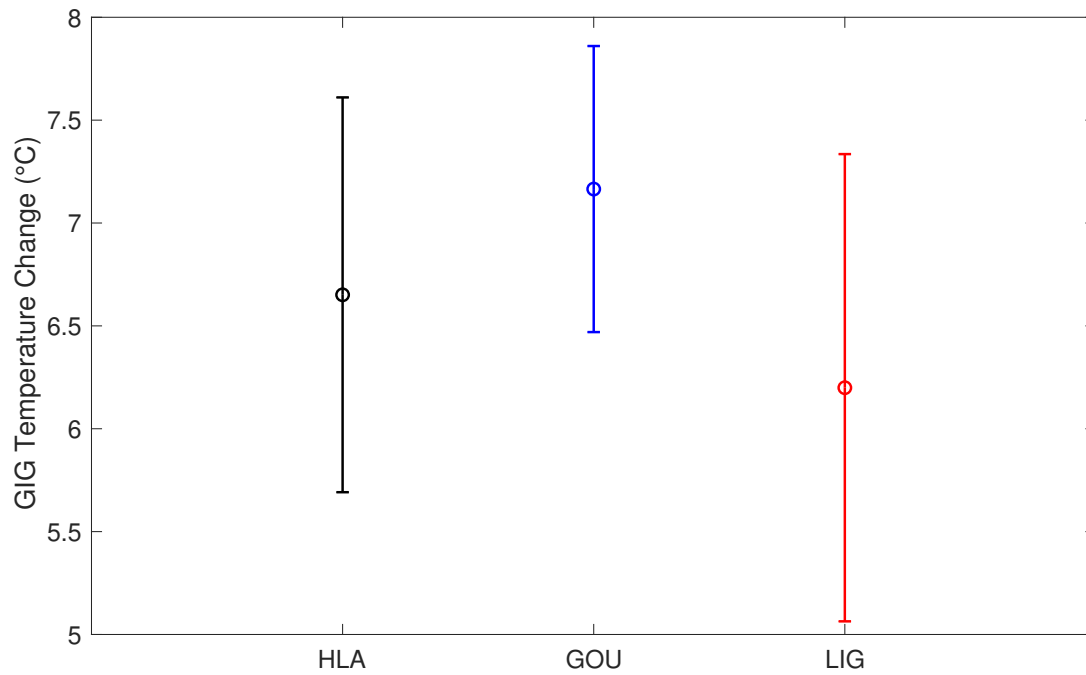


Figure S4: Glacial-interglacial temperature change from the inverse framework with three different firn models. Mean and one s.d. are shown for Herron and Langway (1980) (HLA), Goujon et al. (2003) (GOU), and Ligtenberg et al. (2011) (LIG). The temperature difference is calculated on the intervals defined in the main text: present = 500-2500 years; glacial = 19500-22500 years. The temperature reconstructions have been corrected for ice advection from upstream, resulting in a temperature change estimate for the South Pole site.

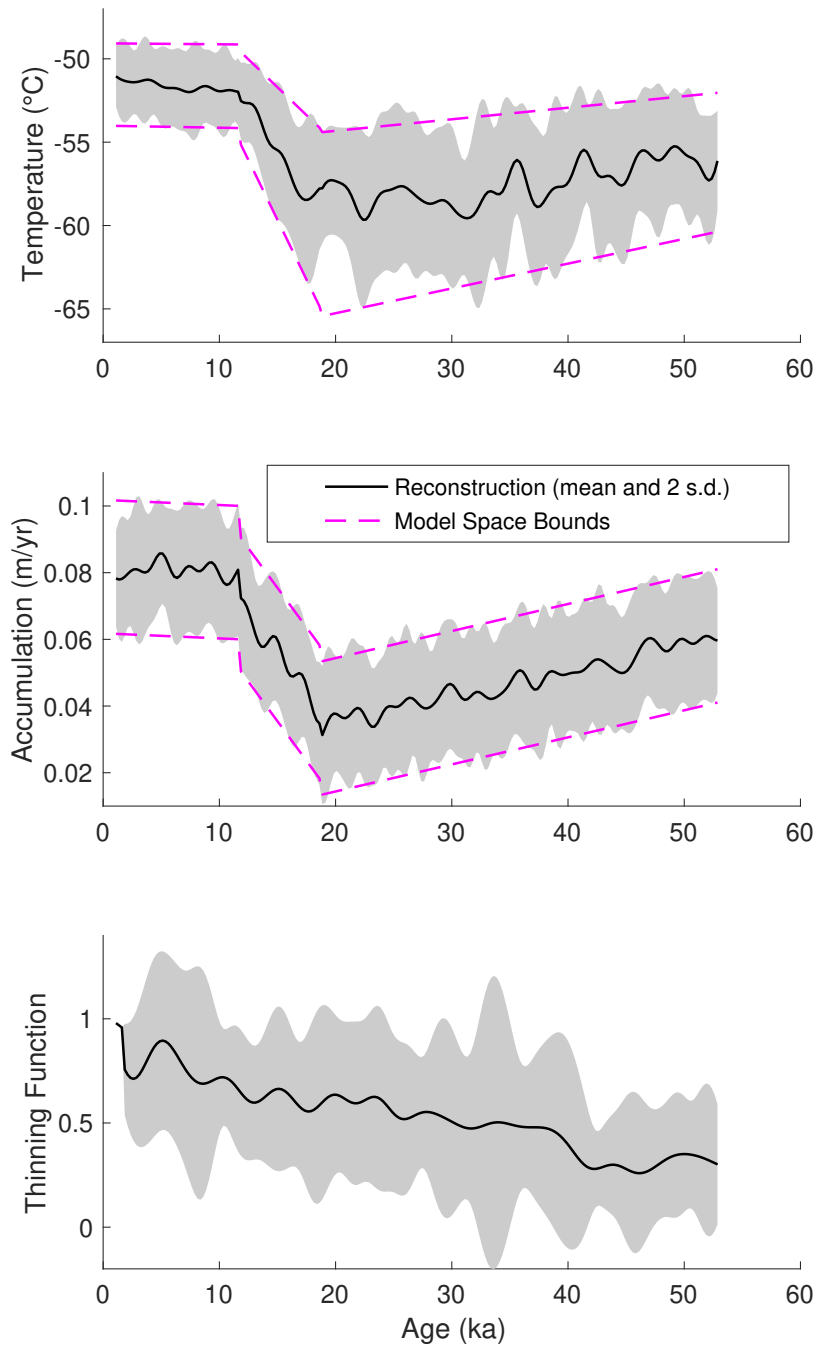


Figure S5: Results of the null test to recover the *a priori* distribution. In the upper two panels, for which model bounds are defined, two standard deviations of the *a posteriori* distribution (grey shading) approximately fill the bounded space (dashed magenta lines), and the mean of the distribution (black curve) is approximately the mean of the bounds.

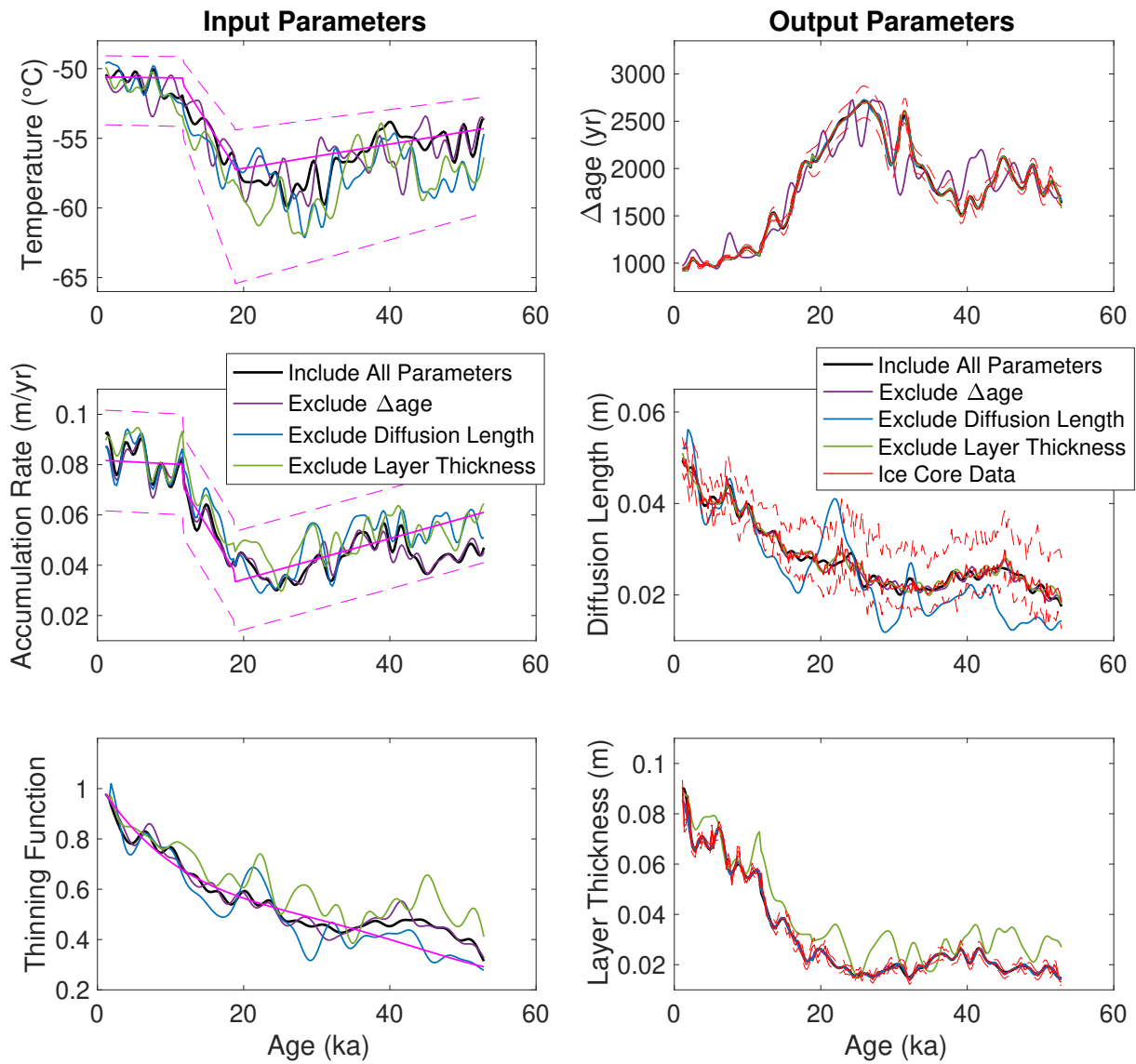


Figure S6: Analysis of the sensitivity of the *a posteriori* distribution to information in each data set. Each color shows the *a posteriori* distribution mean for a different sensitivity test. We compare the results when  $\Delta\text{age}$  is excluded (purple), when diffusion length is excluded (blue), when layer thickness is excluded (green), and when all data sets are included (black). Magenta curves in the left panels show *a priori* information and red curves in the right panels show ice-core data and uncertainties.

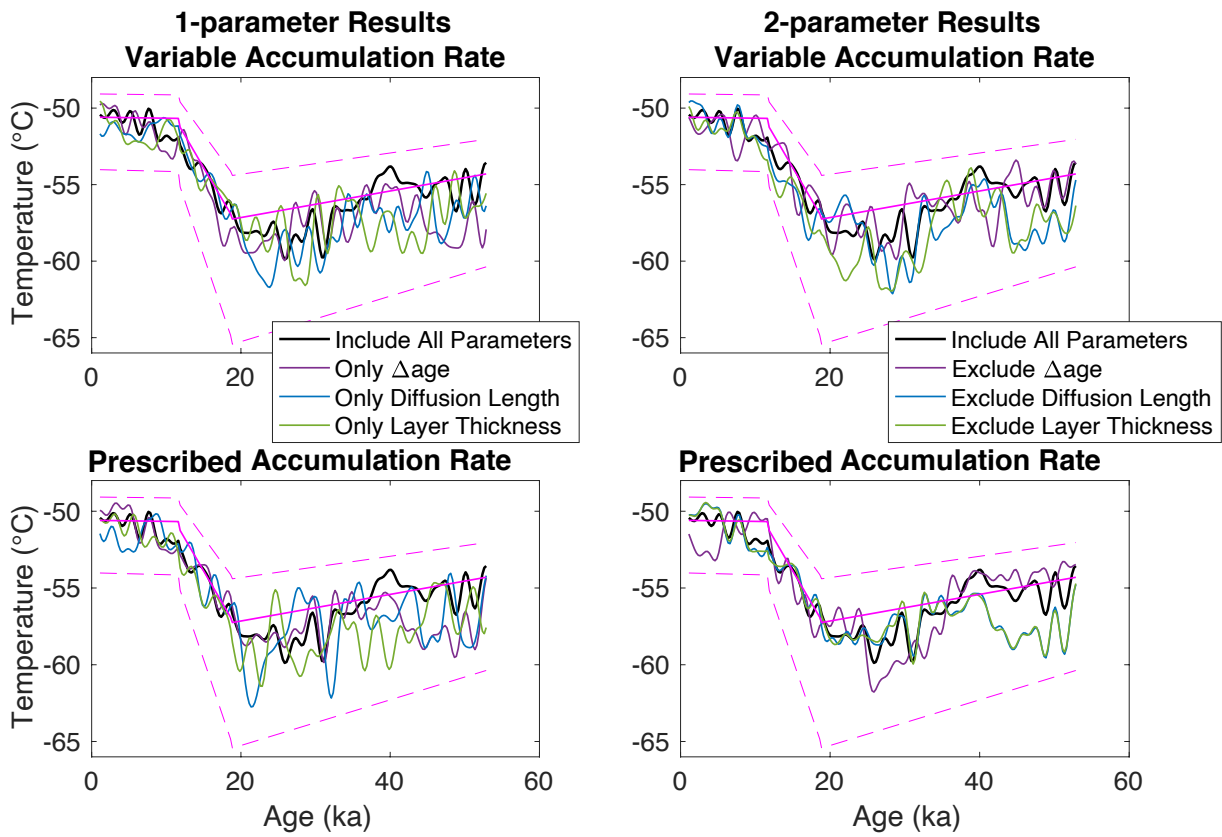


Figure S7: Analysis of the sensitivity of temperature to information in each data set. Colors are defined as in Figure S6. The results of the 1-parameter suite are shown on the left and of the 2-parameter suite on the right. The upper row shows the result when accumulation rate is allowed to vary, and the lower row shows the result when accumulation rate is held at the prescribed values.

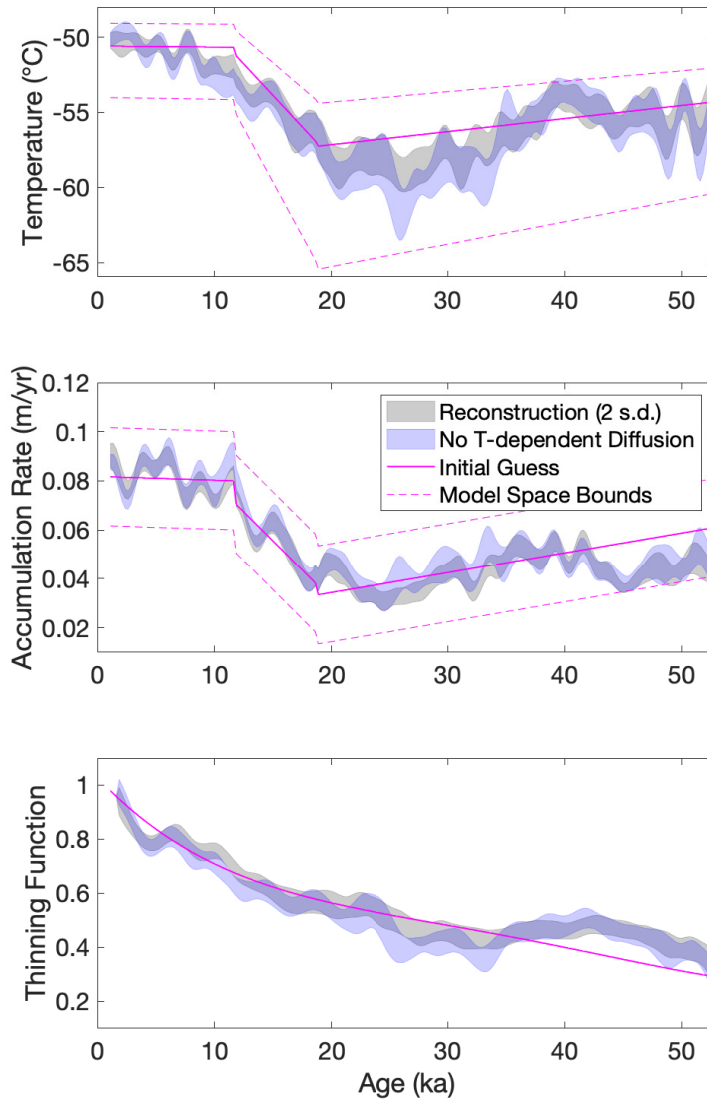


Figure S8: Analysis of sensitivity to the temperature dependence within the water-isotope diffusion model. Grey shading shows the main inverse result as a control test. Blue shading shows the results from holding the temperature history constant within the water-isotope diffusion model, only allowing the diffusion-length data to impact the thinning function.

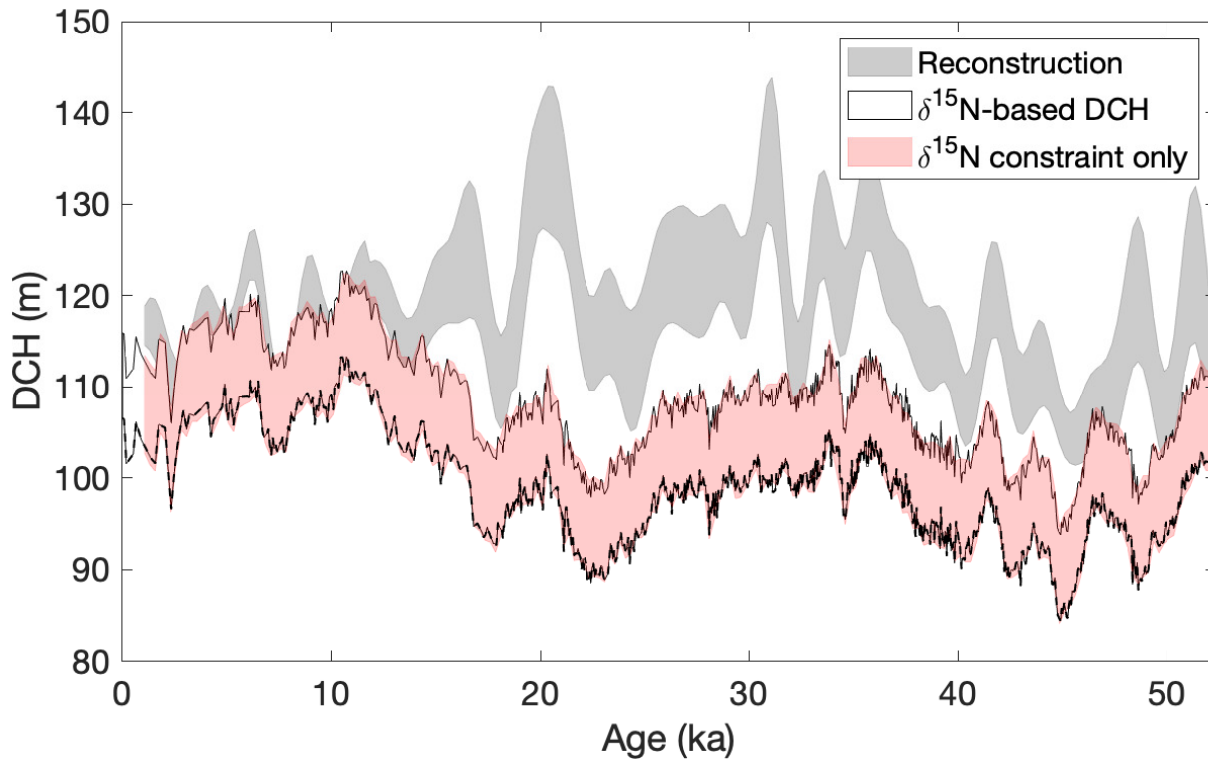


Figure S9: Comparison of diffusive column height (DCH), shown as two s.d. for each source. Grey shading shows the DCH as modeled by the temperature and accumulation rate solutions accepted in the main reconstruction. The black outline shows the DCH as calculated from the  $\delta^{15}\text{N}$  data. Red shading shows the  $\delta^{15}\text{N}$ -constrained DCH, reconstructed from the temperature and accumulation-rate histories shown in Figure 5 in the main text.

Table S1: Sensitivity of the relationship between water isotopes and temperature. Calibrated slopes are given for the relationship between water isotopes and temperature from five different temperature reconstructions: the main inverse result, the results from using the GOU and LIG firn models instead of HLA, and the results from using the constraints of the  $\delta^{15}\text{N}$  and  $\Delta\text{age}$  data sets. The correlation coefficient  $r$  is given for the relationship between the water-isotope record and each temperature reconstruction.

<b>Reconstruction</b>	<b>Slope (<math>\text{‰}^\circ\text{C}^{-1}</math>)</b>	<b><math>r</math></b>
Main	0.99	0.94
GOU	0.97	0.94
LIG	1.10	0.90
$\delta^{15}\text{N}$	1.28	0.84
$\delta^{15}\text{N}$ & $\Delta\text{age}$	1.14	0.86

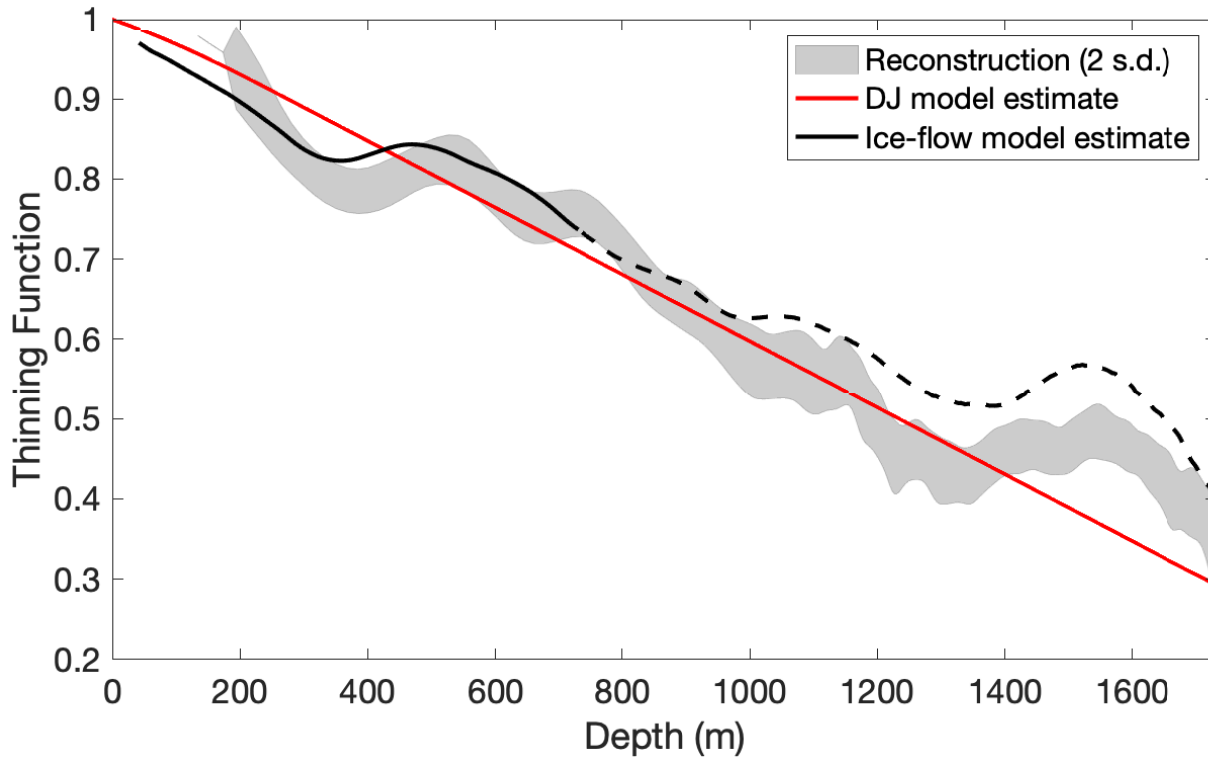


Figure S10: Comparison of primary thinning reconstruction (grey band shows two s.d. uncertainty), the 1-D Dansgaard-Johnsen model output (red) plotted against depth, and the thinning estimate from the 2.5-D ice flow model (black). As in Figure 6 in the main text, the dashed black line shows the depths at which the upstream bed topography is unknown. The reconstruction shows considerably more high-frequency variability. Note that the reconstruction band collapses to a line at the upper depth points due to an imposed constraint of *a priori* information to limit variability in the uppermost part of the thinning function.

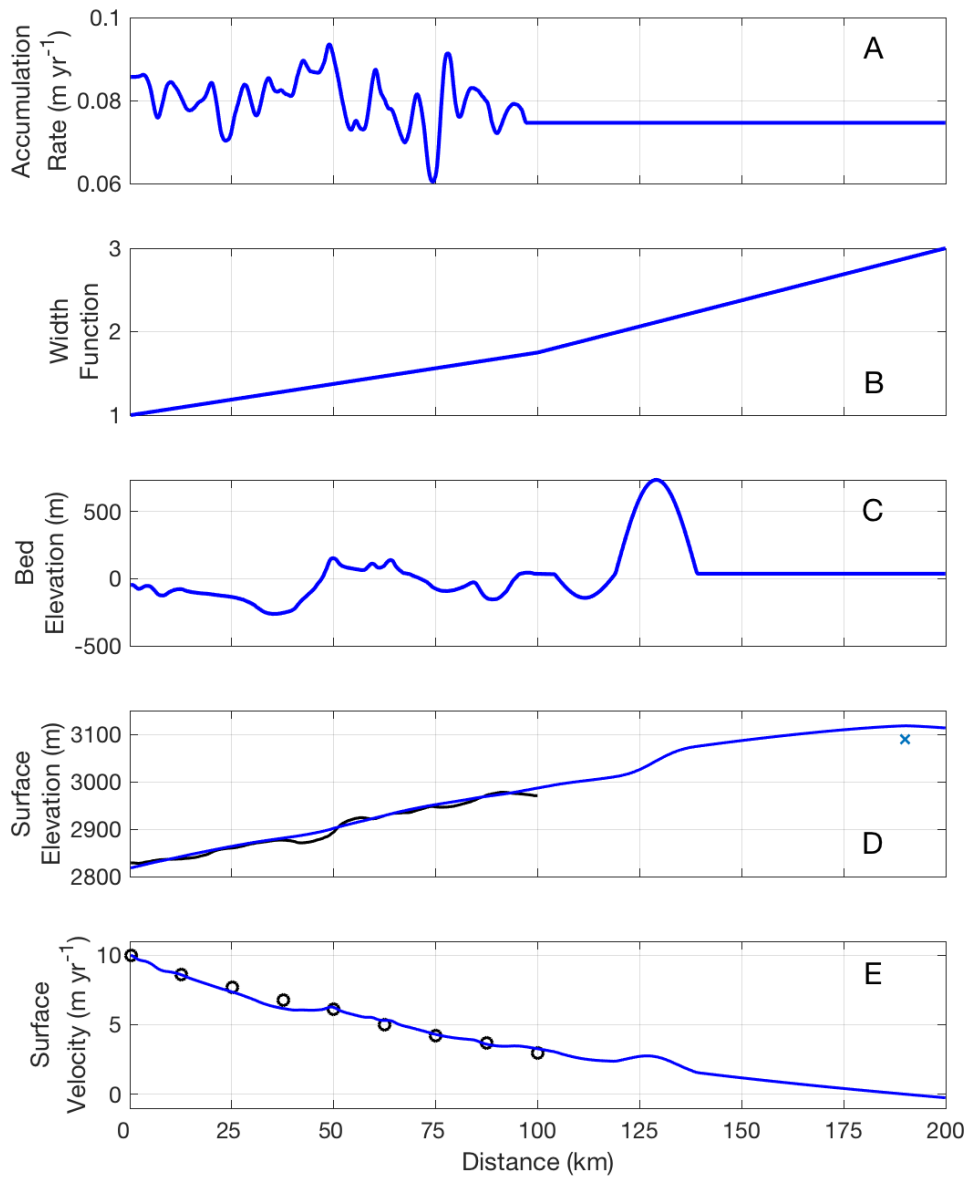


Figure S11: Flowband model inputs (A-C) and model fits to measured data (D-E). A) Modern accumulation-rate pattern for 100 km upstream of SPC14 site inferred from the available shallow radar measurements (Lilien et al., 2018; Fudge et al., 2020). B) Normalized width function used to fit measured surface velocities in panel E. C) Bed topography was measured from 0 to 100 km. Beyond 100 km, the bed topography used in the model is determined as discussed in Text S4.2. D) Measured (black) and modeled surface elevation (blue). The small black “x” at 190 km marks the approximate position and elevation of Titan Dome relative to SPC14. E) Measured (black circles) and modeled surface velocities (blue).

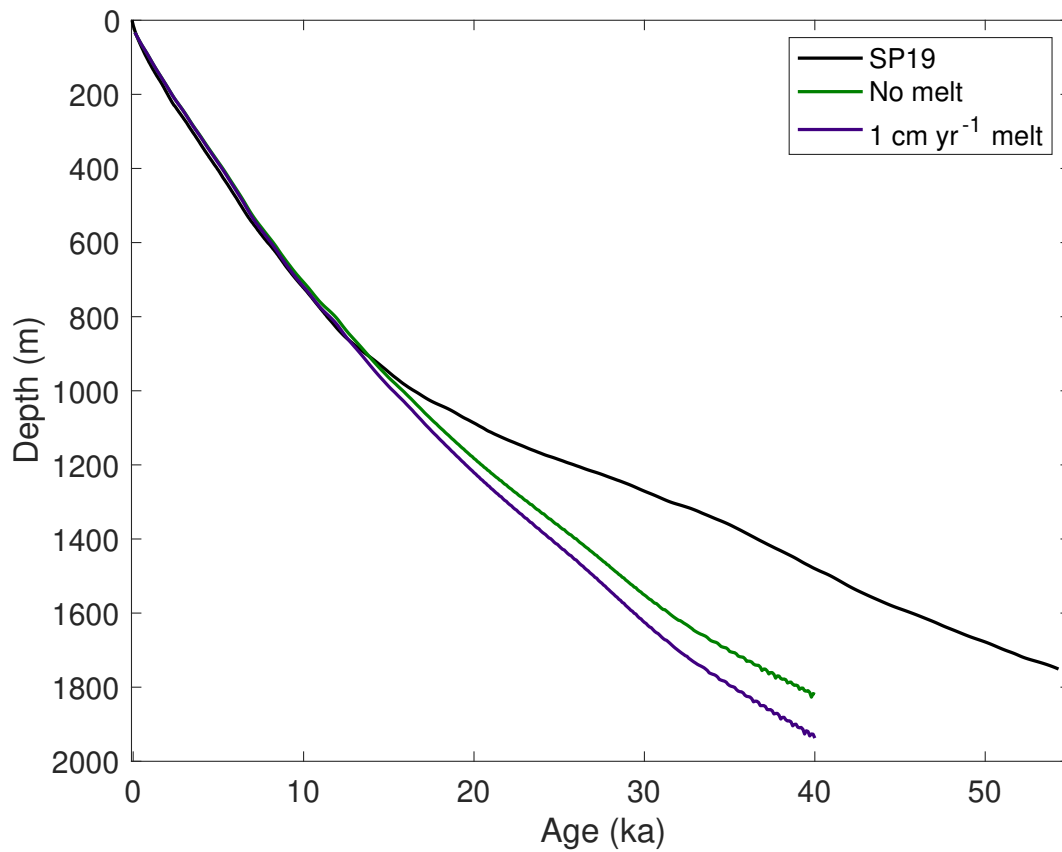


Figure S12: Comparison between modeled and measured depth-age relationship. The depth-age relationship from the steady-state models compare well to SP19 (Winski et al., 2019) for the Holocene. The divergence in the modeled values compared to SP19 values below approximately 900 m depth is due to the decrease in accumulation rate at older ages that we do not simulate with the steady-state model.

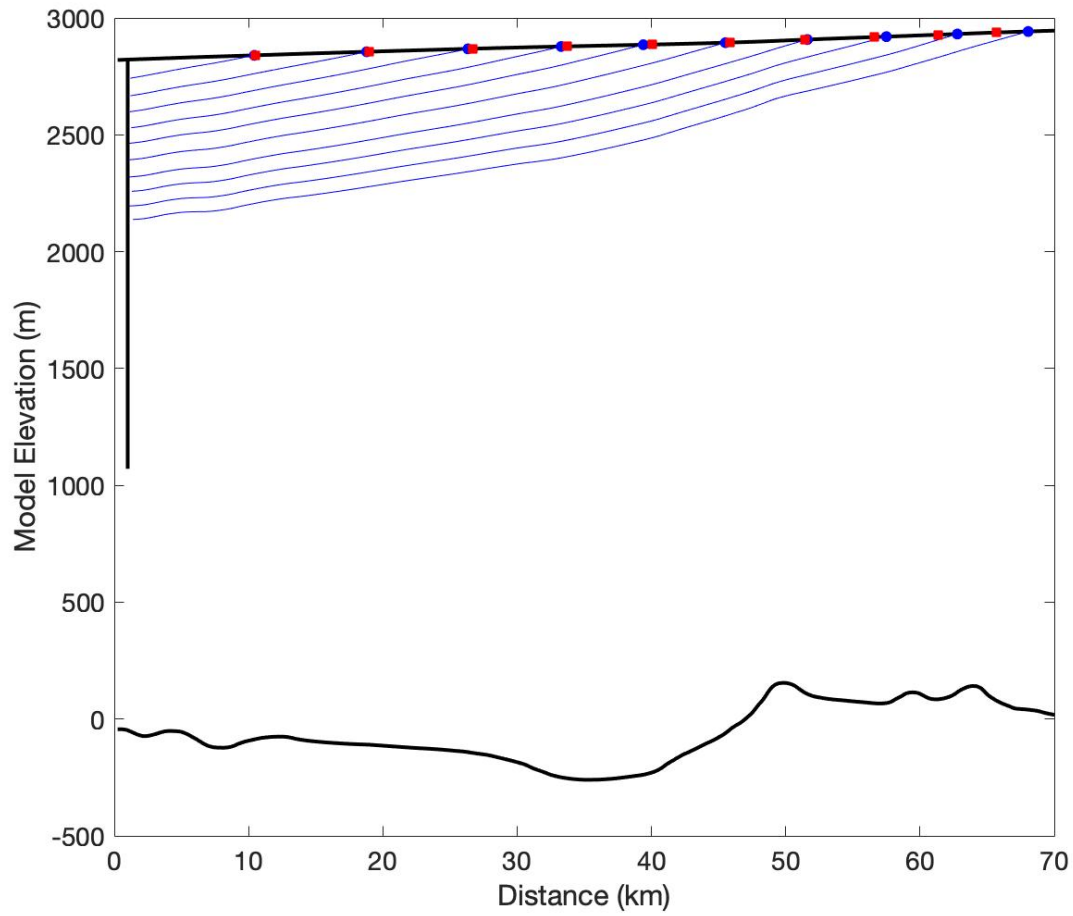


Figure S13: The origin location of ice parcels in 1 ka increments are shown in red squares for the reconstruction of Lilien et al. (2018) and the flowband model used in this study (blue dots). The blue lines are the modeled ice parcel paths. The black vertical line at 1 km represents the 1751 m deep SPC14.

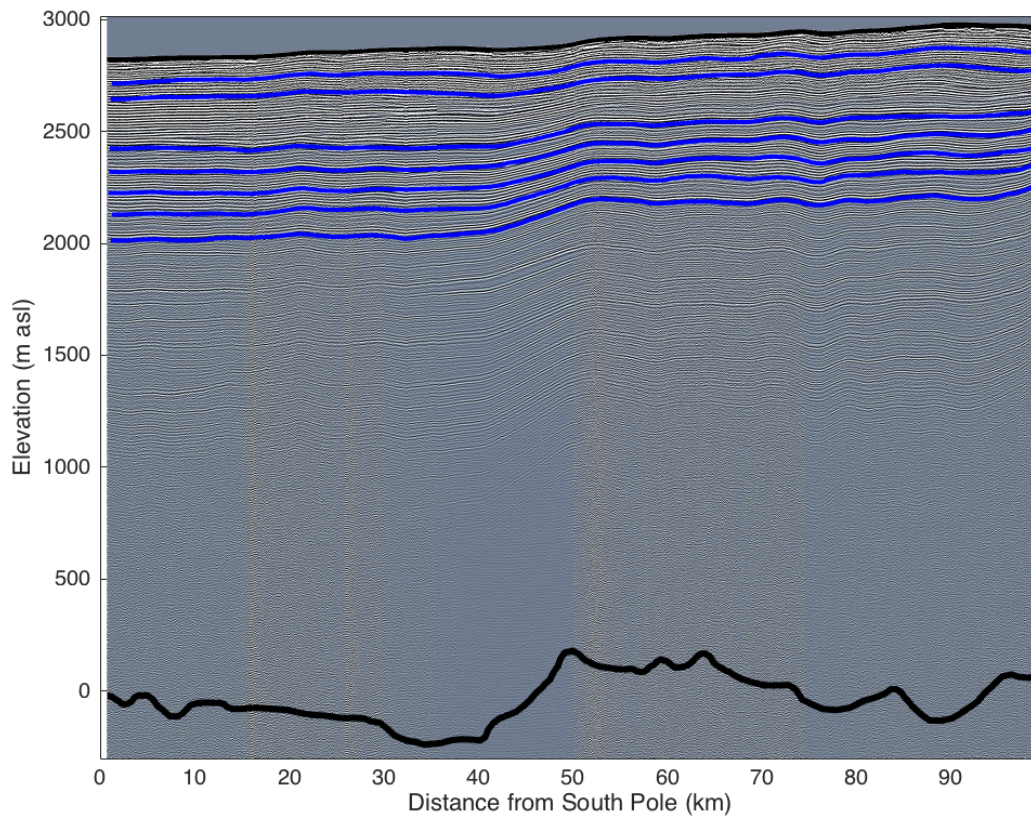


Figure S14: Radar profile along 100 km of the modern flowline upstream of SPC14 (see map, Figure S16). The data were imaged using a ground-based, bistatic impulse radar with center frequency of 7 MHz. The transmitter and receiver were towed inline behind a skidoo; each record consists of 1024 stacked waveforms and records were located using GPS. Reflection positions, measured as a function of radar two-way travel time, were converted to depth below the surface using a wave speed of  $168.5 \text{ m } \mu\text{s}^{-1}$  in ice and  $300 \text{ m } \mu\text{s}^{-1}$  in air. Wave speed in the firn was calculated using the density profile from SPC14 and a mixing equation (Looyenga, 1965) to estimate the depth profile of the dielectric constant. Solid black curves show the surface and bed elevations (m above sea level (asl)). Note that the SPC14 site is about 40 m below sea level. Blue curves are radar-detected internal layers (isochrones) that were dated using the SPC14 timescale. Layer ages with increasing depth are: 1020, 1900, 5070, 6510, 8070, 9690, and 11770 years.

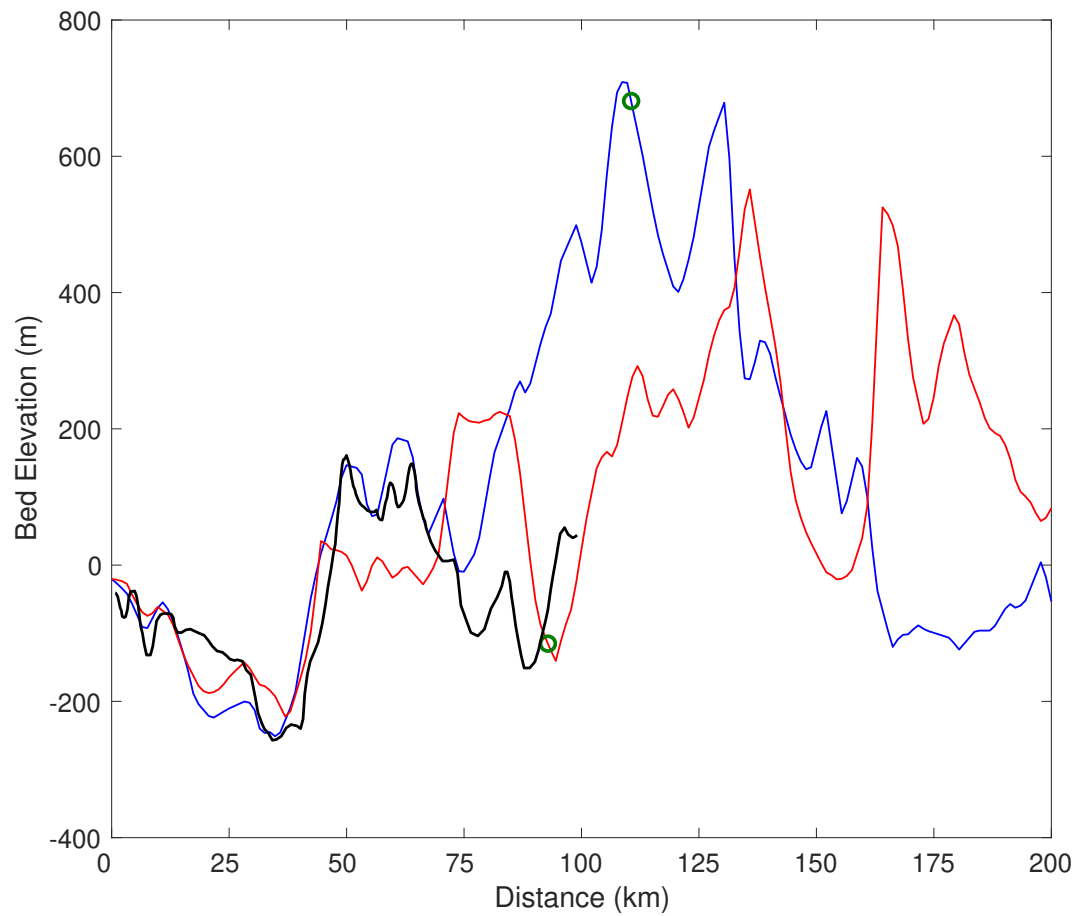


Figure S15: Profiles of bed topography upstream of the SPC14 site. Black is the bedrock measured along the modern flowline. Red is along  $142.5^{\circ}$  E and blue is along  $135^{\circ}$  E from the PolarGAP survey. Green circles mark the two points that we use to define a plausible bed feature to explain the thinning function for older ages (circles correspond to Figure S16).

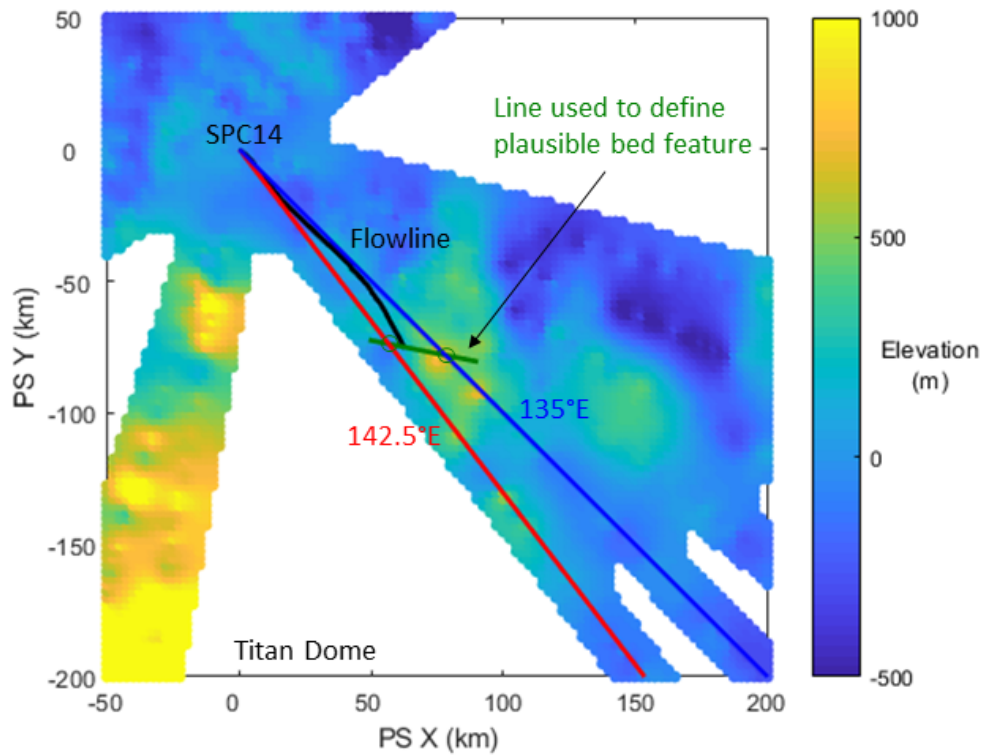


Figure S16: Map view of bed topography near SPC14. Black shows measured flowline. Red is along  $142.5^\circ$  E and blue is along  $135^\circ$  E from the PolarGAP survey. Green line shows the transect between PolarGAP lines used to guide the bed topographic feature beyond 100 km in the ice-flow modeling (circles correspond to Figure S15).

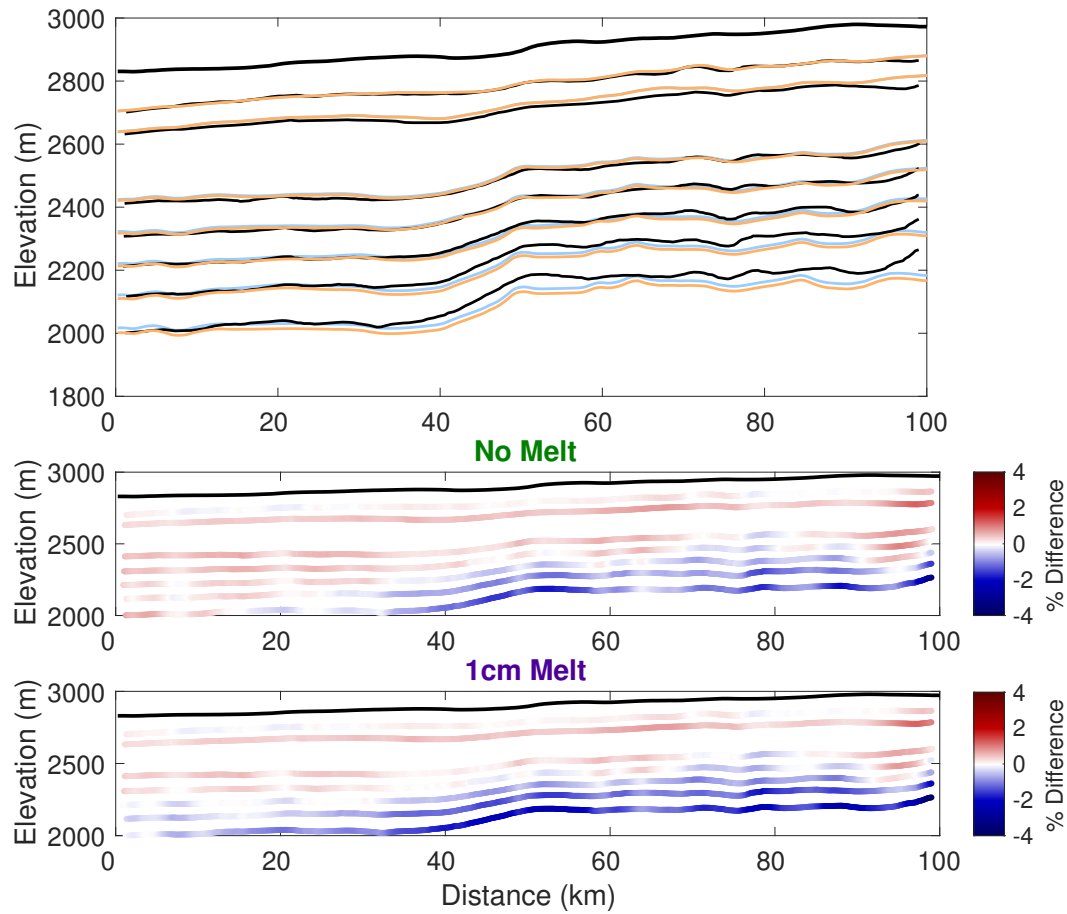


Figure S17: Comparison between modeled and measured internal layers in the flowband domain. Measured layers are shown in Figure S14. A) Observed (black) and modeled with no melt (blue) and 1 cm a<sup>-1</sup> melt (orange) internal layers. Observed layer ages are labeled. B) Percent misfit of layer depths for the “no melt” model. C) Percent misfit of layer depths for the “1 cm a<sup>-1</sup> melt” model.

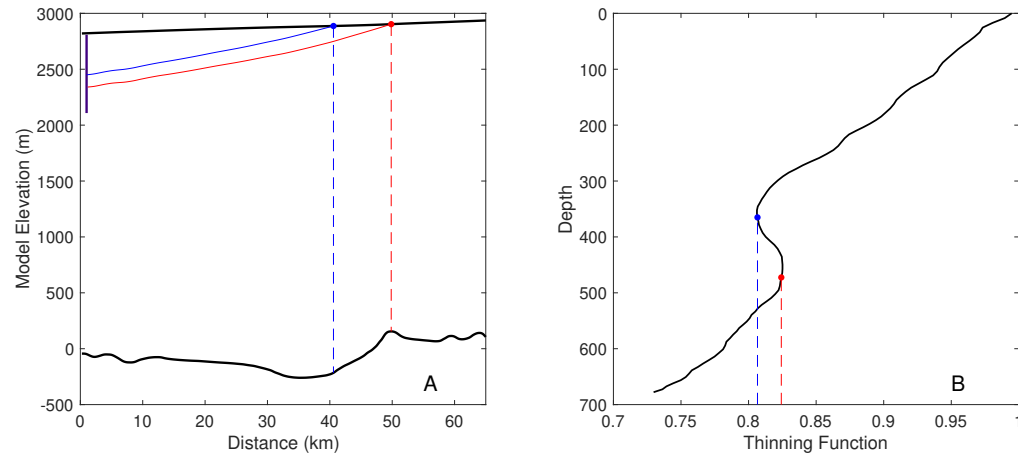


Figure S18: Illustration of the development of a reversal in the thinning function. A) Modeled particle paths with ice thickness (and corresponding bed elevation) at particle origin marked. Age of the red particle is  $\sim 7$  ka and age of the blue particle is  $\sim 6$  ka. Purple vertical line at the far left side is ice-core location and the depth of the core shows the depth range plotted in B. B) Modeled thinning function showing the reversal in thinning due to thickening of the ice sheet which the red particle experienced by the blue particle did not. The jaggedness of the thinning function is due to numerical challenges in the particle tracking.

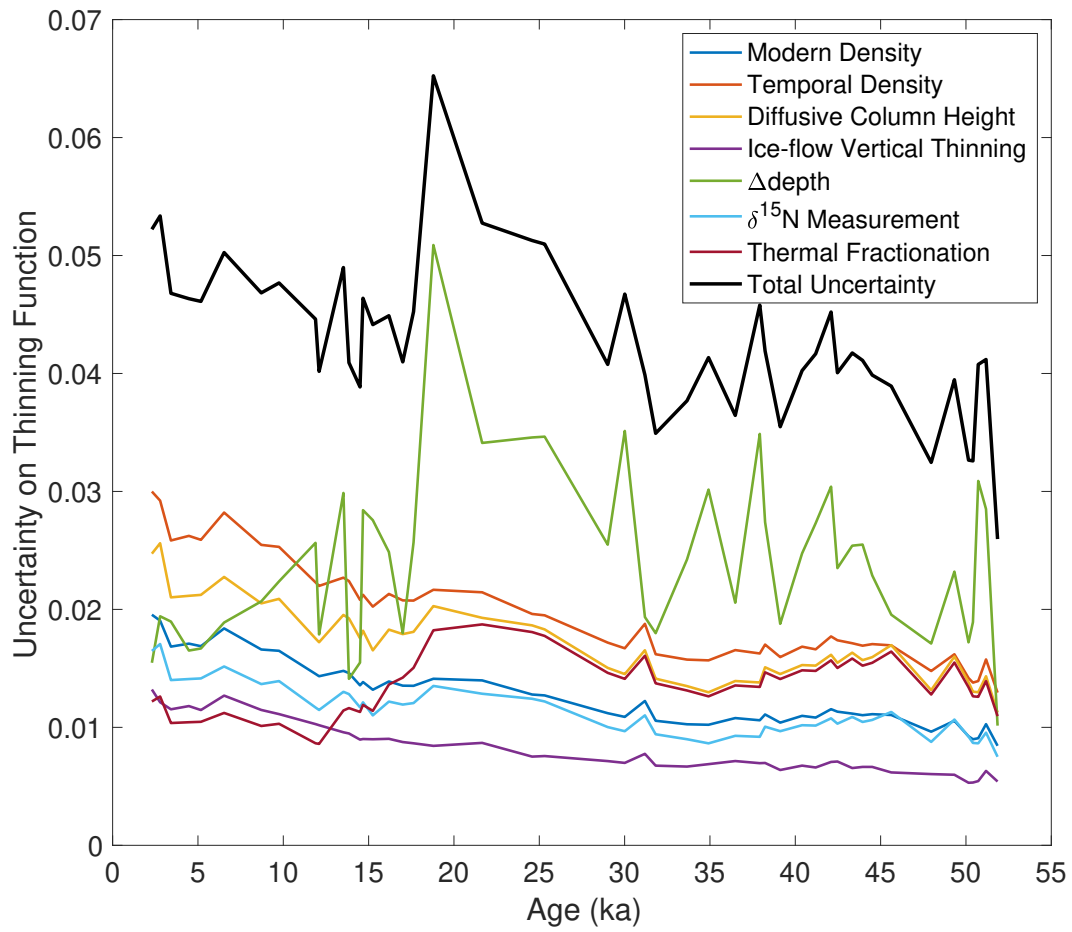


Figure S19: Uncertainty representing two standard deviations for the inferred thinning function from seven main sources described in Text S5.1.